Static and Dynamic Properties of Bio-Mimetic Systems

Inaugural-Dissertation

zur Erlangung des Doktorgrades
der Mathematisch-Naturwissenschaftlichen Fakultät
der Heinrich-Heine-Universität Düsseldorf

vorgelegt von

Silvia De Sio

aus Potenza

aus dem Institut für komplexe Systeme, Weiche Materie (ICS-3)
des Forschungszentrum Jülich, GmbH

Gedruckt mit der Genehmigung der
Mathematisch-Naturwissenschaftlichen Fakultät der
Heinrich-Heine-Universität Düsseldorf

Referent: PD Dr. Peter R. Lang

Korreferent: Prof. Dr. Jan K. G. Dhont

Tag der mündlichen Prüfung:

To my family,

for their profound and unquestionable support

Preface

Part of the work reported in this thesis is already published in peer-reviewed international journals and a book chapter. In the following I list all these publications, specify my personal contribution therein and denote where a specific publication is used in the thesis.

1. ***Depletion Interaction Mediated by fd-Virus: on the Limit of Low Density and Derjaguin Approximation.***
   De Sio, S. and P. Lang, Zeitschrift für Physikalische Chemie, 2015. **229**(7-8). I performed all the experiments and data analysis supported with helpful discussion with P.Lang.
   The manuscript was jointly written by P.Lang and me.
   The concepts of this article are used in Chapter 4, section 4.1.2.

2. ***Near Wal Dynamics of a spherical particle in crowded suspensions of colloidal rods-dynamic information from TIRM revisited***.
   De Sio, S., J.K.G. Dhont and P.R. Lang, Soft Matter, 2017, in revision. I performed all the experiments and data analysis supported with helpful discussion with P.Lang.
   The manuscript was jointly written by P.Lang, J.K.G. Dhont and me.
   The concepts of this article are used in Chapter 4, section 4.

3. ***Colloids and their interactions***.
   P. R. Lang and S. De Sio 46. IFF Spring School 2015: Functional Soft Matter J. K. G. Dhont, G. Gompper, G. Meier, D. Richter, G. Vliegenthart, R. Zorn(Eds.), Schriften des Forschungszentrums J•ülich, Key Technologies Vol. 94, Forschungszentrum J•ulich, J•ulich, 2015. ISBN 978-389336-999-7.
   The manuscript was written by P.Lang, utilizing my data and data analysis.
   The concepts of this manuscript are used throughout Chapter 1, in section 1.2.2 especially.

Summary

We used total internal reflection microscopy (TIRM) to measure the static interaction between colloidal probe spheres and a flat glass wall. The technique was applied to two fundamentally different systems. (i) The colloidal probe spheres and/or the glass wall were covered with a so called S-layer protein, Sgs-EGFP. In this case the protein-protein interaction was investigated. (ii) Bare colloidal spheres were suspended in a solution of rod shaped fd-virus next to a bare glass wall. Here we were mainly interested in the depletion interaction between the sphere and the wall induced by the rods. In the latter case we also analyzed the dynamic information, which is inherent to TIRM raw data, to obtain further insight into the mechanism underlying the sphere-wall interaction.

Protein-protein interactions: Measurements at increasing electrolyte content of the suspending buffer showed that the sphere is stable against irreversible sticking to the surface due to van der Waals attraction at significantly higher ionic strength, if the sphere and the surface are protein coated, as compared to the case of bare surfaces. Qualitative data analysis implies that there is an additional repulsive interaction on top of the DLVO potential, which is effective over a range of tens of nano-meters. This is at least one order of magnitude larger than the range of so-called hydration forces, which are usually considered responsible for protein stability beyond DLVO-interaction.

Depletion interaction induced by fd-virus: We measured depletion potentials by TIRM over a wide range of probe spheres sizes and rod concentrations to explore the limits of the fundamental approximations used in the classical Asakura-Oosawa theory (AO), which are the treatment of the depletant as an ideal gas and Derjaguin approximation, demanding that the sphere radius is much larger than the rod length. The experimental data follow the AO predictions at concentrations and size ratios, at which this is expected to fail. At even higher fd-concentrations, we observe deviations from the ideal gas behavior, which are much larger and of opposite sign than predicted earlier. By analyzing the dynamic information inherent to the raw data, we found evidence that this observation is caused by the dynamics of the rod network which is inevitably formed at fd-concentrations above the overlap density. In a first step, we used the initial slope of the intensity correlation functions to determine spatially averaged particle diffusion coefficients, which show a dependence on the fd-concentration which is intriguingly similar to the concentration dependence of the amplitude of the depletion potential. Therefore, we assume that the large amplitude of the apparent attractive potential at high fd-concentrations is not anymore due to depletion forces but rather to the particle being mechanically trapped in the network of rods.

To gain further insight into the systems dynamics, we determined spatially resolved dynamic data. We found that the particle's drift velocity due to the external force field can be determined with excellent accuracy, while it appears to be generally much more difficult to measure near-wall diffusion coefficients by TIRM. This finding might open a new route to use TIRM as tool to measure local viscosities at extremely low shear rates by a passive micro-rheology approach.

Zusammenfassung

In dieser Arbeit beschreibe ich Experimente mit „total internal reflection microscopy“ (TIRM) zur Messung der Wechselwirkungspotenziale zwischen einer kolloidalen Sondenkugel und einer flachen Glaswand. Es wurden zwei Systeme untersucht: (i) Die Kugel und/oder die Glaswand waren mit einer Lage aus dem sogenannten S-Layer Protein Sgs-EGFP beschichtet. In diesem Fall wurden nicht-spezifischen Protein-Protein Wechselwirkungen untersucht. (ii) Die Sondenkugel wurde in einer Lösung von stäbchenförmigen fd-Viren suspendiert, um die Verarmungs- (Depletion) -wechselwirkung zu untersuchen, die durch die Stäbchen verursacht wird. In diesem Fall habe ich auch die, in den Rohdaten enthaltene Information, zur Dynamik des Systems analysiert, um die Mechanismen besser zu verstehen, die der Wechselwirkung zugrunde liegen.

Protein-Protein Wechselwirkung: Es wurden vergleichende Experimente gemacht, in denen Systeme mit unbeschichteten Oberflächen solchen gegenüber gestellt wurden, in denen die Oberflächen mit Sgs-EGFP bedeckt waren. Messungen bei steigendem Elektrolytgehalt der Suspension zeigen, dass das System sehr viel stabiler gegenüber einer irreversiblen Adhäsion aufgrund von van der Waals Attraktion ist, wenn die Kugel und die Glaswand mit Proteinen beschichtet sind. Eine qualitative Datenanalyse zeigt, dass eine zusätzliche abstoßende Wechselwirkung existieren muss, die über die klassischen DLVO-Potenziale hinausgeht. Allerdings hat diese Wechselwirkung eine Reichweite von mehreren zehn Nanometern, was mindestens eine Größenordnung mehr ist, als die Reichweite sogenanntes Hydration-Kräfte, die üblicherweise zur Erklärung der Stabilität von Proteinen bei hohen Salzkonzentrationen herangezogen werden.

Depletion Wechselwirkung durch fd-Viren: Ich habe Depletion-Potenziale über einen weiten Bereich von Kugelgrößen und Stäbchenkonzentrationen gemessen, um zu untersuchen, wo die die Grenzen der fundamentalen Näherungsannahmen liegen, die in der klassischen Asakura-Oosawa (AO)-Theorie der Depletionwechselwirkung gemacht werden. Dies sind die Behandlung der Stäbchen als ideales Gas und die Derjaguin-Näherung, die verlangt, dass der Kugelradius sehr viel größer als die Stäbchenlänge sein muss. Die experimentellen Daten werden durch die AO-Voraussagen sehr gut beschrieben, auch in Konzentrationsbereichen und bei Größenverhältnissen, wo das eigentlich nicht mehr erwartet werden kann. Bei noch höheren fd-Gehalten beobachte ich Abweichungen vom Verhalten des idealen Gases, die allerdings sehr viel größer sind und das entgegengesetzte Vorzeichen haben, als theoretisch vorausgesagt. Die Analyse räumlich gemittelter Diffusionskoeffizienten, legt nahe, dass diese Abweichungen durch die Dynamik des Stäbchennetzwerks bedingt sind, das sich bei hohen Konzentration unweigerlich bildet. Die Amplitude der Depletionwechselwirkung und die gemittelten Diffusionskoeffizienten zeigen eine sehr ähnliche Abhängigkeit von der Stäbchenkonzentration. Dies legt nahe, dass die überhöhte Amplitude des effektiven attraktiven Potentials bei hohen fd-Konzentrationen nicht mehr durch Depletionwechselwirkungen zustande kommt, sondern eher durch eine Behinderung der Kugelbeweglichkeit durch das Stäbchennetzwerk.

Um weitere Einblicke in die Dynamik der Systeme zu bekommen, habe ich ortsaufgelöste Daten bestimmt. Dabei habe ich gefunden, dass die Drift-Geschwindigkeit der Partikel, die durch die äußeren Kräfte verursacht wird, sehr genau gemessen werden kann. Dagegen erscheint es sehr viel schwieriger ortsaufgelöste Diffusionskoeffizienten mit TIRM zu messen. Diese Beobachtung könnte eine neue Methode ermöglichen, TIRM zu nutzen, um mit einem mikrorheologischen Ansatz lokale Viskositäten bei extrem kleinen Scherraten zu messen.

Table of Contents

Introduction

In the present work static and dynamic properties of a specific kind of colloidal systems have been investigated by means of Total Internal Reflection Microscopy (TIRM).

Historically the only access to information about pair-interaction potentials has been via scattering techniques, like light scattering [1-3]. Yet, deriving interaction potentials with such methods always requires model assumptions that can be source of misinterpretations. For this reason, there has been a growing need for developing more direct methods to measure interactions, like e.g. Surface Force Apparatus [4] (SFA), Atomic Force Microscopy [5] (AFM), Optical Tweezers [6-8] and Total Internal Reflection Microscopy (TIRM). Among these techniques, TIRM has proven the most sensitive and less invasive method [9] for the direct measurement of pair-wise interactions [10, 11]. Thus, this experimental investigation has chosen TIRM as most suitable set-up, given our aims. Some examples of what has been already done with TIRM is the measurement of Van der Waals interactions [12], of critical Casimir forces [13, 14] and finally of depletion interactions [15-18]. The systems we decided to investigate are special kind of colloidal systems called Bio-mimetic. The term ‘‘Bio-mimetic’’ derives from ancient Greek: *βίος* (bios), life, and *μίμησις* (mimesis), imitation, and it was coined by the American bio-physicist Otto Herbert Schmitt during his doctoral research studies in the 50’s, while he was attempting to engineer a device that could replicate the biological system of nerve propagation in squids [19]. He realized that, through evolution and adaptability, biological systems provide countless of yet unrecognized technological solutions to complex human problems [20]. Thus, the aim of Bio-mimetics, which grew to be a hall independent scientific area, became to devise systems, either partially composed of biological matter or completely synthetic, able to mimic nature’s favourite solutions. Because of the richness and complexity within real biological systems, Bio-mimetics relate with many different fields. In applied bio-physics, for example, biomimetic systems are devised and used as models for real biological systems that may be very difficult to access and study otherwise.

In this work a binary mixture of micron sized polystyrene beads and wild type fd-viruses [21-26] was chosen as model system to study depletion interactions induced by long stiff rods, while the same polystyrene beads, coated with S-layer proteins [27-29], have been used to study protein-protein non-specific interactions.

Nowadays it is well known that the physical properties of colloidal suspension are strongly affected by the forces acting between its components. Attempts to explain suspensions stability in these terms, go back to the beginning of the 20th century. Important and extensively studied forces in colloidal systems are magnetic forces, steric forces (due to attached polymers) and the so called DLVO interactions. The latter originate from surface charge interactions between colloidal particles like Van der Waals attraction and electrostatic repulsion. These interactions govern in many cases the stability and phase-behaviour of colloidal suspensions [8] but, in the last decades, it has been observed that stability is also affect by yet another kind of forces, of entropic nature and normally classified as Non-DLVO interactions. The latter can be due, for example, to non-adsorbing polymers in solution, which, through excluded volume effects, can drive larger colloids towards aggregation, as in the case of depletion interactions [30-32], or to the rearrangement of water molecules around proteins surfaces forming a steric-like layer that prevents aggregation, as in the case of hydration forces [33, 34].

Protein-protein non-specific interactions became a topic of great interest after it was clear that describing proteins like spherical patchy particles, thus with inhomogeneous surface charge distribution and a pair-wise potential defined solely by the DLVO, was not enough to justify their stability at physiological conditions [35]. Nonetheless, the fact that life is instead possible just at physiological conditions, implies stability in fact. An experimental investigation by Valle-Delgado et al., conducted via AFM between bovine serum albumin layers adsorbed on different substrates, has shown a very strange behaviour at high salt concentrations and around the isoelectric point of the proteins: those interact attractively at low salt concentrations but repulsively at high salt concentrations [36]. Thus, in the present investigation, we decided to test if proteins belonging to the “slim layer” (s-layer) group would have the same behaviour in a salt concentration gradient. This class of proteins is one of the most common outermost cell envelope components of many bacteria and archea [37-39], shown to be determinant in the adaptation of such microorganisms to the external environment [27]. Moreover S-layer proteins are extensively studied for their ability of self-assembly in perfect 2D-lattices (e.g. in Fig. (II)), feature that can be used to immobilize other kind of biomolecules, leading to the so called *S-layer fusion proteins* [28].

Figure II-Sketch of the p2 symmetry of the s-layer protein monomeric di-blocks.

A relevant example of the latter for our purposes are the *fluorescent s-layer fusion proteins* used already in a very broad range of applications in nano-bio-technology and bio-mimetics [40-46]. In this case, the labelling of the S-layer proteins with fluorescent dyes is obtained by genetically inserting cysteine groups [47] which will functionalize the proteins surface fluorescent. Moreover, S-layer fusion proteins can be recrystallized on different kinds of substrates among which various kinds of polymers [48]. Thus, we chose this kind of fluorescent S-layer fusion proteins to obtain the *Bio-functional fluorescent particles and substrates* used to probe protein-protein non-specific interactions. We used total internal reflection microscopy (TIRM) to measure interaction potentials between 4 μm polystyrene beads and a planar wall at constant pH=9 and at increased salt concentration, between 2-60 mM, considering all the possible cases: un-coated particle with un-coated wall, coated particle with un-coated wall, un-coated particle with coated wall (see section (4.1.1)). Fluorescence was used to check the quality of the coating procedure, via fluorescent confocal microscopy (see Fig. (3-1)(a)).

We can now introduce the second system, object of the present investigation: binary mixtures of spheres and rods. The latter have been widely investigated for their complex and interesting phase behaviour [49-51]. One study in particular, carried out using spherical particles and fd-viruses as depletants, has shown how diverse and surprising such phase diagram can be and how critically it depends on the size ratio of the spheres' radius to the length of the rods and on the relative volume fraction of one species with respect to the other [52] . Thus, the determination of stability configurations in binary mixtures, strongly on depends depletion interactions. The first formulation of a pair-wise depletion interaction potential belongs to the pioneering work of Asakura and Oosawa in 1954 [30-32], where depletion is explained as a purely entropic effectively attractive force pushing larger colloids together, for the smaller species to increase their free available volume, thus reduce the total energy of the system towards the equilibrium. In their model Asakoura and Oosawa applied two basic assumptions: the first is that the size of the colloidal spheres must be much larger than the depletant itself, called Derjaguin's approximation (I); the second is for the depletants to be treated as an ideal gas, thus low density approximation (II).

There has been a plethora of studies reported in literature about the experimental verification of the depletion model within the theoretical limits [53-55] and as well some simulations extending investigations beyond the limits of Derjaguin and low density approximation [56]. In this respect, Auvray [57] and Mao et al. [58] theoretically studied the influence of the mutual excluded volume of the rods up to second order in density, finding that the resulting forces at increased rod number density showed values reduced of about six percent respect to the low density prediction, at rods concentrations as high as ten times the overlap value. About the effect of the spheres to depletant size ratio, Yaman et al. [56] and Lang [59], by means of numerical calculations, found out a rather pronounced effect linked to the violation of Derjaguin's approximation. At ratios of rod-length over sphere radius L/R=2, e.g. the predicted values for the potential of the spheres at contact is approximately three times smaller than predicted by Derjaguin approximation. Experimentally, Yodh et al., using laser tweezers and image analysis techniques [60, 61], studied depletion interactions between silica particles mediated by fd-virus, with L/R>1 and at high concentrations. These authors though, neglecting their violation of low density approximation, rather assigned the deviation of their results from the predictions to the finite flexibility of the fd-virus. The latter explanation has been though corrected by a subsequent study from July et al. [62], where, by comparing potentials induced by wild type fd-virus to data obtained using a stiff fd-mutant as depletant, it was shown that the flexibility of fd-rods does not change their effectiveness significantly. Given this state of the art, in our contribution we used total internal reflection microscopy (TIRM) to probe simultaneously both limits of the Asakoura and Oosawa model theory through a more systematic data collection. We measured the interaction potentials between probe spheres of different sizes, 1–4μm in diameter, and a glass wall, induced by a rod-like fd-virus with concentrations varied from zero to 1mg/mL (see Fig. (4-4)). Given a rod length $L = 880\ nm$, we measured with size-ratios varied in the range 0.44<L/R<1.76 and with concentrations in the range $0.85c^* \leq c \leq 14c^*$, being $c*$=0.07 mg/mL the fd-virus overlap concentration, in order to test both, the low density and Derjaguin approximation (see section (4.1.2)).

The same data sets were also analysed to try and gather dynamical information. To do so at first we followed the work published by Prieve and co-workers [63, 64] where they show that the slope at very short times of the intensity auto-correlation function for a probe sphere in an evanescent field can be used to derive an averaged diffusion coefficient normal to the interface,

$< D_n^{TIRM} >$ (see section (4.2.1)). The latter is a quantity related to the Einstein's bulk diffusion coefficient, D_0, via a function that describes the hydrodynamic slow-down of the probe due to the presence of a near interface, averaged over all the heights spanned by the probe particle. Later on we realized that more detailed information could be gathered via a novel way to calculate mean displacement and mean square displacement at given heights (see section (4.2.2)). The relevance of this new calculations lies not only in the possibility of calculating normal diffusion coefficients (see Fig. (4-14)) and drift velocities (see Fig. (4-15)) at any accessible distance from the interface but also extrapolating absolute solvent viscosities (see Fig. (4-16)).

This thesis starts exposing all theories and models needed to explain both static and dynamic properties of the systems investigated via total internal reflection microscopy (see DLVO Interactions, Non-DLVO Interactions and Total Interaction Energy between a Sphere and a Wall, Section 1.1, 1.2 and 1.3 respectively and Dynamics of colloids in suspension, Section 1.4). The description of the principles, the set-up are collected in Chapter 2 (see Total Internal Reflection, Section 2.1and Sub-sections 2.1.1 and 2.1.2). The description of the experimental procedures involving samples and samples preparation are collected in chapter 3, section 3.1. The results obtained from both static and dynamic treatment of the TIRM intensity traces over time are presented in chapter 4, Results from Statics and Dynamics (see Section 4.1 with sub-sections 4.1.1 and 4.1.2 and section 4.2 with sub-sections 4.2.1 and 4.2.2) The last chapter is of course dedicated to the conclusions drawn from the results of both static and dynamic treatment (Conclusions, Chapter 5, Section 5.1 and Section 5.2).

1 Theory

Introduction

This section will be devoted to the description of the model theories needed to explain pair-wise interactions between a particle and a planar wall, above which the particle is undergoing Brownian motion. The discussion will be divided into two main sections. Section (1.1) describes all the so called DLVO interactions, therefore: *Double Layer Forces* (0)*; Interaction Energy between Two Planar Walls* (1.1.2)*; Interaction Energy between Molecular Dipoles* (1.1.3)*; Van der Waals Interactions between a Sphere and a Wall* (1.1.4). Section (1.2) takes care of the so called Non-DLVO interactions, therefore: *Gravitation and Light Forces* (1.2.1)*, Depletion Forces* (0)*, Hydration Forces* (1.2.3). The last section of the chapter, Section (1.4), will focus instead on Dynamics of a particle in the close vicinity of an interface focusing especially on the calculation of *Auto-correlation functions* (0) and of *Mean Displacement and Mean Square Displacement at given Starting positions* (0), novelty proposed by us.

1.1 DLVO Interactions

Double-layer forces

When a colloidal particle carrying dissociable groups on the surface, is dispersed into a polar solvent (e.g. water), it develops a charged surface due to the dissociation of counter-ions from it. The same phenomenon occurs if the planar side of a glass slide is exposed to water. If the colloidal particle and the glass wall are like charged, they repel each other via a screened Coulomb potential given by the average distribution of anions and cations around both bodies. The forces deriving from such screened Coulomb potential interaction are called *Double Layer Forces*. The interaction between two charged interfaces is therefore modified by a distribution in space of ions and cations. When the system is in thermal equilibrium, the ions are distributed according to Boltzmann's law distribution, thus, the number density of ions shows an exponential dependence on the electrostatic potential they are subject to. Here the goal is to derive an approximate expression for the interaction potential between a charged wall and a charged sphere. For this purpose we start deriving an expression for the screened Coulomb potential emerging from an infinitely expanded planar wall, in an electrolyte solution and with homogenous surface charge distribution, along the z direction.

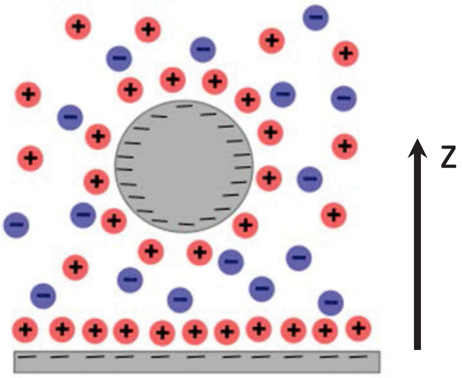

Figure 1-1: Sketch of a stabilized colloidal particle suspended in a near to wall configuration with release and rearrangement of ions and cat-ions in solution forming the so called double layer.

We start from the one-dimensional form of the Poisson's equation:

$$\frac{\partial^2\psi(z)}{\partial z^2} = -\sum_i \frac{Z_i e\rho_i(z)}{\varepsilon_0\varepsilon}. \tag{1.1}$$

This relates the second distance derivative of the potential, $\psi(z)$, to the number densities, $\rho_i(z)$, at distance *z*, of the ions of species i. Here e is the elementary charge, Z_i.is the valency of ion species i, ε_o is the vacuum permittivity and ε is the relative dielectric constant of the solvent. As stated before, the ion number density is determined by a Boltzmann distribution:

$$\sum_i \rho_i\,(z) = \sum_i \rho_i^0 e^{-\frac{Z_i e\psi(z)}{k_B T}} \tag{1.2}$$

where $k_B T$ is the unit thermal energy and ρ_i^0 is r the number density of ion species i at zero potential, i. e. at infinite distance from the wall. Thus, the combination of Eqs. (1.1) and (1.2) results the Poisson-Boltzmann equation:

$$\frac{\partial^2\psi(z)}{\partial z^2} = -\sum_i \frac{Z_i e\rho_i^0 e^{-\frac{Z_i e\psi(z)}{k_B T}}}{\varepsilon_0\varepsilon}. \tag{1.3}$$

To solve this second order differential equation one should recall that the concentration of the ions shows an exponential dependency with respect to the interaction potential, therefore its first derivative with respect to *z* is:

$$\sum_i \frac{d\rho_i(z)}{dz} = -\sum_i \frac{Z_i e \rho_i(z)}{k_B T} \frac{d\psi(z)}{dz}. \tag{1.4}$$

Further, from Eq. (1.1) we may write:

$$\sum_i \frac{Z_i e \rho_i(z)}{k_B T} = -\frac{\varepsilon_0 \varepsilon}{k_B T} \frac{d^2\psi(z)}{dz^2}. \tag{1.5}$$

Considering both equivalences, one can write:

$$\sum_i \frac{d\rho^i(z)}{dz} = \frac{\varepsilon_0 \varepsilon}{k_B T} \frac{d^2\psi(z)}{dz^2} \frac{d\psi(z)}{dz} = \frac{\varepsilon_0 \varepsilon}{2k_B T} \frac{d}{dz} \left(\frac{d\psi(z)}{dz}\right)^2 \tag{1.6}$$

Which, with the boundary condition $\lim_{z\to\infty} \psi(z) = 0$, can be readily integrated to result:

$$\sum_i (\rho_i(z) - \rho_i^0) = \frac{\varepsilon_0 \varepsilon}{2k_B T} \left(\frac{d\psi(z)}{dz}\right)^2. \tag{1.7}$$

Considering now the simple case of a 1:1 univalent electrolyte, this means that only two ion species will be found in solution with opposite valency, $Z_{+/-} = \pm 1$ and same bulk density, $\rho^+(x) = \rho^-(x)$. In this case Eq. (1.7) reduces to:

$$\rho^-(z) + \rho^+(z) - 2\rho_0 = \frac{\varepsilon_0 \varepsilon}{2k_B T} \left(\frac{d\psi(z)}{dz}\right)^2 \tag{1.8}$$

where, substituting to the densities their explicit form leads to:

$$\rho_0 \left(e^{\frac{e\psi(z)}{k_B T}} + e^{-\frac{e\psi(z)}{k_B T}} - 2\right) = \frac{\varepsilon_0 \varepsilon}{2k_B T} \left(\frac{d\psi(z)}{dz}\right)^2, \tag{1.9}$$

and to the equivalent formulation

$$\rho_0\left(e^{\frac{e\psi(z)}{2k_BT}}-e^{-\frac{e\psi(z)}{2k_BT}}\right)^2=\frac{\varepsilon_0\varepsilon}{2k_BT}\left(\frac{d\psi(z)}{dz}\right)^2. \tag{1.10}$$

Further on, the latter, with the definition of the *sinh*-function, may be rewritten as:

$$\frac{d\psi(z)}{dz}=\pm\sqrt{\frac{8\rho_0k_BT}{\varepsilon_0\varepsilon}}\sinh\left(\frac{e\psi(z)}{2k_BT}\right) \tag{1.11}$$

Where, as the potential is expected to decrease with distance from the wall, the positive solution be disregarded as unphysical. To solve the remaining differential equation we simplify the form substituting $y=\frac{e\psi(z)}{2k_BT}$, thus obtaining:

$$\frac{dy}{dz}=\frac{e}{2k_BT}\frac{d\psi(z)}{dz} \tag{1.12}$$

And finally Eq. (1.11) can be rewritten as:

$$\frac{dy}{\sinh y}=\kappa dz \tag{1.13}$$

where we defined $\kappa=\sqrt{\frac{2e^2\rho_0}{\epsilon_0\varepsilon k_BT}}$ as the inverse Debye screening length.

In order to solve Eq. (1.12) both sides are integrated:

$$\int_{y_s}^{y}\frac{1}{\sinh y}dy'=\kappa\int_0^z dz' \tag{1.14}$$

here the subscript s refers to properties at the glass surface, i.e. $z=0$. The integral on the right side is plane simple and the one on left side is solved by using tabulated results, obtaining:

(1.15)
$$ln\left(\frac{\tanh\left({}^{y}/_{2}\right)}{\tanh\left({}^{y_s}/_{2}\right)}\right) = -z\kappa$$

from which it follows:

(1.16)
$$\tanh\left({}^{y}/_{2}\right) = \tanh\left({}^{y_s}/_{2}\right) e^{-\kappa z} \equiv \gamma e^{-\kappa z}.$$

Recalling now the definition of the inverse *tanh*-function $\tanh^{-1}(X) = \frac{1}{2}\ln\left(\frac{1+X}{1-X}\right)$ and the Taylor expansion of the logarithm, only valid for $\gamma e^{-\kappa x} \ll 1$, one can write:

(1.17)
$$y = \ln\left(\frac{1+\gamma e^{-\kappa z}}{1-\gamma e^{-\kappa z}}\right) \approx \ln(1+2\gamma e^{-\kappa z}) \approx 2\gamma e^{-\kappa z}.$$

The latter is the so called Debye-Hückel approximation for ion gases at high temperatures for which, substituting back the definitions of y and γ, yields:

(1.18)
$$\psi(z) = \frac{4k_BT}{e}\tanh\left(\frac{e\psi_S}{4k_BT}\right)e^{-\kappa z}$$

This is finally the formulation of the electrostatic potential at a distance z from an infinite plate in a 1:1 electrolyte solution. Eq. (1.18) can be further simplified by applying the Debye-Hückel approximation again. In case of small surface potentials $\psi_S \leq 25\ mV$, one can write:

(1.19)
$$\psi(z) \approx \psi_S e^{-\kappa z}.$$

Here the meaning of the inverse Debye screening length, constant κ, becomes evident: it is the inverse of the distance from the surface, where the electric potential has dropped to z/e of the value at the surface. Having an explicit formulation for the electrostatic interaction potential, $\psi(z)$, allows for the evaluation of yet another interesting quantity, the surface charge density, σ, which is defined as:

(1.20)
$$\sigma = -\sum_i \int_0^\infty Z_i e \rho_i(z) dz$$

given the electro-neutrality principle. Now recalling the Poisson equation one can write:

(1.21)
$$\sigma = \varepsilon\varepsilon_0 \int_0^\infty \frac{d^2\psi(z)}{dz^2} dz = -\varepsilon\varepsilon_0 \frac{d\psi(z)}{dz}\bigg|_{z=0}.$$

Equation known as the Grahame-relation, which together with Eq. (1.11) and the approximation for small surface potentials yields:

(1.22)
$$\sigma = \varepsilon\varepsilon_0 \sqrt{\frac{8\rho_0 k_B T}{\varepsilon\varepsilon_0}} \sinh\left(\frac{e\psi_0}{2k_B T}\right) \approx \varepsilon\varepsilon_0 \kappa \psi_S.$$

Or the explicit form for the surface charge density on a planar wall immersed in a 1:1 electrolyte solution.

The following step towards the calculation of the pair-wise electrostatic interaction potential between a sphere and a wall consists in the determination of the interaction energy between two planar walls.

Interaction energy between two planar walls

Starting from the now known expression for the electrostatic potential emerging from a planar charged wall, we can now calculate the energy which is required to bring two such identical planes together from an infinite distance to a finite separation, *D*. We assume two parallel plates charged alike and to be immersed in a 1:1 electrolyte solution, which is treated as an ideal gas. Due to the electrostatic potential between the plates, the osmotic pressure due to the ions in the gap will be different from the outside, resulting in a net force pushing the two plates apart.

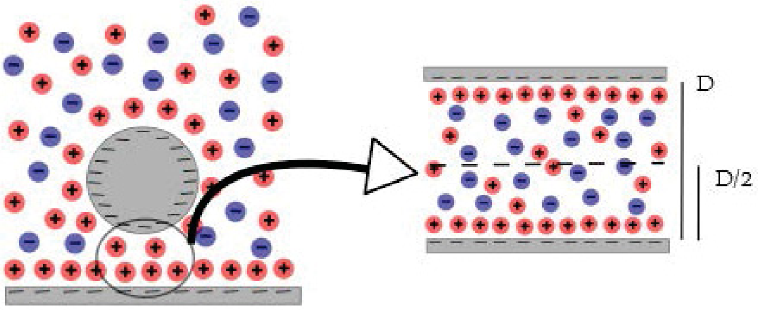

Figure 1-2 Double layer interactions: from sphere/wall to wall/wall interactions and back.

To calculate this difference in osmotic pressure the Gibbs-Duhem relation is used:

$$\mu_i N_i = U_i + \Pi_i V_i - TS_i \tag{1.23}$$

where N_i is the number of ions, U_i the internal energy, Π_i, the osmotic pressure V_i the volume and S_i the entropy related to the ion species *i.* The system temperature is T and the definition of the chemical potential of species *i* is

$$\mu_i = Z_i e\psi(z) + k_B T ln\rho_i(z). \tag{1.24}$$

If the temperature and the composition of the system remain unchanged, the total differential of the chemical potential, as defined in Eq. (1.23), reduces to $d\mu_i N_i = d\Pi_i V_i$, thus:

$$d\mu_i = \frac{d\Pi_i}{\rho_i}, \tag{1.25}$$

while the total differential of Eq. (1.24) is:

$$d\mu_i = Z_i e d\psi(z) + k_B T \frac{d\rho_i(z)}{\rho_i(z)}. \tag{1.26}$$

Equating the two formulations results in the elimination of the explicit dependence from $d\mu_i$ and in the expression of the total differential of the osmotic pressure $d\Pi_i$:

$$d\Pi_i = \rho_i(z)\left[Z_i e d\psi(z) + k_B T \frac{d\rho_i(z)}{\rho_i(z)}\right]. \tag{1.27}$$

To get the pressure between the two walls at a given separation distance z, one needs to integrate:

$$\int_{\infty}^{z} dz' \frac{d\Pi_i(z')}{dz'} = \int_{\infty}^{z} dz' \rho_i(z')\, Z_i e \frac{d\psi(z')}{dz'} + k_B T \int_{\infty}^{z} dz' \frac{d\rho_i(z')}{dz'}, \tag{1.28}$$

which yields:

$$\Pi_i(z) = -\frac{\varepsilon\varepsilon_0}{2}\left(\frac{d\psi(z')}{dz'}\right)^2\Bigg|_{z'=z} + k_B T(\rho_i(z') - \rho_i^0)\big|_{z'=z} \tag{1.29}$$

thus, recalling Eqs. (1.1) and (1.7) and considering the walls at a fixed separation distance $z = D$:

$$\begin{aligned} \Pi(D) &= k_B T \sum_i (\rho_i(z = D) - \rho_i^0) \\ &= 4\rho_0 k_B T \left[\sinh\left(\frac{e\psi(D)}{2k_B T}\right)\right]^2. \end{aligned} \tag{1.30}$$

In the latter, we assume simple additivity of the contributions by each ion species to the total osmotic pressure. At this point it is important to notice that, because of the symmetry of the problem of two identical walls facing each other, the electrostatic potential, $\psi(z)$, in $z = D/2$ is $\psi(D/2) = 2\tilde{\psi}(D/2)$, where $\tilde{\psi}(D/2)$ is the potential emerging from a single surface at the mid-plane between two walls. Moreover, the fact that the system is in thermal equilibrium ensures for its osmotic pressure to be a constant through all the gap. Thus, the easiest way to calculate the osmotic pressure at fixed distance $z = D$, is to use the symmetry of the electrostatic potential to calculate $\Pi(D)$ as $\Pi\left({}^{D}/_{2}\right)$. Thus, for a 1:1 electrolyte one gets:

$$\Pi(D) = 4\rho_0 k_B T \left[\sinh\left(\frac{e\psi\left({}^{D}\!/_{2}\right)}{2k_B T}\right)\right]^2 = 64\rho_0 k_B T\, tanh^2\left(\frac{e\psi_0}{2k_B T}\right) e^{-\kappa D}. \tag{1.31}$$

The energy per unit area, namely γ_{el}^{ww}, as a function of separation distance due to electrostatic interaction, is found by simply integrating the latter over all possible distances $D' \in [\infty, D]$:

$$\gamma_{el}^{ww}(D) = \frac{64 k_B T \rho_0}{\kappa} tanh^2\left(\frac{e\psi_0}{2k_B T}\right) e^{-\kappa D}. \tag{1.32}$$

The latter can be used to picture the electrostatic potential between a sphere and a wall, by means of Derjaguin's approximation:

$$F_{el}^{ss}(D) = 2\pi \frac{R_1 R_2}{R_1 + R_2} \gamma_{el}^{ww}, \tag{1.33}$$

where the forces between curved surfaces, with curvature radii R_1 and R_2, are related to the interaction energy per unit area between flat ones, provided the interaction potential between them is short-ranged and decaying with distance. In our case one of the two bodies is an infinitely extended planar wall thus one of the two radii must be taken as infinite. Given e.g. $R_2 \to \infty$ and $R_1 = R$, the upper equation will simplify to the following:

$$F_{el}^{sw}(D) \cong 2\pi R \gamma_{el}^{ww}. \tag{1.34}$$

Thus, a subsequent integration with respect to distance will give us the electrostatic interaction energy between and sphere and a planar wall, charged alike and in a monovalent electrolyte solution:

$$\Phi_{el}^{sw}(D) = \frac{128\pi R k_B T \rho_0}{\kappa^2} tanh^2\left(\frac{e\psi_0}{2k_B T}\right) e^{-\kappa D} = B e^{-\kappa D} \tag{1.35}$$

given that all the terms before the exponent are constants of the system.

From molecular dipole interactions to van der Waals interactions between colloidal bodies

Another contribution to the interaction energy between colloidal bodies at short distances is due to the Van der Waals forces. Such forces are not of a simple nature as they arise from dipolar interactions happening at a molecular scale between the components of the macroscopic bodies. For the same reason those forces are to be found even between non polar bodies at extremely short distances where molecular interactions become predominant. From a point of view of charge interaction, molecules can be picture as dipoles thus related mainly to three kind of forces:

- Forces due to the orientation of permanent dipoles;
- Forces between induced dipoles;
- Forces of dispersion or London forces.

Mathematically, the interaction energies corresponding to the listed terms show all the same inverse power law dependence on separation distance, r^{-6}, so those can be linearly summed up defining the Van der Waals interaction between two atoms or molecules:

$$\varphi_{vdw}(r) = -\frac{1}{r^6}\left(c_{orient} + c_{ind} + c_{disp}\right) = -\frac{C}{r^6}. \tag{1.36}$$

Here we us φ as the symbol for the interaction energy to distinguish interaction at a molecular or atomic level from those between colloidal bodies which will be termed Φ in the following. The van der Waals interaction between two colloidal bodies of various shapes can be pictured generalizing the pair-wise molecular interactions summing those up over the macroscopic volumes.

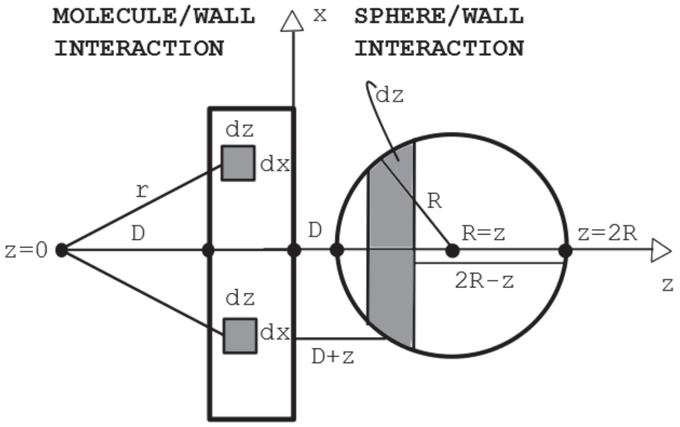

Figure 1-3 Sketch of the geometries followed for the calculation of Van der Waals interactions in the two cases: molecule/wall and then sphere/wall interactions. To be noticed that for the second case the origin of the z axes has to be shifted to the sphere surface

In this way e.g. the total interaction between a planar wall and a spherical object can be calculated. As sketched in Fig. (1-3), the first step is to describe the interaction between a single molecule and a wall made up of molecules of the same kind:

$$\varphi_{vdw}^{mw} = -\sum_{i=1}^{N} \frac{C}{r_i^6} = -NC\sum_{i=1}^{N} \frac{1}{r_i^6}. \tag{1.37}$$

Given that: $N = \rho V => dN = \rho dV$, the second term of the latter equation can be re-written as an integral over the entire wall:

$$\varphi_{vdw}^{mw} = -\int_V dV \frac{C}{r^6} \tag{1.38}$$

where the elementary volumes $dV = 2\pi x dx dz$ pictures cylindrical shells with radius x, thickness dx and length dz. With this substitution one can calculate the interaction energy between a single molecule and a planar wall at a given distance , $\varphi_{vdw}^{mw}(D)$, as follows:

$$\varphi_{vdw}^{mw}(D) = -2\pi C\rho \int_D^\infty dz \int_0^\infty dx \frac{x}{(x^2+z^2)^3} =$$

$$= \frac{2\pi C\rho}{4} \int_D^\infty dz \frac{1}{(x^2+z^2)^2}\bigg|_0^\infty = \tag{1.39}$$

$$= -\frac{2\pi C\rho}{4}\int_D^\infty dz\frac{1}{z^4} = -\frac{\pi C\rho}{6D^3}.$$

Now, to calculate the attractive interaction between a sphere and a wall at a given distance, $\Phi_{vdw}^{sw}(D)$, one needs to extend the same kind of integration used above, this time considering elementary volumes from a spherical slice the closest to the wall. To do that the elementary volume dV must be taken as follows $dV = \pi x^2 dz = 2\pi(R-z)zdz \approx 2Rzdz$, thus:

$$(1.40) \qquad \Phi_{vdw}^{sw}(D) = \rho\int_0^\infty \varphi(D+z)2Rzdz = -\frac{\pi C\rho^2}{6}\int_0^\infty \frac{2Rz}{(D+z)^3}dz$$

$$= -\frac{\pi^2\rho^2 CR}{6D} = -A_H\frac{R}{6D}.$$

Note that here the origin of the z-axis was shifted to the surface of the sphere and it was assumed only elementary volumes at $z \ll R$ to contribute significantly to the overall potential energy. Further, it is important to mention that here we defined $A_H = \pi^2 C\rho^2$, the so-called the Hamaker constant, for two bodies with the same number density of molecules enforcing the pair-wise additivity of the energetic contributions thus neglecting any many-body effects. This brutal simplification may be justified for very dilute dipole gases but it is certainly not correct in condensed matter like colloidal particles and even less if the latter are suspended in a dielectric medium, where a damping of the molecular interaction fields occurs. However, it turns out that the more rigorous treatment by the Lifshitz continuum theory results the same distance dependence of the potential, as derived above, if the Hamaker constant is expressed in terms of the dielectric properties of the involved materials:

$$(1.41) \qquad A_H \approx \frac{3}{4}k_B T\left(\frac{\varepsilon_1-\varepsilon_3}{\varepsilon_1+\varepsilon_3}\right)\left(\frac{\varepsilon_2-\varepsilon_3}{\varepsilon_2+\varepsilon_3}\right) + \\ + \frac{3h\nu_e}{8\sqrt{2}}\left\{\frac{(n_1^2-n_3^2)(n_2^2-n_3^2)}{(n_1^2-n_3^2)^{1/2}(n_2^2-n_3^2)^{1/2}\left[(n_1^2-n_3^2)^{1/2}+(n_2^2-n_3^2)^{1/2}\right]}\right\}.$$

In the formulation above the first term represents the static contribution where $\varepsilon_1, \varepsilon_2$ are the zero-frequency dielectric constants of two objects and ε_3 the one of the surrounding medium; the second term is representing the contribution of frequency dependent dispersion forces which are approximated by the dominant term which occurs at the main electronic absorption frequency ν_e. The refractive indexes are given by $n_i(\nu) = \sqrt{\frac{\varepsilon_i(\nu)}{\varepsilon_0}}$, where $\varepsilon_i(\nu)$ is the materials frequency dependent dielectric function and ν_e is normally the frequency attributed to the dominant absorption in the UV region of the electro-magnetic spectrum and is of the order of $10^{15} Hz$. The same quantity for metals is the so called Langmuir or plasma frequency, above which the metal becomes transparent to the radiation, in this case the explicit form would be $\nu_e = \sqrt{\frac{n_e e^2}{\varepsilon_0 m_e}}$, where n_e is the electron density and e the elementary charge, ε_0 is the permittivity in the vacuum and m_e is the effective mass of a conduction electron. For most materials in vacuum or air the Hamaker constant is very small, i.e. $A_H = 10^{-20} J \approx 3k_B T$, and it can be reduced drastically if the materials are dispersed in a dielectric surrounding which matches the optical properties of the suspended particles.

1.2 Non-DLVO interactions

1.2.1 Gravitation and light forces

In colloidal suspensions where particles do not exceed the nano-metric size, gravitational contributions are normally disregarded as a contribution to the total pair-wise interaction potential. A new scenario comes about with the use of micro-metric colloids and optical tweezers. In this case the weight of the colloid and the extra push due to the optical pressure of the laser tweezers cannot be neglected in the evaluation of the gravitational contribution. For free colloids in suspension, gravitation is calculated considering the buoyancy correction (Archimedes principle) on the density of the particle from which the solvent density will be subtracted:

$$\vec{F}_G = V_p(\rho_p - \rho_s) \cdot \vec{g} = V_p \rho_{eff} \cdot \vec{g} \tag{1.42}$$

where V_p is the particle volume, $\vec{g}$ is the acceleration of gravity and the symbol ρ now refers to the mass density of particle, subscript p, of the suspending solvent, subscript s, and effective one, subscript eff. Thus, the gravitational contribution to the particle energy is:

$$\Phi_{grav}(h) = -\vec{F}_G \cdot h \tag{1.43}$$

where h is the height of the particle's center of mass above a reference point which can be chosen arbitrarily. As mentioned before, on top of the gravitational potential related to the bare mass of a colloid in suspension, an extra contribution has to be taken into account, coming from the light radiation pressure the tweezers laser exerts on it. As sketched in the figure below, when a laser beam with Gaussian profile is directed over a colloidal particle freely moving in suspension, the object will tend to align its motion along the force gradient and towards the maximum of the intensity distribution, so in the focal point.

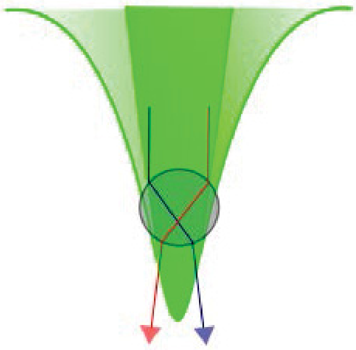

Figure 1-4: Sketch of a particle trapped in a light beam with Gaussian profile. The harrows represent the gradient forces pushing the colloid towards the focal plane.

The light force ($\vec{F}_L$) exerted by the electric-field has its maximum when the particle gets trapped in the focal plane and it is proportional to the ratio between the power of the radiation, namely $\mathcal{P}$, and the speed of light, c [65-67]:

$$F_L \propto \frac{\mathcal{P}}{c}.$$

In our case, the effective force pushing the particle towards the interface will be the sum of the latter two terms, th one related to the particle buoyancy corrected mass and the one due to the light radiation pressure:

$$\Phi_{grav}(h) = \tilde{F}_G \cdot h = \left(F_g + \frac{\mathcal{P}}{c}\mathcal{R}_{sphere}\right) \cdot h \qquad (1.44)$$

where we introduce the effective weigh force, $\tilde{F}_G$, for the convenience of later notation, or the sum of the bare weigh force, F_g, and the light force, F_L. $\mathcal{R}_{sphere}$ is a proportionality constant connected to the Fresnel's coefficients of reflection/absorption of the particle and h its the separation distance from the wall.

More intuitively a laser trap can be pictured as a spring with a stiffness that varies depending on the size ratio between the trapped object and the wave length λ of the trapping laser used. Normally, depending on this ratio and on the value of the material refractive index (n_m), three different regimes can be identified according to the ration of laser wave length and colloidal diameter d:

(1) the Rayleigh regime where $d \ll \lambda/n_m$ and the stiffness increases as r^3
(2) the Mie-Lorentz regime $d \sim \lambda/n_m$;
(3) the Ray-optics regime $d \gg \lambda/n_m$ and the stiffness decays as $1/r$.

As a matter of fact in this investigation, given a λ=532 nm, and particles diameters d=1000, 2000, 3000 and 4000 nm the last two regimes (2 and 3) have to be taken into consideration. Between these two regimes the "ray-optics" (3) is the one expressly chosen for the description of the laser force used in the model (F_L). As for the Mie-Lorentz regime (2), Maxwell's equations need to be solved explicitly to calculate it and this needs to be done via numerical integration [68, 69]. What is already known from the literature is that particles with dimensions comparable to the laser wave length feel a much stronger trapping force as compared to smaller or larger particles [70, 71]. This is very likely the reason why we see deviations of the experimental data obtained with a probe sphere of d=1μm, from the trends set by the data obtained with larger spheres (see Chapter 4).

1.2.2 Depletion forces

The first theoretical formulation of depletion interactions was given by Asakura and Oosawa [30-32] between 1954 and 1959 using as model system a binary mixture of large colloidal spheres, interacting between each other as hard spheres, in a dilute suspension of much smaller polymer coils, treated as an ideal gas where its constituents have no mutual interaction, in other words as phantom spheres. The mixture is taken to be in thermal equilibrium with a thermal bath at given temperature, *T,* therefore both species will undergo Brownian motion with proportional thermal velocity, each of them trying to maximize the accessible free volume in order to minimize the total energy. While moving so, it may happen for the larger colloids to be found so close to each other that no depletant would fit into the gap in between. This will cause the depletant to be unevenly distributed around the larger colloids, thus the collisions due to Brownian motion, will result in a non-zero momentum onto the two spheres pushing them together. Another way to picture the phenomenon is to define, around the two larger colloids, a shell of empty volume called depletion layer, which the centres of mass of the phantoms spheres cannot enter. In this picture the accessible free volume of the system increases if the depletion layers around the large colloids are partially overlapping. Consequently the entropy of the system increases and its free energy decreases leading the system to equilibrium. In their work Asakura and Oosawa investigated pair-wise depletion potentials between spherical colloids induced by differently sized and shaped macromolecules [31], the main assumptions of their model being:

- Low Density Approximation, telling us that if one takes depletants below their overlap concentration, so diluted, then those will follow the laws of ideal gases and mutual interaction can be disregarded;
- Derjaguin Approximation, reminding us that if the interaction potential is short ranged then forces acting between curved surfaces can be calculated as the integral of interaction potentials between flat walls.

The latter is the most crucial approximation to relate measurements and theory in the case of a TIRM set-up, where interaction potentials, between a spherical probe and the wall of the interface below it, are calculated. Thus, to reach an explicit formulation for the depletion interaction potential between a sphere and a wall we will start from the calculation of the same interaction between two walls and then Derjaguin's approximation shall be used.

The depletion interaction potential between two walls induced by rod-like depletants, $\Phi_{dep}^{ww}(D)$, can be calculated as the variation of the free Helmholtz energy of the system, ΔF, due to the approximation of two walls form infinity to a distance D, smaller than the virus length L. Thus, given a system in thermal equilibrium at fixed temperature T, one can write:

$$\Phi_{dep}^{ww} = \Delta F = \Delta U - T\Delta S,$$

where:

$$\Delta U = T\Delta S - \Pi\Delta V = 0 => T\Delta S = \Pi\Delta V.$$

Thus:

$$\Delta F = -\Pi\Delta V$$

where $\Pi = \rho k_B T$ is the osmotic pressure in the system and $\Delta V = V_{ex}(D \to \infty) - V_{ex}(D)$ is the change in free volume accessible to the rods. The latter is defined as the change of excluded volume to the rods center of mass given their orientation due to the hard-body interaction with the walls. Substituting the above mentioned equivalences in the last expression of ΔF, one gets:

$$\Delta F = \Phi_{dep}^{ww}(D) = -\rho k_B T[V_{ex}(D \to \infty) - V_{ex}(D)], \tag{1.45}$$

Or the rods induced depletion interaction potential between two flat walls. For the explicit calculation of the excluded volumes one needs to start defining the geometry of the problem as precisely as possible. Considering for example a rod-like particle of total length L, the volume unavailable for the rod's centre of mass given its orientation, changes if there one or two walls to consider.

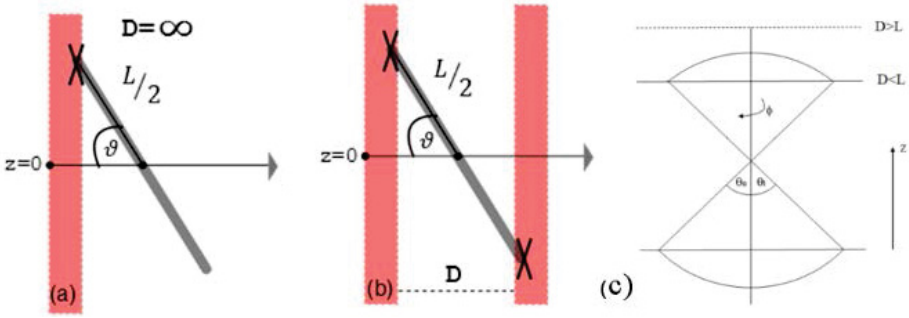

Figure 1-5 Sketch of the geometry for the calculation of the excluded volume to a rod centre of mass in the case of two walls at infinite separation distance (a) and at finite separation distance D (b) together with a sketch about the integration limits of the rotational angle, ϑ (c).

The volume excluded for a single rod of length L facing a single wall can be calculated as:

$$V'_{ex} = \int dr^3 \int d\Omega \frac{1}{4\pi}\left(1 - e^{-\frac{u(r,\Omega)}{k_B T}}\right) \tag{1.46}$$

where $\frac{u(r,\Omega)}{k_B T}$ is the hard body potential between the rod and the wall. Consequently the integral has a non-zero value solely when the rod is touching the wall, meaning that the term $1 - e^{-\frac{u(r,\Omega)}{k_B T}} = 1$. In the latter equation the first integral is the one over all the possible positions for the rod center of mass, while the second integral is the fraction of the spherical unit volume which is not accessible to it when it is close enough to the walls. Figures (1.5)(a) and (b), picture a rod facing a single wall and confined between two walls respectively, projected on a 2D space. In the case of a single rod facing a single wall (Fig(1-5)(a)), the conditions for a rod touching the wall are for $z \leq \frac{L}{2}$ and for $0 \leq \vartheta \leq \vartheta_l$, or $\vartheta_u \leq \vartheta \leq \pi$ (see Fig.(1-5)(c)), thus:

$$V'_{ex}(D \rightarrow \infty) = \frac{1}{4\pi} \int dx \int dy \int_0^{L/2} dz \int_0^{2\pi} d\phi \left[\int_0^{\vartheta_l} d\vartheta\, sin\vartheta + \int_\pi^{\vartheta_u} d\vartheta\, sin\vartheta \right]$$

If now the two plates come within a distance $D \leq L$, like shown in Figure 1-5)(b), the excluded volumes from the two plates overlap describing therefore a reduction of the total excluded volume. $V_{ex}\,(D)$ is calculated in the same way as in the case of infinite distance between the walls, but for the upper integration limits. The center of mass coordinate z will now vary between 0 and D but $cos\vartheta_{l,u} = \frac{2z}{L}$ for $z < D/2$ and $cos\vartheta_{l,u} = \frac{2(D-z)}{L}$ for $z > D/2$. To simplify the calculations, one should notice the symmetry of the problem with respect to the distance between the walls, which allows to set the upper integration limit for z to $D/2$ and count the contribution twice, thus getting:

$$V_{ex}\,(D) = \frac{1}{4\pi} \int dx \int dy\, 2 \int_0^{D/2} dz \int_0^{2\pi} d\phi \left[\int_0^{\vartheta_l} d\vartheta\, sin\vartheta + \int_\pi^{\vartheta_u} d\vartheta\, sin\vartheta \right] \tag{1.47}$$

The integration over dz yields in both cases $2(z - \frac{z^2}{L})$, the integration along $d\phi$ yields always 2π, while the integration over dx and dy gives identically the area of the walls, namely A. Thus, it follows:

$$\begin{aligned} V'_{ex}(D \rightarrow \infty) &= A(z - \frac{z^2}{L})\Big|_0^{L/2} = A\frac{L}{4} \\ V_{ex}\,(D) &= 2\,A(z - \frac{z^2}{L})\Big|_0^{D/2} = A\left(D - \frac{D^2}{2L}\right). \end{aligned} \tag{1.48}$$

For a correct calculation of Eq. (1.49) in the case of two walls, one needs to multiply the previously calculated $V'_{ex}(D \to \infty)$ by a factor two, so to account for the other wall as well, while $V_{ex}(D)$ accounts already for symmetry:

$$\begin{aligned} \Delta V = V_{ex}(D \to \infty) - V_{ex}(D) = 2V'_{ex}(D \to \infty) - V_{ex}(D) \\ = A\left(\frac{L}{2} - D + \frac{D^2}{2L}\right) \end{aligned} \qquad (1.49)$$

$$\Phi_{dep}^{ww}(D) = -\Pi\Delta V = -\rho k_B T A\left(\frac{L}{2} - D + \frac{D^2}{2L}\right).$$

The latter is the depletion interaction pair-wise potential induced by rods between two planar walls, non-zero strictly assuming $D < L$, but zero otherwise. Once the interaction energy for two flat surfaces is given, the sphere/wall case is calculated via direct application of the Derjaguin approximation. To do so one needs first to transform $\Phi_{dep}^{ww}(D)$ in an energy per unit area, $\gamma_{dep}^{ww}(\mathrm{D})$, thus simply dividing it for A:

$$\gamma_{dep}^{ww}(\mathrm{D}) = \frac{\Phi_{dep}^{ww}}{A} = -k_B T\rho\left(\frac{L}{2} - D + \frac{D^2}{2L}\right). \qquad (1.50)$$

At this point, by recalling Derjaguin's approximation (Eq. (1.37)) and by simple integration of Eq. (1.54) in the appropriate range of distances, so those where the potential interaction is non-zero, one obtains:

$$\begin{aligned} \Phi_{dep}^{sw}(h) = 2\pi R \int_h^L \gamma_{dep}^{ww}(h')dh' \\ = \pi R\rho k_B T \int_h^L \left(\frac{L}{2} - h' + \frac{{h'}^2}{2L}\right) dh' = \\ = -\frac{\pi}{3} R L^2 \rho k_B T \left(1 - \frac{h}{L}\right)^3 \end{aligned} \qquad (1.51)$$

or the depletion interaction potential induced by rods between a sphere and a flat interface in function of separation distance, h. The latter can also be rewritten in in function of the bulk concentration of depletant recalling the substitution $c = \frac{\rho M_{rod}}{N_A}$, where N_A is the Avogadro number, ρ is the bulk density of the rods and M_{rod} their mass, so that:

$$\frac{\Phi_{dep}^{sw}(h)}{k_B T} = -\frac{\pi}{3}\frac{cN_A}{M_{rod}} RL^2 \left(1 - \frac{h}{L}\right)^3. \tag{1.52}$$

This last formulation is the depletion interaction model potential used in this experimental study for the data evaluation.

1.2.3 Hydration forces

Hydration forces are known as an additional contribution to the basic DLVO potential, in picturing the stability of proteins systems [34]. Such forces arise from the rearrangement of water molecules around the proteins in forming a steric-like layer providing stabilization. The thickness of such layer depends directly on the charge of the ions in solution and their polarizability and this region, where the solvent modifies its structure and its properties, is called *solvation zone.* Being due to polarization effects, this rearrangement of solvent molecules around the solute is expected to propagate but at the same time to vanish exponentially within very small distances in the order of few nano-meters (~1 nm to 2 nm). In the case of monovalent ions and sphere/wall interaction the interaction potential due to an hydration layer between equally coated surfaces has been described phenomenologically by:

$$\frac{\phi_{protein}^{sw}}{k_B T}(h) = C_H \exp(-\frac{h}{\lambda}) \tag{1.53}$$

Where C_H is the amplitude of the interaction; h the distance between the two surfaces and $\frac{1}{\lambda}$ the inverse length of the hydration layer defining as well the range of the interaction. Such forces remain though very difficult to predict and describe theoretically because those arise from highly specific solute-solvent and modified solvent-solvent interactions working at molecular level for which the latter is a crude approximation.

1.3 Sphere-Wall Total Interaction Energy

At this point all the interactions governing the static properties of a colloid levitated on top of an interface and trapped with optical tweezers have been mentioned and explained. So knowing which energetic contributions are involved, the total interaction potential in the case of a depletant-free suspension can be written as:

$$\frac{\Phi_{tot}^{sw}(h)}{k_B T} = \frac{\Phi_{el}^{sw}(h)}{k_B T} + \frac{\Phi_{vdw}^{sw}(h)}{k_B T} + \frac{\Phi_{grav}^{sw}(h)}{k_B T} \tag{1.54}$$

where $\frac{\Phi_{el}^{sw}(h)}{k_B T}$ is the energetic contribution due to electrostatic repulsion, $\frac{\Phi_{vdw}^{sw}(h)}{k_B T}$ the one due to Van der Waals attraction and $\frac{\Phi_{grav}^{sw}(h)}{k_B T}$ is the gravitational contribution, taken with positive sign in case the direction of the gravity force is normal to the wall. Here and in all further experimental considerations, the separation distance between the wall and the probe sphere is termed h.

When a second colloidal species, the depletant in this case, is added in suspension, the former total energy gains a fourth term, $\frac{\Phi_{dep}^{sw}(h)}{k_B T}$, the depletion interaction, as shown by the blue line in Fig. (1-6), thus by linear additivity:

$$\frac{\Phi_{tot}^{sw}(h)}{k_B T} = \frac{\Phi_{el}^{sw}(h)}{k_B T} + \frac{\Phi_{vdw}^{sw}(h)}{k_B T} + \frac{\Phi_{grav}^{sw}(h)}{k_B T} + \frac{\Phi_{dep}^{sw}(h)}{k_B T} \tag{1.55}$$

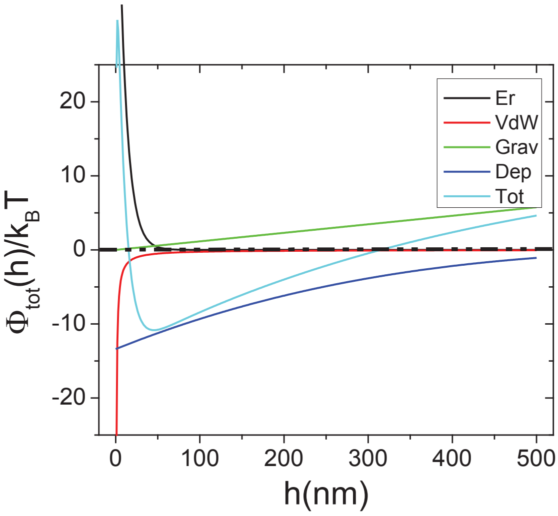

Figure 1-6 Plot of all the energetic contributions explained so far: electrostatic repulsion (black), Van der Waals attraction (red), gravitational contribution (green), Depletion (blue) and the total interaction potential resulting from the sum of the four (light-blue).

In this experimental investigation, for all the suspensions used to study depletion interactions, the Van der Waals attractive contributions were strongly damped: $\frac{\Phi_{vdw}^{sw}(h)}{k_BT} \sim 0$ so the total interaction energy was indeed the sum of three terms: electrostatic repulsion, gravitation and depletion.

$$\frac{\Phi_{tot}^{sw}(h)}{k_BT} = Bexp\{-\kappa_D \cdot h\} + \tilde{F}_G \cdot h - \frac{\pi}{3} RL^2 \rho \left(1 - \frac{h}{L}\right)^3. \tag{1.56}$$

In the case of protein-protein non-specific interactions the aim was to prove Hydration was competing against the Van der Waals attractive potential neutralizing it, thus the total interaction energy was this time the sum of four terms:

$$\frac{\Phi_{tot}^{sw}(h)}{k_BT} = \frac{\Phi_{el}^{sw}(h)}{k_BT} + \frac{\Phi_{vdw}^{sw}(h)}{k_BT} + \frac{\Phi_{grav}^{sw}(h)}{k_BT} + \frac{\Phi_{protein}^{sw}(h)}{k_BT} \tag{1.57}$$

i.e. electrostatic repulsion, gravitation, Van der Waals attraction and hydration.

Eqs. (1.56) and (1.57) are the model interaction potentials used in the current investigation to fit the experimental data to the theory.

The following section will focus instead on other important insights in investigating a colloidal system from a dynamical point of view, thus the latest theories and models about the dynamics of a colloid in a close vicinity of an interface will be explained.

1.4 Near wall dynamics of colloids in suspension measured by TIRM

As will be discussed in more detail in chapter 2, total internal reflection microscopy (TIRM) allows for a determination of the separation distance, h, of a probe sphere from a glass wall with nm-resolution. This by measuring the time trace of the intensity scattered by the particle and making use of the fact the latter is described as exponentially decaying with distance due to the evanescent nature of the field the particle is immersed in. The measurement principle is based on the use of an evanescent wave, which has a penetration depth Λ^{-1}, as the illumination source. Moreover, if the separation distance can be measured with high enough time resolution, TIRM data can also be used for the evaluation of the near-wall dynamics of the investigated system. In this respect, Bevan and Prieve have shown how auto-correlation functions of the scattered intensity from the probe can be used to derive a diffusion coefficient normal to the interface, $< D_n^{TIRM} >$, averaged over the separation distances covered by the illuminated scattering volume. The latter is a quantity related to the Einstein's bulk diffusion coefficient, D_0, via a function that describes the hydrodynamic slow-down of the colloid due to the presence of a near interface. In this chapter we start with a brief overview of the dynamic theory carried out by Frej and Prieve [63] at first and then revisited by Bevan and Prieve [64]. Then we will continue with theory of our thinking that allows instead the calculation of dynamic quantities not averaged in space, like mean displacements and mean-square displacements at given heights.

1.4.1 Auto-correlation functions

The time auto-correlation function of the scattered intensity (ITACF) is generally defined as

$$R(\tau) = \lim_{T\to\infty}\left\{\frac{1}{T}\int_0^T I(t)I(t+\tau)dt\right\} \qquad (1.58)$$

where T is the total measurement time and τ.

Taking into account that because the particle's separation distance from the wall changes with time the scattered intensity fluctuates accordingly and the system is is thermal equilibrium, one can exploit the ergodicity principle to simplify the integration by substituting the integration variable over all different positions of the colloid centre of mass, $z = h + R$, defined as the shortest distance to the wall surface, given an initial position z_0, weighed on the probability of occurrence they have. Thus, let $P(z, z_0|\tau)dz$ be the conditional probability of finding the sphere at some elevation between z and $z + dz$ at time $t + \tau$, given that it was at elevation z_0 at time t. Then the product $P(z_0)dz_0P(z, z_0|\tau)dz$ is the probability of some initial elevation z_0 followed by some final elevation z after a delay time τ, and integrating over all possible initial and final elevations, it gives the autocorrelation function:

$$R(\tau) = \int_R^\infty dz_0 \int_R^\infty I(z)I(z_0)P(z, z_0|\tau)p(z_0)dz \qquad (1.59)$$

The conditional probability density $P(z, z_0|\tau)$ has to satisfy the following specific conditions:

1. $P(z, z_0|\tau)$ and $p(z_0)$ will vanish for distances $z < R$;
2. $P(z, z_0|0) = \delta(z - z_0)$, meaning that the particle's position is well known at $\tau = 0$, from which it directly follows: $R(0) = \int_R^\infty I^2(z_0)p(z_0)dz_0 =< I^2 >$, which is basically the weighing factor at a fixed height;
3. $P(z, z_0|\infty) = p(z)$ where $p(z)$ is the Boltzmann probability distribution, from which it follows that $R(\infty) = \left(\int_R^\infty I(z)p(z)dz\right)^2 =< I >^2$;
4. $P(z, z_0|\tau)$ must be a solution for the Smoluchowski equation:

$$\frac{\partial P}{\partial \tau} = \frac{\partial}{\partial z}\left[D(z)\left(\frac{\partial P}{\partial z} - \beta F(z)P\right)\right] \qquad (1.60)$$

where we use $\beta = 1/k_BT$ and $P \equiv P(z, z_0|\tau)$ for the convenience of notation. In the vicinity of a wall, the diffusion coefficient $D(z)$ and the force acting on the particle $F(z) = -d\Phi(z)/dz$ both depend on the particle's vertical position z.

In their later paper Bevan and Prieve showed that the initial slope of the auto-correlation function can be calculated without making any assumption on the explicit form of the conditional probability density and the role of a particle drift velocity, which will be imposed by the external force. The only constrain needed is the assumption that the particle mobility becomes zero for a particle touching the wall, which corresponds to so called stick boundary conditions in hydrodynamics. In the following we will outline the derivation of an expression for the derivative of the correlation function in the limiting case of $\tau \to 0$. The only time dependent term in Eq. (1.60) is the conditional probability. Therefore the derivative can be written as:

$$R'(\tau) = \int_R^\infty dz_0 I(z_0) p(z_0) \int_R^\infty dz I(z) P'(\tau) \tag{1.61}$$

where, here and in the following, a prime will denote a derivative with respect to the indicated variable, i. e. $u'(x) = \partial u(x, y, \ldots)/\partial x$. Now, introducing Eq. (1.60) for P' results:

$$\int_R^\infty dz I(z) P'(\tau) = \int_R^\infty dz I(z) \frac{\partial}{\partial z}\left[D(z)\left(\frac{\partial P}{\partial z} + \beta \Phi'(z) P\right)\right] \tag{1.62}$$

where we use $F(z) = -\Phi'(z)$. The right hand side of Eq. (1.62) can be integrated by parts, thus:

$$\begin{aligned} \int_R^\infty dz I(z) P'(\tau) &= \\ &= I(z) D(z) [P'(z) + \beta \Phi'(z) P]|_R^\infty \\ &- \int_R^\infty dz I'(z) D(z)\, [P'(z) + \beta \Phi'(z) P]. \end{aligned} \tag{1.63}$$

As mentioned before, due to the evanescent nature of the illumination, we may assume that the scattering intensity is exponentially sensitive to the elevation, say $I(z) = I_0 e^{-\Lambda z}$ with $I'(z) = -\Lambda \mathrm{I}(z)$. Further the diffusion constant $D(R) = 0$ when the sphere touches the wall at $h = 0$. Therefore the boundary terms vanish and the remaining integral can be split in two parts:

$$\int_R^\infty dz I(z) P'(\tau) = \Lambda\left[\int_R^\infty dz I(z) D(z) P'(z) + \int_R^\infty dz I(z) D(z) \beta \Phi'(z) P\right] \tag{1.64}$$

where the term after the first equality can be integrated by parts again to give:

$$\int_R^\infty dz I(z) D(z) P'(z) = -\Lambda \int_R^\infty dz I(z)[D'(z) - \Lambda \mathrm{D}(z)]P \tag{1.65}$$

Introducing this result into Eq. (1.64) yields:

$$\int_R^\infty dz I(z) P'(\tau) = = \Lambda \int_R^\infty dz I(z) P[\mathrm{D}(z)\beta\Phi'(z) - D'(z) + \Lambda \mathrm{D}(z)]. \tag{1.66}$$

Thus now, recalling that $P(z, z_0|0) = \delta(z - z_0)$ and making use of the properties of delta-function, this integral can be easily evaluated as follows:

$$\int_R^\infty dz I(z) P'(\tau) = \Lambda I(z_0)[\mathrm{D}(z_0)\beta\Phi'(z_0) - D'(z_0) + \Lambda \mathrm{D}(z_0)]. \tag{1.67}$$

Thus, the derivative of the correlation function for short delay times, $\lim_{\tau\to 0} R'(\tau) \equiv R'(0)$, by simple substitution of the latter becomes:

$$R'(0) = \Lambda \int_R^\infty dz_0 I^2(z_0)[\mathrm{D}(z_0)\beta\Phi'(z_0) - D'(z_0) + \Lambda \mathrm{D}(z_0)]p(z_0). \tag{1.68}$$

Since we do not need to distinguish anymore between z and z_0 we will drop the subscript further on. The part of the integral containing $\mathrm{D}(z)\beta\Phi'(z)$ can be integrated by parts again, using that $p(z)$ is a Boltzmann distribution and consequently $p'(z) = -\beta\Phi^{'}(z)p(z)$. Therefore we may write:

$$\begin{aligned} &\int_R^\infty dz I^2(z)\mathrm{D}(z)\beta\Phi'(z)p(z) \\ &\qquad = -I^2(z)\mathrm{D}(z)p(z)|_R^\infty - \int_R^\infty dz I^2(z)\mathrm{D}(z)p'(z) \\ &\qquad = \int_R^\infty dz[I^2(z)D'(z) - 2\Lambda I^2(z)D(z)]p(z). \end{aligned} \tag{1.69}$$

The boundary part is again vanishing, and introducing the remaining integral back into Eq. (1.68) gives the final result:

$$R'(0) = -\Lambda^2 \int_R^\infty dz I^2(z)\mathrm{D}(z)p(z) \tag{1.70}$$

for the derivative of the correlation function at very short times. It is important to note that the terms containing the derivative of the position dependence of the diffusion coefficient cancelled out. Recalling now that $R(0) = \int_R^\infty I^2(z)p(z)dz$ we may now define a diffusion coefficient normal to the wall, averaged over positions:

$$\langle D_n^{TIRM}\rangle = \frac{\int_R^\infty dz I^2(z)\mathrm{D}_n(z)p(z)}{\int_R^\infty I^2(z)p(z)dz} = -\Lambda^{-2}\frac{R'(0)}{R(0)}, \tag{1.71}$$

which can be determined using time resolved intensity measurements in total internal reflection microscopy. Here the subscript *n* indicates that strictly speaking only the particle diffusion normal to the wall is probed, since only particle motion in this direction will lead to a change in scattering intensity.

Normally, for the comparison of experimental data with theoretical predictions, the well-established expression by Honig [72] and co-workers is used:

$$\frac{D_n(z)}{D_0} = f_n(h) = \frac{6h^2 + 2Rh}{6h^2 + 9Rh + 2R^2} \tag{1.72}$$

Where D_0 is the free particles' diffusion coefficient in bulk environment. Eq. (1.72) is a very good approximation for the much more complicated exact expression by Brenner and co-workers [73, 74]:

$$f_n(\alpha) = \left[\frac{4\sinh(\alpha)}{3}\sum_{n=1}^{\infty}\frac{n(n+1)}{(2n-1)(2n+3)} \times \right. \\ \left. \times \left\{\frac{2\sinh[(2n+1)\alpha] + (2n+1)\sinh(2\alpha)}{2sinh^2\left[(n+\frac{1}{2})\alpha\right] - [(2n+1)\sinh(\alpha)]^2} - 1\right\}\right]^{-1} \tag{1.73}$$

where $\alpha = cosh^{-1}(\frac{z}{R})$ and again $z = h + R$.

There are however two major drawbacks to this analysis of the dynamic information contained in TIRM data. Strictly speaking Eq. (1.71) and the following are only correct for $\tau = 0$. As Bevan and Prieve point out in their paper, it is therefore not clear how short delay times have to be chosen, to allow for neglecting the derivative of the position dependent diffusion coefficient and the drift velocity. Further, this method will always result dynamic data spatially averaged over the whole illumination volume. To overcome these shortcomings we will derive expressions for the spatially resolved drift velocities and diffusion coefficients in the following section, through the calculation of mean displacements and mean square displacements at given heights.

1.4.2 Mean Displacement and Mean Square Displacement at given heights

Another way to address dynamic properties of a colloidal system in general is through the calculation of two dynamical averages called mean displacement (MD) and mean square displacement (MSD). As we will see, these are related to the particle drift velocity and the diffusion coefficient at a given starting position. In terms of the above introduced conditional probability density function, $P(z, z_0|t)$, the mean displacement is defined as:

$$m(t, z_0) \doteq < z - z_0 >= \int_R^{\infty} dz(z - z_0)P$$

where $P \equiv P(z, z_0|t)$ is used again, for convenience of notation. In this definition, P is the only time dependent quantity. Therefore, the derivative of the time evolution of the mean displacement at a given starting position can be formulated using the Smoluchowski equation and evaluated via integration by parts.

$$\frac{dm(t, z_0)}{dt} = \int_R^{\infty} dz(z - z_0)\frac{\partial}{\partial z}\left\{D_n(z)\left[\frac{\partial P}{\partial z} - \beta F(z)P\right]\right\} =$$

$$= -\int_R^{\infty} dz D_n(z)\left[\frac{\partial P}{\partial z} - \beta F(z)P\right] = \tag{1.74}$$

$$= \int_R^{\infty} dz P\left[\frac{dD_n(z)}{dz} + \beta D_n(z)F(z)\right] = < v(z) >.$$

In the latter we identify the last integral term as the definition of the spatial average of a position dependent drift velocity, which we thus define as:

$$v(z) = \frac{dD_n(z)}{dz} + \beta D_n(z)F(z) \tag{1.75}$$

where the first term reflects an apparent velocity caused by the fact that the diffusive motion towards the wall is slower than away from it, according to Eq. (1.72). The second term is the velocity due the external force by which the particle is affected.

The same procedure of partial integration can be used also to obtain the mean-square displacement. Therefore defining it as $W(t, z_0) =< (z - z_0)^2 >$ one can write:

$$\frac{dW(t, z_0)}{dt} = \int_R^{\infty} dz(z - z_0)^2\frac{\partial}{\partial z}\left\{D_n(z)\left[\frac{\partial P}{\partial z} - \beta F(z)P\right]\right\} =$$

$$= -2\int_R^{\infty} dz(z - z_0)D_n(z)\left\{\frac{\partial P}{\partial z} - \beta F(z)P\right\} = \tag{1.76}$$

$$= 2\int_R^\infty dzP\{D_n(z) + (z - z_0)v(z)\} = 2 < D_n(z) + (z - z_0)v(z) >,$$

where the first term describes the diffusive contribution while the second term takes into account migration. For small times, where both the mean displacement and the mean square displacement have very little variations around fixed heights z_0, then one can Taylor expand both the drift velocity and the normal diffusion coefficient:

$$v(z) = v(z_0) + (z - z_0)\frac{dv(z_0)}{dz_0} + \frac{1}{2}(z - z_0)^2\frac{d^2z_0}{{dz_0}^2} + \cdots$$

$$D_n(z) = D_n(z_0) + (z - z_0)\frac{dD_n(z_0)}{dz_0} + \frac{1}{2}(z - z_0)^2\frac{d^2D_n(z_0)}{{dz_0}^2} + \cdots$$

By introducing these expansions into Eqs. (1.74) and (1.76) respectively and subsequent calculation of the integrals, we obtain:

$$\frac{dm(t,z_0)}{dt} = v(z_0) + m(t,z_0)\frac{dv(z_0)}{dz_0} + \frac{1}{2}W(t,z_0)\frac{d^2v(z_0)}{{dz_0}^2} + \cdots \tag{1.77}$$

$$\begin{aligned}\frac{dW(t,z_0)}{dt} &= 2D_n(z_0) + 2m(t,z_0)\left\{\frac{dD_n(z_0)}{dz_0} + v(z_0)\right\} + \\ &+ 2W(t,z_0)\left\{\frac{1}{2}\frac{d^2D_n(z_0)}{{dz_0}^2} + \frac{dv(z_0)}{dz_0}\right\}.\end{aligned} \tag{1.78}$$

A formulation for the time dependence of the mean displacement and the mean squared displacement can be obtained by applying the following formal scheme

$$m(t,z_0) = a_{11}t + a_{12}t^2$$

$$W(t,z_0) = a_{21}t + a_{22}t^2,$$

calculating the time derivatives and comparing coefficients, eventually leads to:

$$m(t, z_0) = v(z_0)t + \frac{1}{2}\left\{v(z_0)\frac{dv(z_0)}{dz_0} + D_n(z_0)\frac{d^2v(z_0)}{{dz_0}^2}\right\}t^2 \qquad (1.79)$$

and

$$\begin{gathered} W(t, z_0) = 2D_n(z_0)t + \\ + \left\{v(z_0)\left[\frac{dD_n(z_0)}{dz_0} + v(z_0)\right] + D_n(z_0)\left[\frac{d^2D_n(z_0)}{{dz_0}^2} + 2\frac{dv(z_0)}{dz_0}\right]\right\}t^2. \end{gathered} \qquad (1.80)$$

The limit of both equations for very short times, yields the first order approximation for the mean displacement and mean square displacement:

$$\begin{gathered} \lim_{t\to 0} m(t, z_0) = v(z_0)t \\ \lim_{t\to 0} W(t, z_0) = 2D_n(z_0)t \end{gathered} \qquad (1.81)$$

With this we have a recipe for the determination of spatially resolved drift velocities and diffusion coefficients at hand, which comprises the following steps:

1. transformation of the scattered intensity vs. time trace into a position vs. time trace by use of $I(z) = I_0 e^{-\Lambda z}$;
2. selection of a starting position z_0 and determination of the moments of the displacement distribution after a given time interval according to $m(t, z_0) =< z(t) - z_0 >$ and $W(t, z_0) =< (z(t) - z_0)^2 >$;
3. plot of the MD and MSD versus time and determination of the initial slopes by linear regression.

2 Total Internal Reflection Microscopy

Introduction

Total Internal Reflection Microscopy (TIRM) is a scattering technique based on the principle of total internal reflection. It consists in the production of an evanescent wave across an interface, devised for the direct evaluation of interaction potentials between a single colloid, diffusing on top of an interface, and the interface itself. In this section we describe the basic theory of *Total Internal Reflection* (2.1), the experimental set-up (*Experimental Set Up* (2.1.1)) and the measurement technique (*Experimental Methods* (2.1.2)) in detail.

2.1 Total Internal Reflection

The path of an electro-magnetic wave travelling between two media with different refractive index is defined by Snell's law, which tells us how an incident beam is refracted at the interface into a second medium according to the following equation:

$$n_1 sin(\theta_1) = n_2 sin(\theta_2) \tag{2.1}$$

where n_1 and n_2 are the refractive indexes of the two media, θ_1 is the incident angle, θ_2 the refractive angle. If $n_2 < n_1$, an angle of incidence exists, called the critical angle (θ_C), for which the refracted beam will run exactly along the interface ($\theta_2 = \frac{\pi}{2}$):

$$\theta_C = arcsin\left(\frac{n_2}{n_1} sin(\theta_2)\right) = \arcsin(\frac{n_2}{n_1}) \tag{2.2}$$

For all angles greater than the critical one total internal reflection will occur, which means that the interface is no longer refracting the incident beam but reflecting it completely. Yet Maxwell's equations do not allow for an abrupt drop of the electric field to zero on the other side of the interface, which is why there an evanescent wave will form instead. Considering an electro-magnetic field described by a planar wave:

$$E(\vec{r}, t) = \vec{E}_0 \exp -\mathrm{i}\,(\omega t - \vec{k} \cdot \vec{r}) \tag{2.3}$$

where $\vec{E}_0$ is the amplitude of the field, ω is the frequency and $\vec{k}$ is the wave vector.

$$\overrightarrow{k_J} = \frac{2\pi n_i}{\lambda_0} \cdot \hat{k} = |\vec{k}| cos\theta_j \cdot \hat{z} + |\vec{k}| sin\theta_j \cdot \hat{y} \tag{2.4}$$

where λ_0 is the vacuum wave length, $\hat{z}$ is the unit vector normal to the reflecting interface and $\hat{y}$ the unit vector along the projection of the incident beam onto the reflecting interface. If we apply Snell's law to evaluate $\overrightarrow{k_2}$, it follows that:

$$sin\theta_2 = \frac{n_1}{n_2} sin\theta_1 \tag{2.5}$$

and recalling:

$$\cos(\theta_2) = \sqrt{1 - \sin^2(\theta_2)} = \sqrt{1 - \left(\frac{n_1}{n_2}\right)^2 \sin^2(\theta_1)} = iZ. \tag{2.6}$$

With the latter equations we can calculate $\overrightarrow{k_2}$ and then substitute it into the plane wave solution:

$$E_2(\vec{r}, t) = \overrightarrow{E_{02}} \exp(-i\omega t - k_2 Z z \cdot + i k_2 \frac{n_1}{n_2} \sin(\theta_1) y) \tag{2.7}$$

$$E_2(\vec{r}, t) = \overrightarrow{E_{02}} \exp(-i(\omega t - k_2 y)) \exp(-k_2 Z z).$$

Finally, Eq. (2.7) describes and electro-magnetic field exponentially decaying along the z direction while travelling along the interface in the $\hat{y}$ direction. The sketch in Figure (2-1) below, helps to understand what happens at the moment of total internal reflection, which is the case of $\theta_i > \theta_c$ painted in red, and gives a rough indea of an evanescent wave.

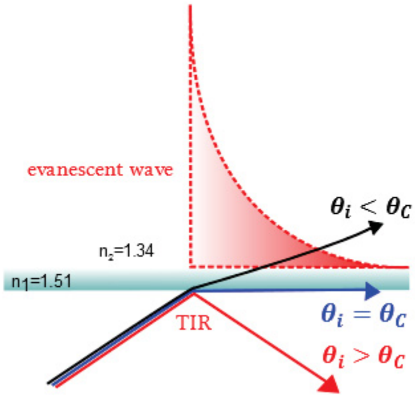

Figure 2-1 Sketch of the transmission of an electro-magnetic wave across an interface framed along the y-z plane: refraction (black), critical angle (blue), total internal reflection and evanescent wave (red).

Experimentally what can be monitored is the intensity of such field, in other words its modulus squared:

$$I_2(\vec{r},t) = |E_2(\vec{r},t)|^2 = \left|\overrightarrow{E_{02}}\right|^2 \exp(-2Zkz) = I_{02}\exp(-\Lambda \cdot z). \tag{2.8}$$

Recalling the definition of Z from Eq. (2.6) we obtain a relation between the penetration depth of the evanescent wave Λ^{-1} and the optical properties of the adjacent media:

$$\Lambda = \frac{4\pi n_2}{\lambda_0}\sqrt{\left(\frac{n_1}{n_2}\right)^2 \sin^2(\theta_1) - 1} = \frac{4\pi}{\lambda_0}\sqrt{{n_1}^2 sin^2(\theta_1) - {n_2}^2} \tag{2.9}$$

Thus meaning that the penetration depth can be tuned by specific choices of refractive indexes and angles of incidence of the light source.

2.1.1 Experimental Set-Up

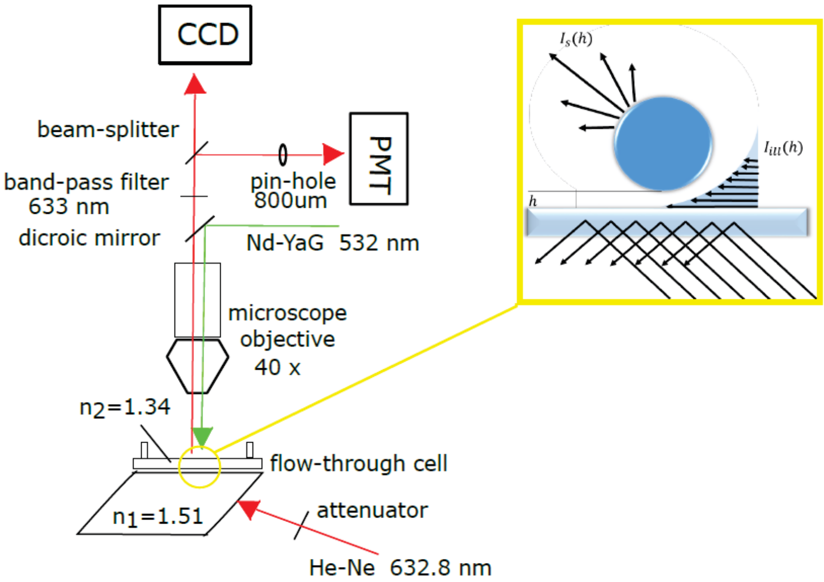

Figure 2-2 Sketch of a typical TIRM set-up with a cartoon showing the magnification of the measuring volume.

The sketch above represents the TIRM set-up used in our experiments with its most important details. The entire set-up is homebuilt from standard microscopy components (Olympus) mounted on an X-95 rail system (Linos). From the bottom side up: a BK7-glass prism (Edmund Optics) is attached to a flow-through cell (Hellma QS137), of 540 µl volume, and optically matched to it via refractive index matching oil. The prism is used to refract the incident beam so that it will hit the interface with the required angle for total internal reflection to occur. In this way an evanescent wave is produced across the interface as shown in the following sketch:

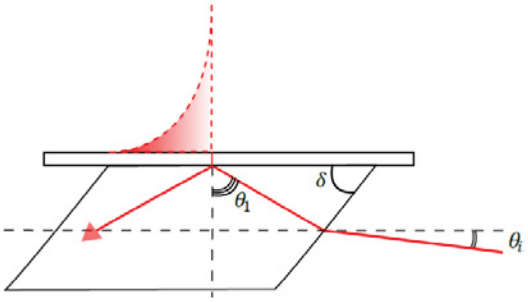

Figure 2-3 Sketch of the refraction due to the prism: geometry for the evaluation of the effective incident angle $\boldsymbol{\theta_i}$via the incident angle on the prism side $\boldsymbol{\theta_l}$ knowing the prism is of an angle $\delta=\frac{\pi}{4}$.

Thus, for total internal reflection to occur, it is crucial to know at which angle the incident beam must hit the prism in order to get the appropriate inner incident angle, so:

$$\theta_i = \delta + arcsin\left[\frac{\sin(\pi/2 - \delta - \theta_l)}{n_1}\right] \quad (2.10)$$

where θ_{i} is the real angle at which the incident beam will hit the interface, while θ_l is the angle, the incident beam describes with respect to the reflecting interface; δ is the 45° angle of the prism and n_1 is the refractive index of the material (quartz glass in this case so $n_1 = 1.55$). Proceeding along the set-up, as shown in Figure (2-2), on top of the prism there is a flow through cell fitted with two small pipes for in- and outlet, one of which can be connected to a syringe equipped with a valve via highly chemically resistive tubing (Saint Gobain Tygon 2075) for load the samples and exchanging solutions. Immediately above the measuring volume an infinity corrected 40x Olympus SLCPlanFI objective, with a focal length f=6.5-8.3 mm and numerical aperture NA=0.55, is used both ways to couple in a 532 nm tweezers laser (Coherent Verdi V2 solid state Nd:Yag laser) and to collect the scattered intensity from the colloidal probe. The illumination source for the scattering experiment is a 15 mW HeNe p-polarized laser with $\lambda_0 = 632.8$nm. The use of a polarized laser and the choice of a suitable penetration depth are very important requirements to minimize the back reflection of light which is scattered by the colloidal particle into the direction of the surface. Interference of scattered light with back reflected light could lead to standing waves, which can result in a significant deviation of the illumination strength profile from the ideal exponential shape. This effect would show as a distortion of the measured interaction potential in the form of undulations along the potential profile [75-77]. In order to further ensure that the collected scattered intensity be solely the p-polarized one, analysers specific for p-polarized light are mounted in front of both detectors (CCD camera and PMT). Moreover, on top of the microscope objective, a dichroic mirror is used to reflect the tweezers laser light away from the detectors while allowing the scattered red light to pass through, reaching PMT and CCD camera simultaneously thanks to a 50/50 beam splitter. Additionally a 633 nm band-pass filter is placed in front of the beam splitter to further purify the transmitted signal from unwanted transmitted green light. Ultimately, on the very top and far-right side of the set-up are the detectors. The CCD camera is a highly sensitive EM-gain camera, which can also be a detector but in this experiment is mainly used to visualize and select a suitable colloidal probe. The PMT is a Hamamatsu H7421-40 operated in the photon-counting mode. According to the number of detected photons, the PMT produces TTL pulses so that intensity is measured in terms of photon count rates. Those pulses are recorded by a digital counter card (National Instruments NI-6602) and then processed by homemade acquisition software which allows also for automating measurement series. A pin-hole of 1mm is mounted in front of the PMT as spatial filter to reduce the probability of collecting scattered intensity collection from other probes in the surroundings of the trapped one or simply to increase the signal to noise ratio by decreasing the amount of detected background signal. The picture in Figure (2-4) are an example of a bright field image (Fig. (2-4), left side) of a 3 μm in diameter probe sphere trapped by the tweezers laser and a direct imaging of its scattering from the evanescent wave (Fig. (2-4)(b), right side).

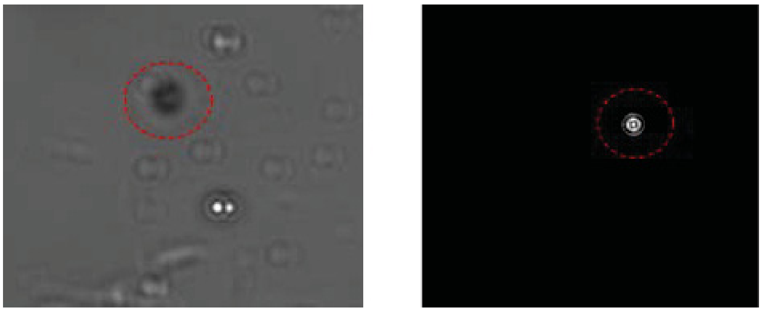

Figure 2-4 Particles respectively in direct (left) and evanescent field (right) illumination. The first picture is the shadow projected by the particle trapped by the tweezers; the second picture is the scattering due to the evanescent wave. Both images are visualized by the CCD camera.

2.1.2 Experimental Method

Total Internal Reflection Microscopy (TIRM) is a well-established scattering technique, devised by Prieve and co-workers in 1999 [10], for the direct evaluation of the interaction potential between interface on top of which is levitated, by monitoring its Brownian motion with an evanescent wave. The basic assumption of a TIRM experiment is that the scattered intensity from a colloidal object immersed in an exponentially decaying field, will still be described by an exponential decay:

$$I_{ill}(h) \propto I_s(h) = I_{0s} \exp(-\Lambda \cdot h) \tag{2.11}$$

where I_{0s} is the intensity scattered from a particle at zero elevation from the interface, $I_s(h)$ is the scattered intensity at the given separation distance h from the interface and $I_{ill}(h)$ is the intensity of the incident exponentially decaying illumination field. From the same formulation and by a simple inversion the separation distance can be evaluated as follows:

(2.12) $$h = \frac{1}{\Lambda}\ln(\frac{I_{0s}}{I_s})$$

from which it stems that the measurement of the intensity of a particle stuck at the interface (I_{0s}) is necessary to rescale and reference the measured scattered intensities with respect to the zero elevation distance and on an absolute scale. During a regular TIRM experiment the intensity trace of a single particle, free to move just along the normal direction to the interface, is recorded over time. From the latter a histogram of scattered intensities gets calculated automatically, like shown in Figure (2-5)(a) and (b), immediately below.

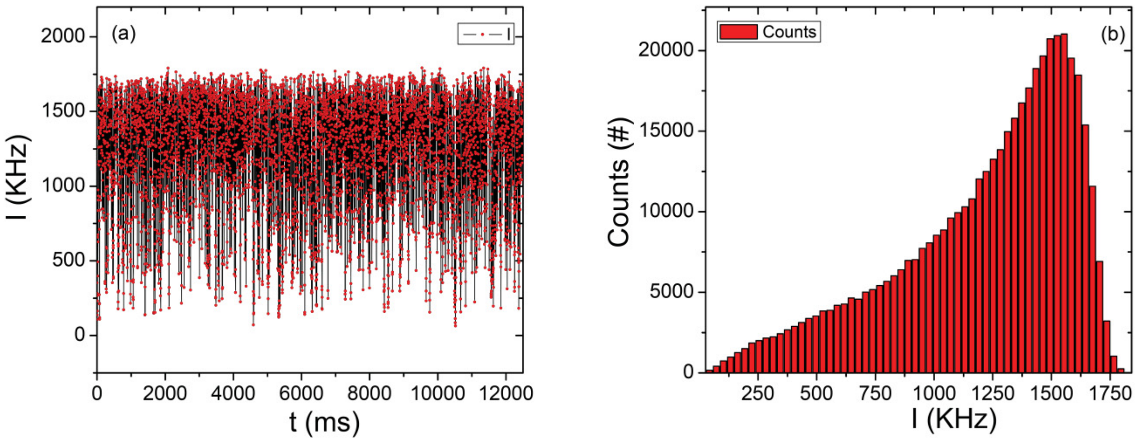

Figure 2-5 Intensity trace over time (a) and related histogram (b) of intensities of a 3 micron particle in diameter at the nominal tweezers laser power of 0.04W.

Usually, for a micrometric bead, a total of 500'000 intensities are recorded with a time lapse of 2ms. The histogram of intensities for large enough bin number and small enough bin size, can be taken as a good approximation of the probability density distribution of intensities the particle is scattering, while sampling all the accessible heights. From the latter it follows:

(2.13) $$\frac{N(I_s(h))}{\sum N(I_s(h))} \approx p\big(I_s(h)\big)$$

where, $N(I_s(h))$ is the number of counts and $I_s(h)$ the related scattered intensity at a given h. Further we assume that the probability to observe a scattered intensity is equal to the probability of finding the particle at the corresponding separation distance:

$$p(h)dh = p\big(I_s(h)\big)dI_s(h) \tag{2.14}$$

where $p(h)$ is the probability density distribution of heights sampled by the scattering object, $p\big(I_s(h)\big)$ the related probability density of the scattered intensities. Combining Eq. (2.13) with Eq. (2.14) we can relate the probability density of heights to the scattered intensity:

$$\begin{aligned} p(h) &= p\big(I_S(h)\big)\frac{dI_S(h)}{dh} = -p\big(I_S(h)\big)\beta I_S(h) \\ &\approx -\frac{N\big(I_s(h)\big)}{\sum N\big(I_s(h)\big)}\beta I_S(h), \end{aligned} \tag{2.15}$$

which in principle allows for measuring $p(h)$, because all terms on the r. h. s. are known or can be measured. This last relation is the most important assumption in order to further calculate interaction potentials. Since the system is in thermal equilibrium, the probability density of finding a particle at separation h, is related by Boltzmann's law to the difference in potential energy, $\Delta\Phi(h)$, of the particle at this position with respect to the position where the particle has the maximum probability density $p(h_\mathrm{m})$:

$$p(h) = p(h_m)\exp\left\{-\frac{\Delta\Phi(h)}{k_BT}\right\}. \tag{2.16}$$

Since Eq. (2.13) holds for all separation distances, including h_m, we may combine Eq. (2.14) to Eq. (2.16) to obtain a relation between observable quantities and the interaction potential we are looking for:

$$\frac{\Delta\Phi_{sw}(h)}{k_BT} = ln\left(\frac{p(h_m)}{p(h)}\right) \approx \ln\left(\frac{N(I_s(h_m))I_s(h_m)}{N\big(I_s(h)\big)I_s(h)}\right) \tag{2.17}$$

where $\Delta\Phi_{sw}(h)$ is the variation of the particle-wall interaction potential between h and h_m, the height related to the intensity with maximum counts. To display interaction potentials on an absolute scale, one needs to place the condition $\Phi_{sw}(h_m) = 0$ so to find the rescaling factor for which $\Delta\Phi_{sw}(h) \equiv \Phi_{sw}(h)$.

The graph below (Fig. (2-6)) is an example of an interaction potential measured on a 3 μm in diameter bead and at the nominal tweezers laser power of 0.03W.

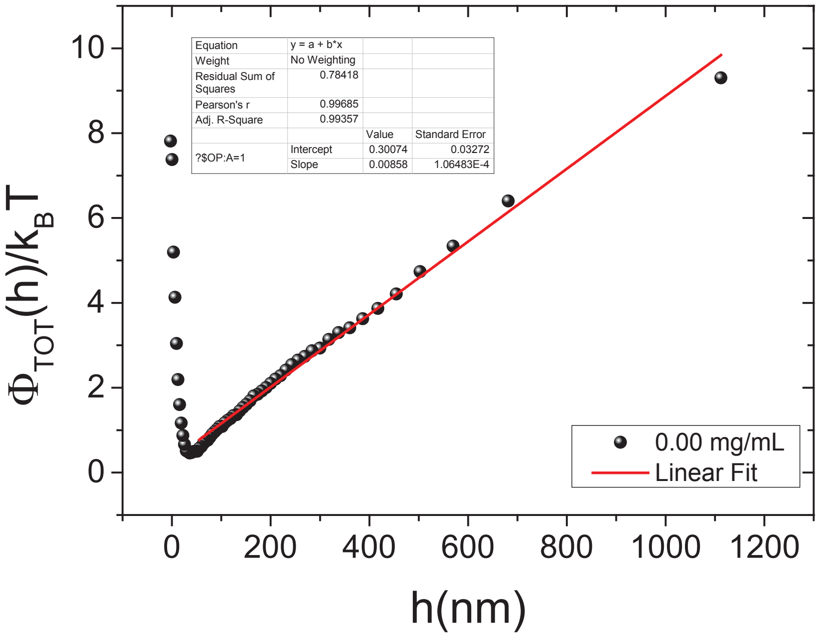

Equation	y = a + b*x		
Weight	No Weighting		
Residual Sum of Squares	0.78418		
Pearson's r	0.99685		
Adj. R-Square	0.99357		
		Value	Standard Error
?$OP:A=1	Intercept	0.30074	0.03272
	Slope	0.00858	1.06483E-4

Figure 2-6 Example of an interaction potential of a 3 μm in diameter colloidal probe sphere measured at the nominal tweezers laser power of 0.03W, in a HCl-Tris water suspension with a Tris concentration of 2mM and at constant pH=8.2 fully referenced on both axes using Eq.(2.11) and Eq.(2.17) (symbols) together with the linear fit performed over the gravitational branch for calibration (red-line).

As pointed out in Section (1.2.1) *'Gravitation and Light Forces'*, the gravitational contribution is a sum of the particles weigh force, F_G, and the radiation pressure, F_L, meaning that the value of its slope (red line in Fig. (2-6)) is directly proportional to the specific tweezers laser power and particle used for the measurement. Given that the weigh force related to the particle's mass stays constant, a calibration process is instead needed to measure the effective weigh force, $\tilde{F}_G$ related to the various tweezers laser powers, thus to the radiation pressure. To do so one simply needs to perform a series of measurements at all usable tweezers lasers powers and then plot the slopes resulting from linear fitting over each gravitational contribution (Fig. (2-7) red line) in function of the nominal tweezers laser power used, as shown in Figure (2-7) below:

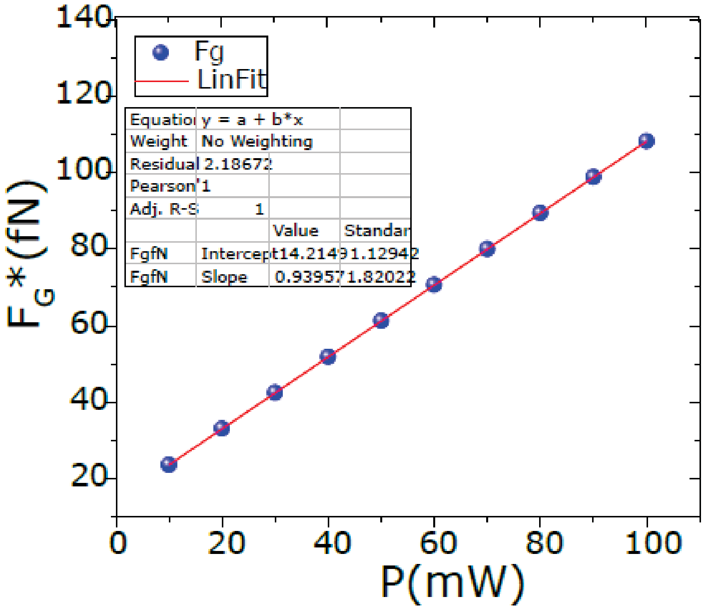

Figure 2-7 Linear fit (red line) over the slopes (symbols) of the gravitational branch of interaction potentials measured over a 4 μm bead in diameter in a HCl-Tris in water suspension at fixed pH=8.2 and varying the nominal tweezers laser power between 0.01W and 0.1W in steps of 0.01W.

The last step of the calculation is to perform another linear fit which intercept and slope are needed to extrapolate effective weigh forces at any given tweezers lasers power along the chosen interval of powers like follows:

$$\tilde{F}_G(P) = F_G^* = slope * P + intercept$$

where P is the nominal tweezers laser power used during the measurement and $\tilde{F}_G(P)$ the effective weigh force in function of given tweezers laser power extrapolated from the linear fitting operation. Moreover an estimate of the effective weigh force, $\tilde{F}_G$, comes necessary in providing an alternative estimate of the equilibrium separation distance, h_{min}. Given a heavy colloid dispersed in a depletant-free medium and diffusing very close to an interface but far enough to neglect Van der Waals attraction, the model describing its interaction potential with the surface underneath is a sum of two terms:

$$\frac{\phi_{TOT}(h)}{\kappa_B T} = Bexp\{-\kappa_D \cdot h\} + \tilde{F}_G \cdot h$$

in the order electrostatic repulsion and gravitational contribution, according to Eqs. (1.35) and (1.44). The equation to find the equilibrium distance given by the condition for a local minimum in the potential profile:

$$\frac{d\phi_{TOT}(h_{min})/\kappa_B T}{dh} = 0 = -\kappa_D B exp\{-\kappa h_{min}\} + \tilde{F}_G$$

which finally gives:

$$h_{min} = \frac{1}{\kappa} ln\left(\frac{B\kappa}{\tilde{F}_G}\right). \tag{2.18}$$

2.1.1.1 Measurement Errors

At this point, a topic that cannot be dismissed is the inevitable uncertainty that comes across measurements over real systems or the measurement errors. To reach a fair evaluation of those, one could start noticing that both, interaction potentials and separation distances, are defined as functions of the particle scattered intensities. The error in the determination of an interaction potential value at a given elevation and the error on the elevation distance it-self will therefore depend on the quality of the acquisitions. The sensitivity of the detector, but also the further data manipulation bring a contribution to the total error that can be evaluated. In the data processing, each intensity trace over time becomes a histogram of counts of intensities with finite bin width, thus limited precision. On top of those one needs to consider the errors coming from un-controllable sources. An example of the latter can be differences in the scattering properties between two nominally identical beads, or in the background noise of two nominally identical samples, or the systematic error. It is clear that a thorough mathematical determination of the Gaussian propagation of such complex experimental error is extremely cumbersome and finally will never account for all the actual causes. A more direct and less disputable way to determine the measurements errors is from a statistical treatment of the latter. For example, measuring a number of times over the same probe sphere and then evaluating the related interaction potentials will show directly how the error on the interaction potential values is depending on elevation distance, as shown in Figure (2-8) below.

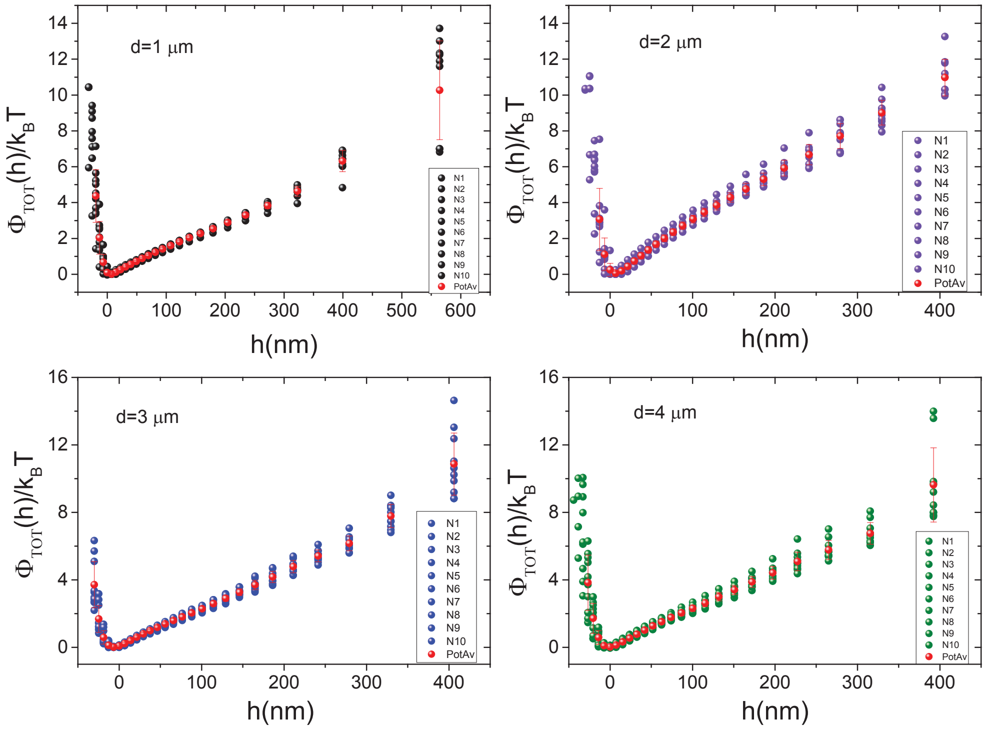

Figure 2-8 displays a collection of non-referenced interaction potentials measured over four differently sized probes, respectively (a) d=1μm, (b) d=2μm, (c) d=3μm, (d) d=4μm, at the nominal tweezers laser power of 0.05W each in the proper dispersing medium. For each probe measurements were repeated ten times (dots of the same colour and without error bar in each graph). From those ten measurements an average interaction potential is calculated point by point with related error bars to each point (red dots with error bars in each graph).

For a mathematical determination all is needed is to apply statistics to the evaluated interaction potentials in order to determine the average interaction potential and the standard deviation from the average interaction potential, point by point. Therefore:

$$\phi_{ave}(h) = \frac{1}{N}\sum_{i=1}^{N=10} \phi_i(h)$$

$$\sigma(h) = \sum_{i=1}^{N=10} \sqrt{\frac{\left(\phi_i(h) - \phi_{ave}(h)\right)^2}{N}},$$

where $\phi_{ave}(h)$ is the average interaction potential at each sampled elevation distance, h; $\phi_i(h)$ is the interaction potential at each sampled elevation distance measured at measure i, N is the total number of measurements and the standard deviation $\sigma(h)$ is finally the error bar for each average interaction potential value at each sampled separation distance. By looking at the trends of the $\sigma(h)$ for the four differently sized spheres, one common feature strikes the eye as the error related to each height is in general non equally weighed but increases with the elevation distance, as shown in the graph below:

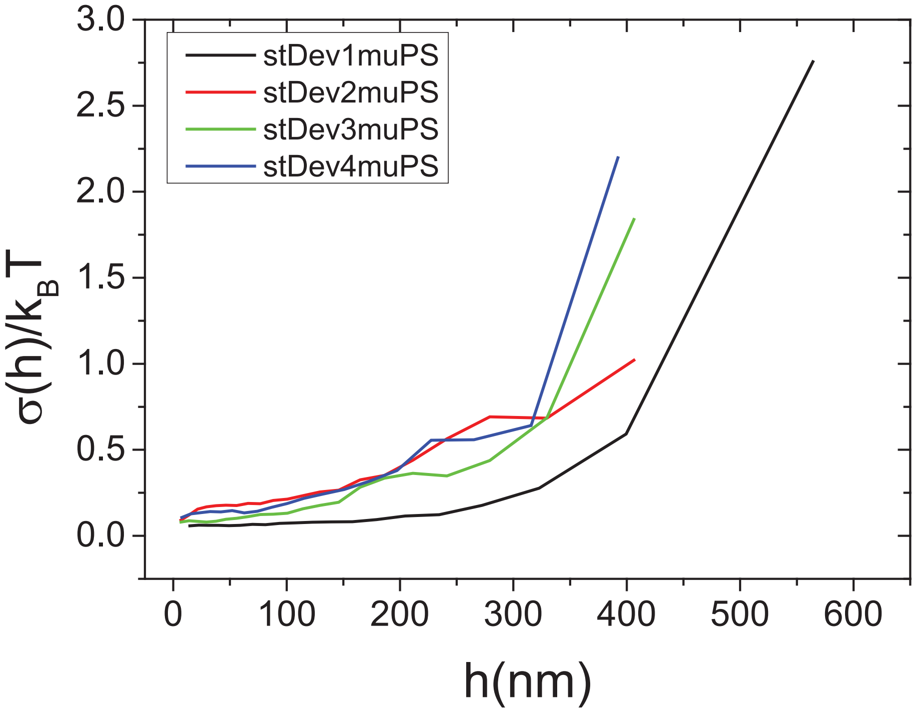

Figure 2-9 trends of the standard deviations related to evaluated average interaction potentials in function of sampled heights for 1,2,3 and 4μm in diameter probes.

At a closer look this property comes not unexpected. The heights related to intensities with higher counts display a smaller error as compared to higher elevations where statistics are poorer. This directly derives from the uneven illumination provided by the evanescent wave scattering source where objects closer to the interface scatter a stronger signal then objects further away from it. In other words, the more reliable points of a measurement are those related to the maximum of the intensities distribution function therefore to the minimum of the interaction potential. To have a feeling of the uncertainty related to the systematic error that comes along with the acquisitions, a number of independent measurements, all at same conditions but substituting the probe sphere with a nominally identical one (say another particle form the same batch), have been performed. From those by using the same statistical formulas above an average set of elevation distances and related standard deviations have being calculated. The graph below (Fig. (2-10)) shows the three independently measured interaction potentials with the error bars along the h-axes:

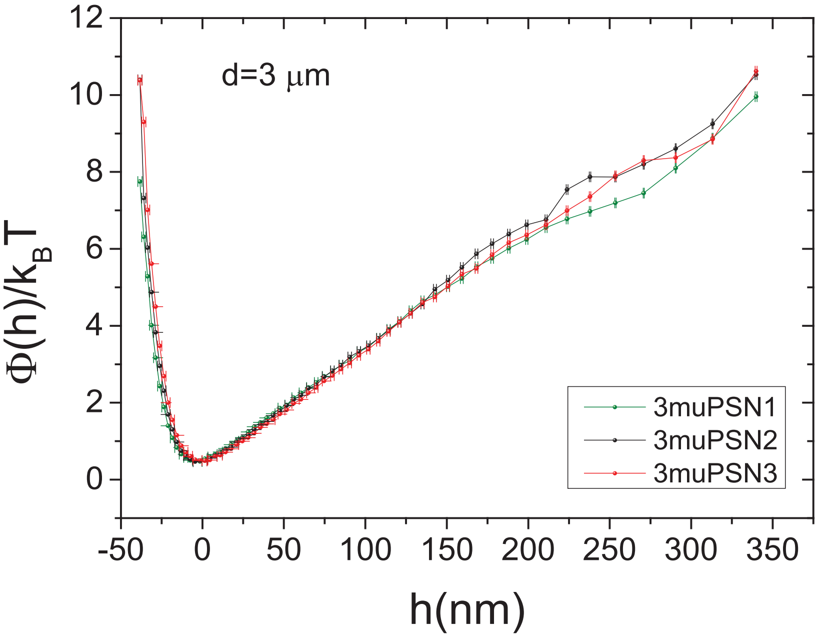

Figure 2-10 Non-referenced interaction potentials from three nominally identical 3μm in diameter beads all measured at nominal tweezers laser power of 0.03W and in the same dispersing medium. The bars across the experimental points indicate the calculated standard deviation for each height respect to the average one over the three measurements.

Given the low number of total measurements considered, it can be firmly concluded that the error in the determination of the elevations is negligible while the one over the interaction potential values at each height grows larger where the probability for the particle to be found is the lowest. Keeping this is mind, in the following interaction potentials will be displayed without error bars for sake of clarity.

3 Materials and Methods

3.1 Samples and Samples Preparation

Introduction

In this chapter, materials, techniques and protocols used for the samples preparation are described in detail. The first paragraph describes the samples prepared to study protein-protein non-specific interactions (3.1.1 *Protein-Protein Non-specific Interactions Samples Preparation*); the second paragraph is about the samples preparation related to the study of depletion interactions (3.1.2 *Depletion Interaction Samples Preparation*).

Protein-Protein Non-specific Interactions Samples Preparation

To obtain colloidal particles coated with a 2D protein layer, polystyrene beads from ThermoSCIENTIFIC of 4 μm in diameter were chosen as colloids and fluorescent S-layer fusion proteins, called SgsE-EGFP S-layer proteins, were used as coating material and were provided by the group of Nano-bio-technologies of the BOKU University in Vienna. To obtain the coating suspension, 5mg of lyophilized proteins was dispersed in 2mL of 6M Urea with 50mM HCl-TRIS solution at $pH \approx 7.5$ for a total protein concentration $c_p = 2.5$mg/mL. Urea is needed to denaturize the proteins so to have them as monomeric dispersion. The suspension was then directly filtered through 0.45 μm PTFE filters into dialysis tubes (from Biomol) with a nominal cut off molar mass of 16 KDa and then dialyzed two times against 1L of –deionized Water from a Millipore-MilliQ water purification system for 30 min each time. The solution obtained this way, was then spun down at 10.000 rpm for 5 minutes to make any unwanted residue or dirt sediment, while keeping the clean proteins in the supernatant. The supernatant protein concentration was measured spectroscopically (Nano-Drop 2000c from Thermo-SCIENTIFIC) to dilute the suspension up to $c_p = 0.4$ mg/mL. All steps were performed keeping the solutions in a dark environment to minimize the bleaching of the EGFP. To obtain S-layer coated particles, a suspension of 4 μm polystyrene beads from Thermo-Scientific with a colloid concentration of 13 mg/mL was used and mixed with the coating suspension in equal parts. The mixture was then kept on a shaker at 4°C for 4 hours. To wash away the potential excess of coating material, the particles were spun down three times fort two minutes with a Minispin micro-centrifuge Z606235 from Sigma Aldrich at the maximum speed of 13400 rpm and re-dispersed in fresh MilliQ-water.

After testing that the 13400 rpm of the micro-centrifuge were not enough to sediment proteins, the maximum speed was safely used to speed up the particles sedimentation process. Finally, as last step, the sediment was re-dispersed in the appropriate buffer for the TIRM measurements. The same procedure was used to coat the flow-through cells, where potential excess coating material was removed by thorough rinsing with MilliQ-water. To check the effectivity of the coating procedure on the particles, we exploited the fluorescent nature of the EGFP s-layer proteins. It is known that the green fluorescent protein emits green fluorescence when exited with light in the blue to ultra-violet range [78, 79] and that after excitation the only luminous signal will come from the fluorescent proteins. Thus a coated sample of 4 micron diameter beads was analysed with confocal fluorescent microscopy and a picture of it is reported below in Fig. (3-1)(a). In the latter, the beads are the only source of light in the sample meaning that the coating procedure was successful as well as the rinsing off of the exceeding coating, which would have prevailed on the background otherwise. The other two pictures, in alphabetic order, show respectively: a schematic representation of the S-layer fusion protein where the grey area marks one unit cell composed of two monomeric proteins in a p2 lattice symmetry [28] (Fig. (3-1)(b)) and a TEM picture of the 4 micron beads in diameter to be coated (Fig. (3-1)(c)).

Measurements were performed in HCl-Tris suspensions at fixed $pH \approx 9$ varying the effective ionic strength between 2mM and 40mM. The effective salt-buffer concentration was obtained using the following formula:

$$\frac{[A^0]}{1 + 10^{pk_a - pH}} = [A^-], \tag{3.1}$$

where $[A^0]$ is the molar concentration of the non-dissociated buffer, $[A^-]$ is the concentration of dissociated acid groups resulting at a given pH and pk_a which is the negative logarithm of the dissociation constant of the salt in water.

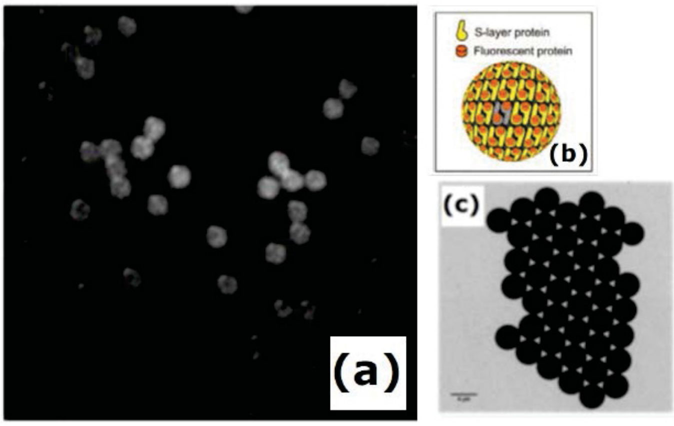

Figure 3-1. (a) confocal microscopy image of 4 µm polystyrene particles coated with SgsE-EGFP; (b) artistic view of a particle coated with an s-layer 2D lattice with P2 symmetry [28] and (c) TEM image of 4 µm polystyrene particles.

Depletion Interaction Samples Preparation

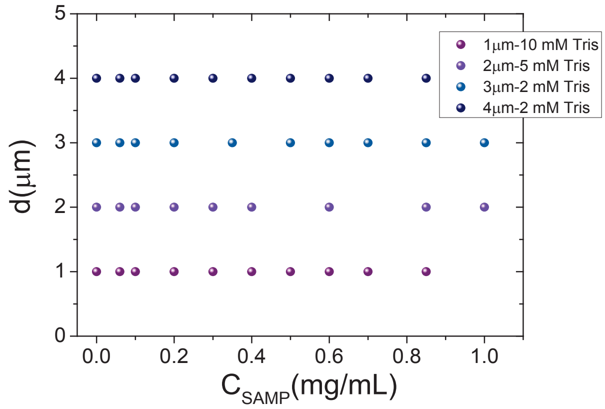

Figure 3-2. Each dot represents a sample with specific fd-virus concentrations c_{SAMP}, prepared to investigate depletion interactions between four differently sized probe spheres and a wall. The salt concentration of the buffer is colour codes as indicated in the legend.

The graph in Figure (3-2) above summarizes the compositions of all the samples prepared for the investigation of depletion interactions between a spherical colloidal probe and a planar wall induced by rod-like depletants. As spherical probes the same differently sized polystyrene particles purchased to perform the protein coating (see section 3.1.1) were used. As rod-like depletants we used wild-type fd-virus, considered a model system for anisotropic colloids like slender objects [49]. The latter were grown and harvested in-house following procedures carefully reported elsewhere in literature [21] and then stored in a HCl-Tris buffer suspension at constant $pH = 7.5$. The polystyrene particles were provided in a very concentrated stock solution so, before use, those were washed in pure water at least two times, using a regular spin-down and solvent exchange procedure, and then diluted till obtaining a very clear suspension. The fd-viruses stock solution was instead diluted into other three stock solutions of $1\,\frac{mg}{mL}$ in concentration, using HCl-Tris buffer suspensions at three different Tris-salt concentrations of $2-5-10\;mM$, at constant $pH = 8.2$ and with 15% volume of Ethanol added to prevent bacterial growth over time. The Tris-buffer concentrations were chosen after an empirical evaluation of the partial screening of the electrostatic repulsion between the probe spheres and the glass surface due to the constant partial dissociation of the buffer in solution. The latter had to be such that the probes will reach close enough to the interface to scatter enough light from the evanescent wave without being caught in the Van der Waal attraction range. Finally Tris-solutions were matched as follows:

- $10\;mM \rightarrow 1\;\mu m$
- $5\;mM \rightarrow 2\;\mu m$
- $2\;mM \rightarrow 3-4\;\mu m$

where the last case reports as well the minimum concentration possible to use for the Tris-buffer to actually keep the pH steady. To be fair it takes to point out that the values listed above refer to the Tris-buffer concentrations used for the preparation of the solutions but the respective effective ionic strength related to the given $pH = 8.2$ was calculated, via the already used Eq. (3.1), to be exactly half of the total concentration, thus:

$$I_{eff}^{Tris} = \{1-2.5-5\}\;mM.$$

The three fd-virus stock solutions were then diluted down to the desired concentrations targeted during the experiment and well summarized in Figure (3-2) for each probe size. The effective fd-concentration of each dilution prepared was checked via UV-Vis spectroscopy and found between the following listed values:

$$c_{samp} = \{0.00-0.06-0.10-0.20-0.30-0.35-0.40-0.50-0.60-0.70-0.85 \\ -1.00\,\}\frac{mg}{mL}.$$

An important reference value for the system fd is the so called overlap concentration, or c^*. The latter defines the concentration at which the fd-viruses stop behaving as a gas and start to overlap thus to interact with each other. Such value is calculated through its inverse proportion to the volume of a sphere having half of an fd-virus length as a radius:

$$c^* \propto \frac{1}{V_{sphere}^{fd}} = \frac{6M_{rod}}{\pi N_A L^3} \approx 0.07\ \frac{mg}{mL}.$$

The overlap concentration represents the upper limit for the low density approximation to be fulfilled. It it worth to notice that just the first two concentrations reported for the fd-virus dilutions are within this limit, all the rest belongs to the high concentrations limit up to $14 \times c^*$, or $1\frac{mg}{mL}$, which is the highest concentration considered. To have the measurements performed at the best over a single particle in the measuring volume, the preparation of the binary mixtures used to investigate depletion interactions was realized directly in situ using the flow-through cell. The particles dispersion was flushed-in the flow-through cell then, after a suitable particle was trapped at high tweezers laser power, the excess was rinsed out with at least 250 mL of pure water. Only at last the pure water was substituted by flushing in 5 mL of the wanted HCl-Tris buffer solution at the desired fd-virus concentration to perform the measurements. Given the volume of the flow through cell being 540 μL, the latter quantity is enough to ensure a full exchange of solvent.

4 Results from Statics and Dynamics

Introduction

In this chapter the data analysis and the results obtained are explained in detail and organized in two main paragraphs, respectively *Results from Static Data Analysis* (4.1) and *Results from Dynamic Data Analysis* (4.2).

4.1 Results from Static Data Analysis

4.1.1 Results from S-layer coated colloids

The study of protein-protein non-specific interactions was inspired by an experimental investigation from Valle-Delgado et al. where their aim was to monitor the effects of the dispersing medium conditions on the interactions between surfaces coated with bovine serum albumin (BSA) [36, 80]. Finally their scope was to address protein stability at physiological pH and salt concentrations and eventually above such limits.

Proteins are well known biological macro-molecules capable of performing a wide variety of functions basic to life, from DNA replication [81], response to stimuli [82], and transport of other molecules from and to specific locations [83], to catalysing the metabolic reactions [84]. Thus a great diversity in structures and interactions is required for such class of molecules to fulfil their purpose. Such diversity is granted by the unique sequence of amino acids and residues building up the specific protein, which do not account solely for its chemical composition but also for its folded structure and therefore its activity [85, 86]. Due to their intrinsically complex chemical composition, proteins show anisotropically patterned surface charges and given their typical size range they are normally treated as colloids. This is why this class of macro-molecules is also described as patchy colloidal system [87]. As with colloids, one may think that also here pair-wise interactions can be well described by a DLVO potential. The trends described by the blue curves in Figure (4-1) are the total pair-wise DLVO interaction potential, resulting from the sum of electrostatic repulsion (Fig. (4-1)-black lines) and Van der Waals attraction (Fig. (4-1)-red lines), and calculated with parameters typical for Apoferritin, a very common protein found in almost all living organisms that commonly acts to store iron and release it in a controlled manner [88]. The two graphs below show total pair-wise interaction potentials calculated taking the protein as a patchy colloidal sphere with total number of surface charges $Z = 50$ and radius $R = 6.9\ nm$ [35]

in a solution of deionized water, $c_{salt} = 10^{-5} mM$ (Fig. (4-1)(a)), and at physiological salt concentrations, $c_{salt} = 152\ mM$, both at constant $pH = 7.5$ (Fig. (4-1)(b)).

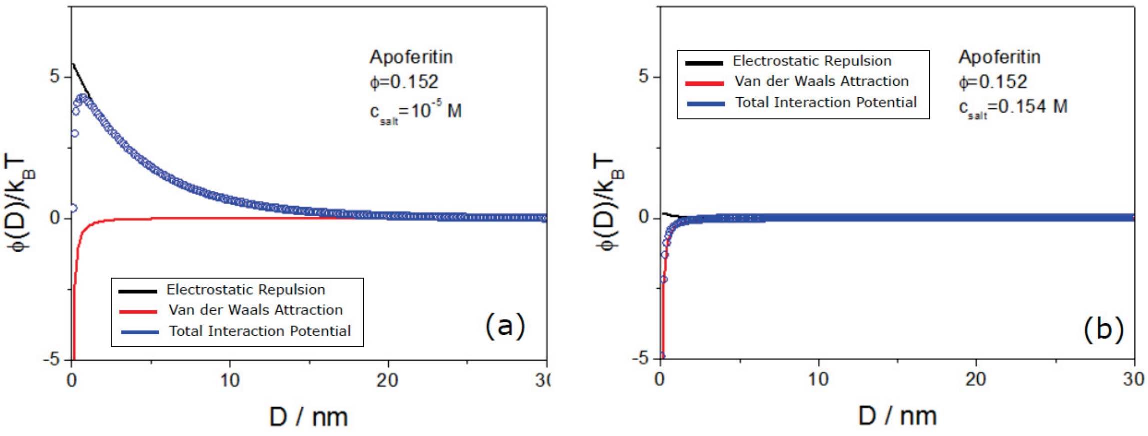

Figure 4-1 Plots representing the pair-wise interaction potential between two proteins calculated with average values of the surface number of charges, Z=50, and radius, R=6.9 nm, typical for Apoferritin and considering a Hamaker-constant of $1k_BT$*. Figure (a) displays in blue the total interaction potential in pure water; figure (b) shows the same case but with increased salt concentration matching physiological conditions, i.e.* $c_{salt} = 152mM$*.*

In the first case, the blue curve in Figure (4-1)(a) describes a system stabilised at short distances by an energetic barrier that prevents the components from aggregation. In Figure (4-1)(b) instead, where the salt content is dramatically increased, the total interaction potential becomes purely attractive, due to the salt screening effect on the surface charges, causing aggregation. Though, the fact that life is possible, if not necessarily, happening in such ranges of pH and salt concentrations, leads to the obvious conclusion that there must be an additional kind of interaction beyond the DLVO potential stabilizing proteins against aggregation. The latter is generally attributed to Hydration forces [34]. In their experiment Valle-Delgado et al. studied their protein system via Atomic Force Microscopy (AFM) and reached the conclusion that indeed there is an hydration layer stabilizing the system at distances below 2 nm and at salt concentrations as high as 1M and pH~9 [80]. Given the higher resolution in force measurements of TIRM with respect to AFM, we attempted a similar investigation but on a different kind of protein, called S-layer proteins. The basic motivation was to study whether such stabilizing forces at high salt concentration are indeed a common feature of protein systems, especially within the range of the Van der Waals interactions.

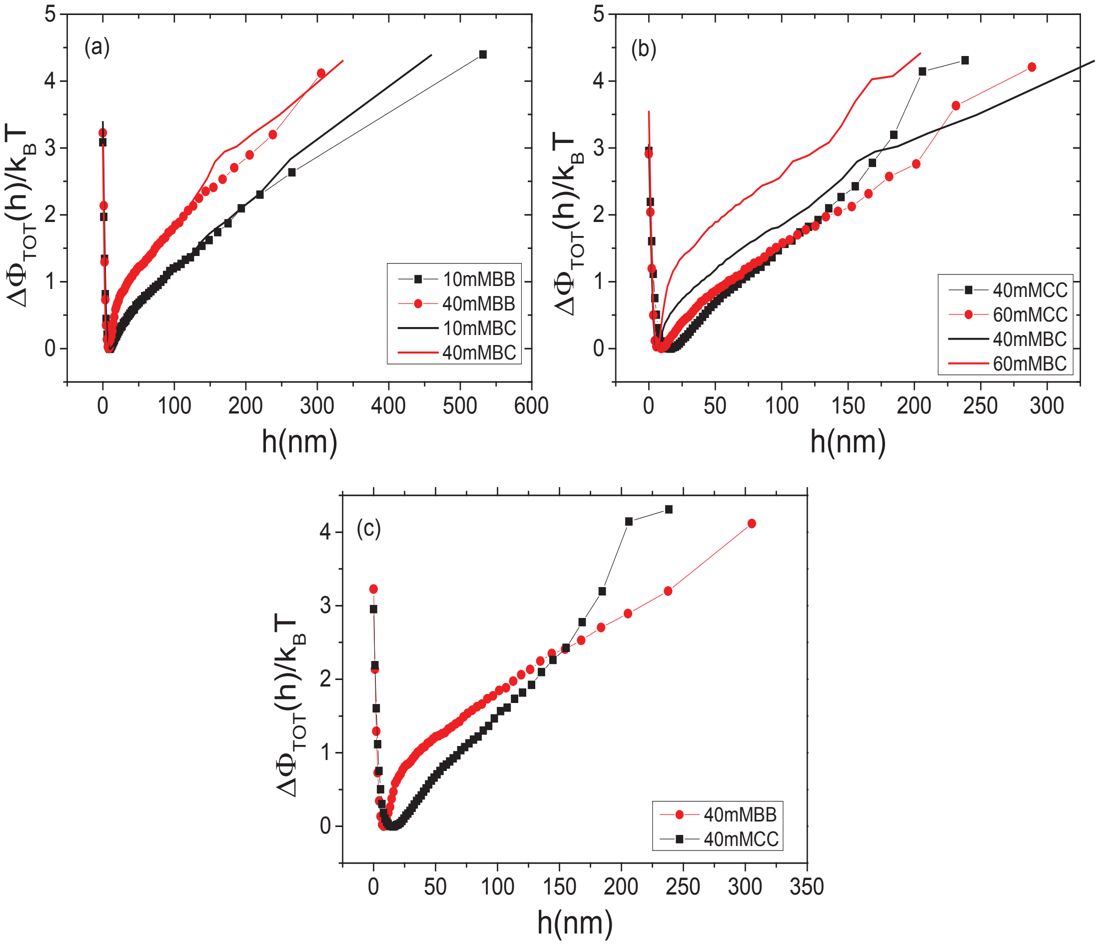

Figure 4-2 *Comparison of relative particle-wall interaction potentials measured over coated and un-coated 3 micron bead, at various ionic strengths* $c_{\mathrm{TRIS}} = 10 \div 60\ \mathrm{mM}$ *and at constant tweezers lasers power of 0.03W and pH=9. Panel (a) shows the interactions measured between a bare particle and a bare wall (BB, symbols) and bare particle and coated wall (BC, lines) at salt concentrations* c_{TRIS}*=10, 40mM; panel (b) shows the interactions between a bare particle and coated wall (BC, lines) and between a coated particle and coated wall (CC, symbols) at salt concentrations* c_{TRIS}*=40, 60mM; panel (c) shows the interaction potentials measured at same the salt concentration,* c_{TIRS}*=40 mM, for a bare particle over bare wall (red symbols) and for coated particle over coated wall (black line plus symbols).*

The graphs in Figure (4-2) above, show interaction potentials measured at buffer concentrations $c_{TRIS} = 10, 40, 60\ mM$ and constant pH $= 9$. The potentials are represented in the form of $\Delta\Phi = \Phi - \Phi_0$, meaning that the minimum value of the potential is set to zero ambiguously. It was not possible to fit the experimental data with the model function including hydration effects as proposed in the theory, therefore the discussion has to be limited to a qualitative comparison of the measured interaction potentials.

The measurements were taken under the following conditions: a bare particle interacting with a non-coated wall (Fig. (4-2)(a)-symbols); a bare particle interacting with a coated wall (Fig. (4-2)(a)-lines) and finally a coated particle interacting with a coated wall (Fig. (4-2)(b)-symbols). The potential profile between a bare sphere and the bare wall (BB) shows a distinct increase of the slope at separation distances slightly above the equilibrium position, while at larger separation distances the slope decreases to the particles weigh force. A qualitatively similar trend is observed for the case of a bare particle interacting with a protein coated wall (BC). The deepening of the potential well is a clear indication for Van der Waals interactions not being fully over-compensated by the electrostatic repulsion between particles and walls. When the interface and the particle are both coated instead (CC) (Fig. (4-2)(b)-symbols), the profile minima are much shallower, indicating an almost complete outweighing of the attractive term in the total interaction potential. The observation gets even more supported by a closer look to Figure (4-2)(b), especially comparing the trends described by lines and by symbols respectively. The interaction potentials drawn as lines are related to the case of a bare particle interacting with a coated wall (BC), the symbols instead picture the case of a coated particle interacting with a coated wall (CC). The latter show a much shallower attractive minimum.

In all cases shown in Figure (4-2) the salt concentration in the buffer is high enough to effectively screen electrostatic repulsion. Therefore, the contribution of Van der Waals attraction to the potential profiles can be clearly observed in the cases where the bare probe particles interact with the bare or the coated wall. However, if the particles and the wall are coated with S-layer protein, Van der Waals attraction can be effectively over-compensated. Even at a buffer concentration of $c_{TRIS}=60\ mM$ there is only a small reminiscence. Here it is important to note that at electrolyte concentrations $c_{TRIS}>40$ mM the bare particles will inevitably sediment to the bare glass surface and stick there irreversibly due to Van der Waals attraction. There are two potential explanations for this observation. (I) Either the charge density on particles and walls increases drastically by the coating by that increasing the amplitude of the electrostatic repulsion, or (II) there is an additional contribution to the interaction potential introduced by the coating.

The first hypothesis can be checked by comparing potentials measured between a bare sphere and a bare wall to a potential measured between a bare sphere and a coated wall. If the coating would change the charge density significantly, a change of the profile shape should be observed even if only one of the interacting partners is changed. To the contrary, it is evident from the profiles shown in Figure (4-2)(a), that potentials are virtually indistinguishable independently of whether the glass surface is protein coated or not.

However, this argument is based on the assumption that the coating of the glass surface was successful, which we could regrettably not prove experimentally. Therefore another method needs to be applied to check hypothesis (I), which is based on model calculations of the potential profile. In Figure (4-3) model curves which represent a superposition of electrostatic repulsions, Van der Waals attraction and a gravitational contribution are plotted, according to Eq. (1.54) and in units of $k_B T$. The profiles were calculated, choosing parameters such that shapes were obtained which are qualitatively similar to the profiles displayed in Figure (4-2), e.g. sphere radius R=2000 nm, effective weight force $\tilde{F}_G = 40\text{fN}$, Hamaker constant A_{H}=0.1$k_{\mathrm{B}}T$, Debye screening length $\kappa_D^{-1} = 2$ nm and amplitudes of the electrostatic repulsion, B, varying from $10^3 k_B T$ to $10^6 k_B T$.

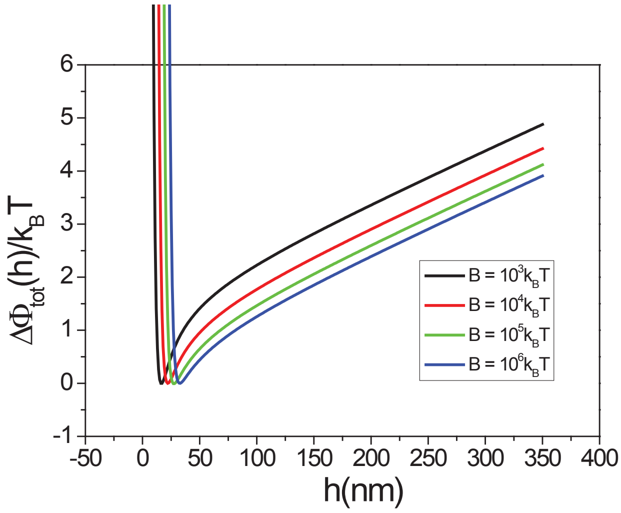

Figure 4-3 Calculated potential profiles between a sphere and a wall. The curves represent a superposition of an electrostatic repulsion, a Van der Waals and a gravitational contribution, calculated in the Derjaguin-limit with the parameters: sphere radius $R = 2000$ nm, effective weigh force $\tilde{F}_G = 40$fN, Hamaker-constant $A_H = 0.1\ k_B T$, Debye screening length $\kappa_D^{-1} = 2$ nm and amplitudes, B, of the electrostatic repulsion varying as indicated in the legend.

The calculated curves imply that to cause the experimentally observed change in profile shape one would needed an electrostatic amplitude as bigger as thousand times the original one. Further on, this increase should depend solely on the protein coating, meaning that the effective charge density would have to increase by a factor thirty, given that the repulsive potential is approximately proportional to the square of the charge density. Thus, although we do not have sound experimental proof to rule out this option definitely, such increase in number of charges would be rather impressive. It is therefore likely that we are observing the effect of an additional repulsive interaction on top of the DLVO potential. However, this interaction appears to be effective over a range of tens of nano-meters, thus it cannot be due to hydration forces as suggested earlier, because they have a typical range of about two nano-meters. Regrettably a quantitative analysis was not possible due to difficulties encountered in properly fitting the data. It was shown earlier, that describing Van der Waals potentials quantitatively is difficult [12] but, in our case, a further problem aroused from the unknown interaction term due to the protein coating for which the hydration force model was found inconsistent. Finally we observed a generally poor reproducibility of the measured profiles, as often happens with biological material and high salt concentrations, which is probably due to inhomogeneity of the coating. For these reasons these results, though very intriguing, shall be considered preliminary.

4.1.2 Depletion interactions mediated by fd-virus: on the limits of low density and Derjaguin Approximation

Depletion interactions are a basic energetic contribution when it comes to the stability of binary or even more complex colloidal mixtures. Asakura and Oosawa described the phenomenon in terms of a pair-wise potential using a simple entropic picture and imposing two important limitations for the validity of the theory: *Derjaguin approximation* and *low density approximation*. The first approximation is needed as a practical tool to calculate the force between curved surfaces which can be described trough the potential between flat walls provided that the range of the interaction is short enough, the second approximation simply neglects the mutual interaction between depletant particles. Experimentally, much work was dedicated to the measurement of depletion induced by polymer coils [15, 16, 54, 55] or anisotropic rod-like depletant [53, 89] to confirm the theory.

The first experimental investigation of depletion interactions induced by fd-virus is from Yodh et al. [60] where they investigated depletion interactions between two spheres induced by rod-like depletant at high concentrations, as high as $14 \times c^* \cong 1\ mg/mL$, being $c^* = 0.07\ mg/mL$ the overlap concentrations for the fd-system. Theoretically, the problem of highly concentrated suspensions of rod-like depletants was addressed already many years before. Independently of each other, Auvray [57] and Mao et al. [58], devised an approach to describe the influence of the mutual excluded volume of rod-like depletant at high concentrations up to 10 times the overlap concentration. By means of a third order expansion in density, depletion forces were calculated with a formulation where the effective diameter of the rods in function of pH and salt concentration is also used. They predicted a 6% decrease of the depletion forces at rod concentrations as high as ten times their overlap density.

The effect of the spheres to depletant size ratio was studied by Yaman et al. [56] in the frame work of the lack of phase separation in mixtures of spheres and rods while later on Lang [59], by means of numerical calculations, explored the role of depletant polydispersity on depletion interactions at low density. Common finding in both the latter studies has been that at ratios of rod-length over sphere radius L/R=2, the predicted value for the depletion interaction contact potential calculated using Derjaguin approximation can get as large as three times higher than what evaluated from numerical approximations.

The present experimental investigation [18] is bridging the theoretical and experimental papers quoted so far, proposing measurements taken over four differently sized micrometric beads, in order to probe the validity of Derjaguin approximation, and fd-concentrations up to 14 times the overlap concentration, to purposefully violate the low-density approximation. For each probe measurements were taken over almost ten different fd-concentrations and for each concentration at eight different tweezers laser powers with the purpose of increasing statistics and prove reproducibility.

The experimental data were analysed using the following procedure which basically consist of non-linear least squares fitting of the potential profiles with the expression of Eq. (1.61). This model function, in essence contains only two adjustable parameters, i. e. the amplitude of the electrostatic repulsion, B, and $\Phi_{tot}(h_{min})$, which have to be determined to compare the potentials on an absolute scale. Further, the experimental potential profiles have a distance coordinate with the zero position at the position of the potential minimum. Therefore also the absolute separation distance, at which the probe sphere experiences the lowest potential, h_{min}, has to be determined. Finally, we also allowed the concentration of rods, c_{rod}, to float freely in a wide range of concentrations, to detect deviations from the low density approximation.

To achieve the highest reliability of the best fitting parameters, we adhered to the following protocol. Firstly, we calibrated the effective force, $\tilde{F}_G$, by simultaneous fitting on a series of data sets obtained in the absence in a depletant-free suspension at various powers of the laser tweezers. By this procedure, we obtained a linear relation between $\tilde{F}_G$ and the nominal laser power used for the measurements, to keep $\tilde{F}_G$ as a fixed parameter further on during the fitting operations on the data obtained in the presence of fd-virus. Secondly, we simultaneously fitted the sets of data which were obtained for a given virus concentration at different laser powers. In this case c_{rod} and B were used as global parameters, e.g. they were forced to be the same for all sets of data, while the local parameters h_{min} and $\Phi_{tot}(h_{min})$ were allowed to vary between the data sets. In a complementary step we performed simultaneous fits of the data sets obtained from samples with different fd-concentrations but at the same laser power. In this case, only $\tilde{F}_G$ was used as a global parameter, which was however fixed to the value obtained from the linear $\tilde{F}_G$ versus nominal power relation. To determine the values of h_{min}, we used the fact that the potential profiles have a local minimum determined by the other parameters via the relation:

$$\frac{1}{k_B T}\frac{d\phi_{TOT}(h_{min})}{dh} = 0 = -\kappa_D B exp\{-\kappa_D h_{min}\} + \tilde{F}_G + \frac{\pi c_{rod} N_A}{M_{rod}} L_{rod} R_{sphere}\left(1 - \frac{h_{min}}{L}\right)^2, \tag{4.1}$$

which was solved numerically during each iteration of the fitting procedure.

The knowledge of h_{min} and $\Phi_{tot}(h_{min})$ allows the comparison of potentials measured under different conditions on absolute scales of potentials and separation distances. The reference frame was set such that by definition the apparent gravitational contribution vanishes at particle wall contact, i. e. $\lim_{h\to 0} \tilde{F}_G h = 0$.

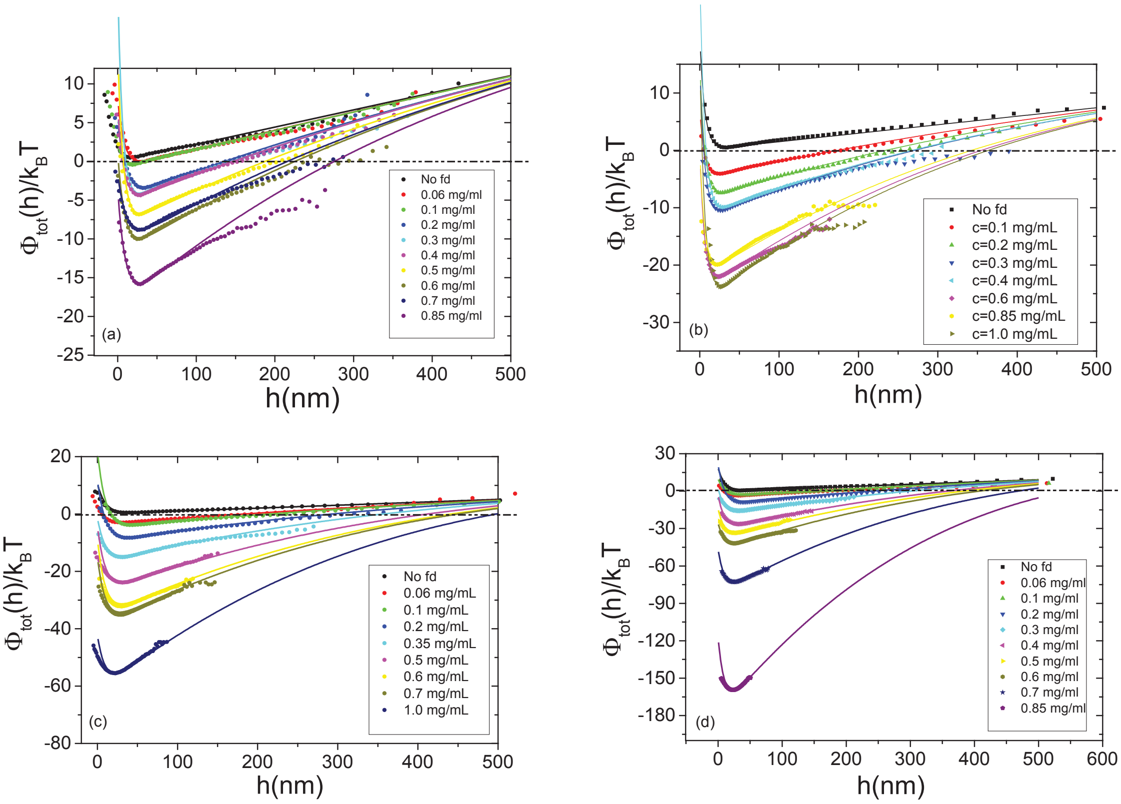

Figure 4-4 Measured interaction potentials (symbols) and theoretical calculations from the fitting parameters (lines) for d=1 μm (a), d=2 μm (b), d=3 μm (c) and d=4 μm (d) particles in diameter at a nominal laser power of 0.03W and at increasing fd-concentrations as indicated in the legend.

The graphs in Figure (4-4) represent measured and calculated interaction potentials between each probe sphere and the interface at the nominal laser power of 0.03W. In each of the graphs above the full symbols are the measured data where the full lines are calculated from using the resulting best parameters of the fitting operation performed on the same data set. In this representation, the trends are more easily visible, since negative potential values can be due to the depletion contribution only. The data depicted with full black symbols and full black lines are those measured in a depletant-free solution which is regarded as a reference. The data sets depicted with red full symbols define the measurement taken at fd-concentration below the overlap at the nominal fd-concentration of $0.06\frac{mg}{mL}$. The latter was chosen as the only concentration below the overlap one, $c^* = 0.07\ \frac{mg}{mL}$, as to set a reference before the violation of the ideal gas approximation.

Analysing the experimental data, we come to a first important conclusion: even for concentrations far above the threshold set by the overlap one, the model theory predicts some experimental trends correctly. All the parameters, which determine the shape of the potential profile including the depletion contribution, are known except for the amplitude of the electrostatic potential, B. Therefore it is possible by numerical calculations, using the model function (Eq. (1.56)) and its first derivative, Eq. (4.1), to identify trends about how the parameters h_{min}, $\Phi_{tot}(h_{min})$ and c_{FIT} depend on the concentration of the depletant. Here c_{FIT} is the rod content as determined from the fitting procedure as opposed to c_{SAMP} wich is the fd-concentration determined independently by UV-VIS spectroscopy. It is expected that h_{min}, $\Phi_{tot}(h_{min})$ decrease linearly with fd-concentration, while c_{FIT} should be equal to the pre-set virus concentration. Fortunately it turns out that variations of the unknown parameter, B, over one order of magnitude does not change any of these trends significantly. Therefore the electrostatic amplitude was set to the constant value $B = 20k_BT$ in all the calculations discussed below, which is a reasonable choice, since a value of this order was determined in all the fitting procedures. The following plots represent the trends of the equilibrium distances, h_{min}, as determined by the fitting operations for all data sets and for each probe size. The lines with symbols picture the data extracted from the fits on the experimental data, whereas the dashed-dotted lines describe the predictions of the same quantities as calculated from Eq. (1.56) using the best fitting parameters. The calculated lines show the same trend and same average slope as the experimental data and at a closer look, especially the data points corresponding to $c_{rod} = 0.00 mg/mL$, reveal a trend in tweezers laser power. The equilibrium distance gets indeed smaller and smaller as the laser power increases. Moreover, the effect seems to be more pronounced with increasing probe size, whereas for the smaller probe used the dispersion of the height at zero fd-concentration is much lower and scattered around a much lower average distance. This indicates that the particles with 1 μm diameter are feeling a stronger trapping power as compared to the other probes, confirming what was stated already in the theory about the optical traps in the Mie-Lorentz regime (Section (1.2.1)). This dispersion effect on the heights due to the optical pressure becomes though negligible in all the cases at non-zero fd-concentration meaning that the attractive minima induced by depletion were in any case predominant with respect to the extra push due to the optical pressure in the same direction.

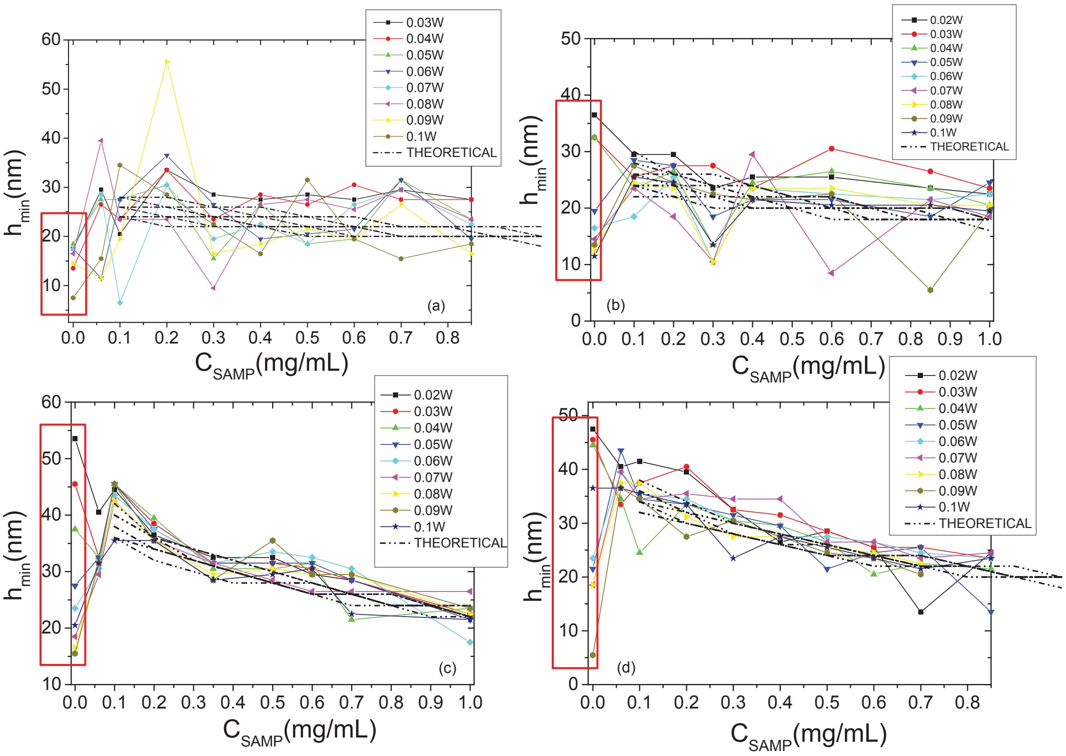

Figure 4-5 trends of the equilibrium positions (h_{min}) achieved from the fitting operations (lines plus symbols) for all the probes: d=1 μm (a), d=2 μm (b), d=3 μm (c), d=4 μm (d), in function of increasing fd-concentration. Different colours refer to various nominal tweezers laser powers as indicated in the legend. Dashed-dotted lines represent trends which were calculated as explained in the text; the red boxes highlight the distribution of the h_{min} values in fd-free suspensions due to the optical pressure.

This last observation is very important in order to validate the findings about depletion interactions, proving that the trapping is not influencing qualitatively the results. The graphs below instead picture the trends of the evaluated (Fig. (4-6) lines plus symbols) and calculated (Fig. (4-6) dashed-dotted lines) potential minimum values in function of the sample fd-concentrations for each probe size and at each tweezers laser power. The calculated trends display a linear decaying dependency in function of fd-concentration for each probe size. The values of potential minima obtained from the fitting to the data follow the calculated predictions very well at low fd-concentrations and for the lowest tweezers laser power. The trends which are experimentally observed with the 1 μm sphere show a linear decay along the full range of concentrations however, at a different level for each tweezers laser power. This is probably again due to the fact that this probe sphere has a size which lies more certainly in the Mie-Lorentz regime. For the 2 μm spheres the experimental data follow the expected trends qualitatively within some experimental scatter throughout the entire concentration range and the influence of the laser tweezers is less pronounced and not systematic. The experimental data from the 3 μm and especially the 4 μm spheres quantitatively agree with the predictions at low fd-concentrations, and no influence of the tweezers power is detected. However, at larger concentrations, deviations from the predictions beyond experimental scatter become evident. This is the case in particular for the 4 μm sphere at fd-concentration above 0.6 mg/mL.

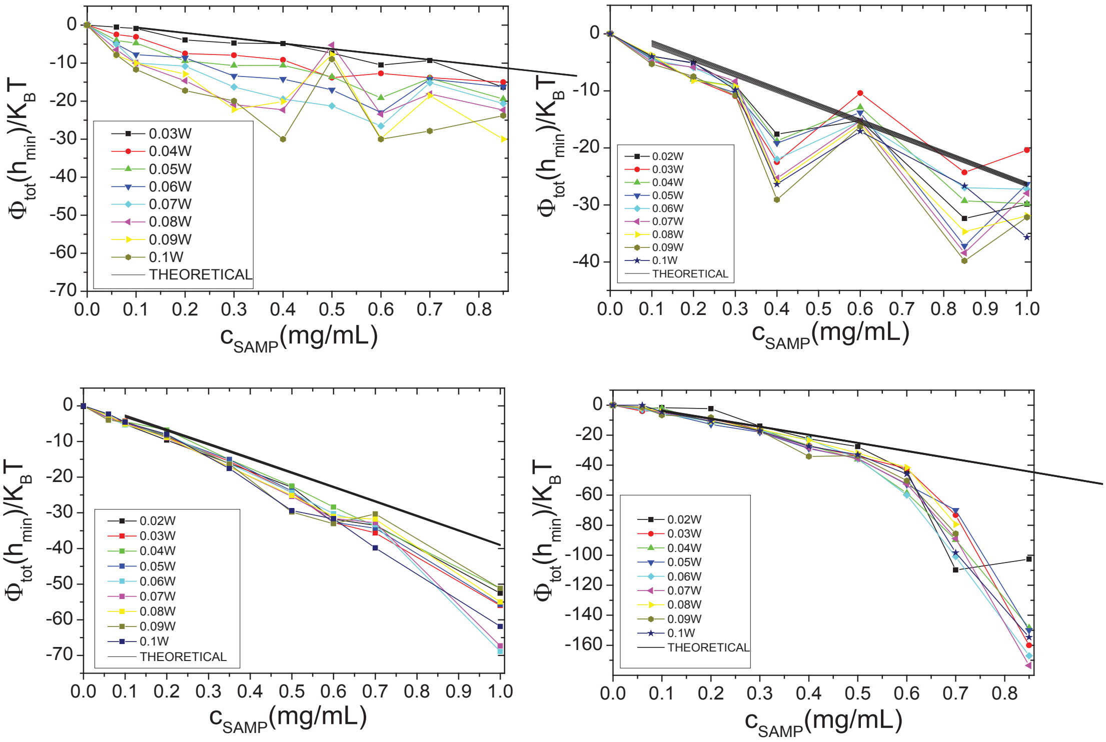

Figure 4-6 trends of the total interaction potential minima (lines plus symbols) achieved from the fitting operations to the experimental interaction potentials for all the probes: d=1 μm (a), d=2 μm (b), d=3 μm (c), d=4 μm (d), and at all laser powers used in function of increasing fd-concentration along with the calculated trends (collapsing lines).

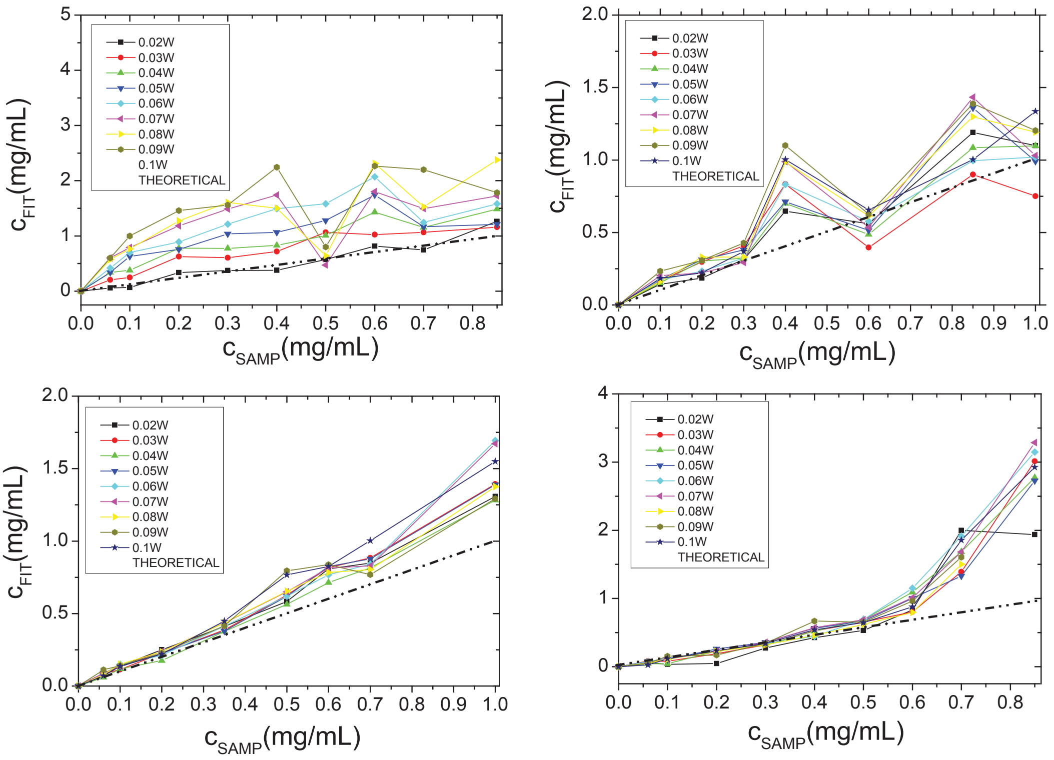

Figure 4-7 trends of the concentrations achieved from the fitting operations of all experimental interaction potentials for all probes, from the upper left corner going clock wise: 1-2-3 and 4 μm in diameter at all laser powers used (lines plus symbols) in function of increasing fd-concentration along with the calculated theoretical trends (dash-dotted lines).

In Figure (4-7), the depletant concentrations obtained as fitting parameters, c_{FIT}, are shown in dependence of the real c_{SAMP}, which was pre-set and determined independently by UV/VIS spectroscopy. Here the dashed-dotted line describes the linear trend with zero intercept and slope of one, which was expected if the model described the experiment correctly throughout the entire range of concentrations. At higher rod concentrations, the data obtained with the two smallest spheres appear to follow the linear trend up to the highest concentration within experimental scatter, apart from the tweezers induced anomaly in the case of the 1 μm sphere. Differently, in the case of the 4 μm sphere there is a significant deviation above c_{SAMP} = 0.5mg/mL. Also in the case of the 3 μm probe sphere, the experimental data deviate systematically from the predictions towards higher values, indicating a stronger depletion interaction than expected from the model which applies Derjaguin and low density approximation. These observations confirm earlier data by July, who found the same effect but did not explore it systematically [62].

The data in Figures (4-6) and (4-7) allow an assessment of the limits of the two basic approximations of the theoretical model. In cases where Derjaguin approximation is expected to hold, e.g. for the two largest spheres, the low density limit appears to break down only at rod concentrations as high as seven times the overlap value. At higher concentrations, the attractive potential is significantly (up to a factor of three in our set of data) deeper than predicted by the low density approximation. It is interesting to note that the only theoretical treatments, which take into account increased rod number densities [58], predict only a very small effect of the order of six percent and most importantly with the opposite sign from that of our experimental results, towards smaller values of interaction strength. At the moment there is no explanation for the behaviour we measured. Based on numerical calculations, it is expected that deviations of experimental depletion potentials from the Derjaguin description should be of the order of ten percent for the case of the 2 μm sphere [59], while the experimental data are expected to be smaller than the Derjaguin prediction by a factor of two in the case of the 1 μm sphere. Contrarily, here it is observed that in both cases there is no significant deviation of the experimental data from the approximate theoretical prediction. It is however possible that this finding occurs due to a fortuitous balancing of effects. While a violation of the low density approximation causes a deepening of the effective depletion potential, as observed with the large probe spheres, the violation of Derjaguin approximation is expected to have the opposite effect. A potential explanation for such observations could lie in the dynamics of the system, because there is a further implicit assumption hidden the theory of depletion by rods. The assumption that the system is always in thermal equilibrium implies that any fluctuations of the depletant density relax instantaneously. Therefore, the next step in the current experimental investigation has been to use the TIRM data to study the dynamics of the single-particle in suspension of stiff thin rods, wandering if something was happening there at high fd-concentrations.

4.2 Results from Dynamic Data Analysis

4.2.1 Dynamics averaged over separation distances

As discussed in section (1.4.1) Prieve and co-workers [34, 35] showed that the initial slope of the time auto correlation function, $R(\tau)'$ (see Eq. (1.61)), of the scattered intensities (ITACF) is related to the particle diffusion coefficient normal to the interface, averaged over the illumination profile:

$$\langle D_n^{TIRM} \rangle = -\Lambda^{-2} \lim_{\tau \to 0} \frac{R'(0)}{R(0)}$$

where Λ^{-1} is the evanescent wave's penetration depth and $R'(0)$ is the derivative of the correlation function with respect to time that tends to zero (see section (1.4.1)).

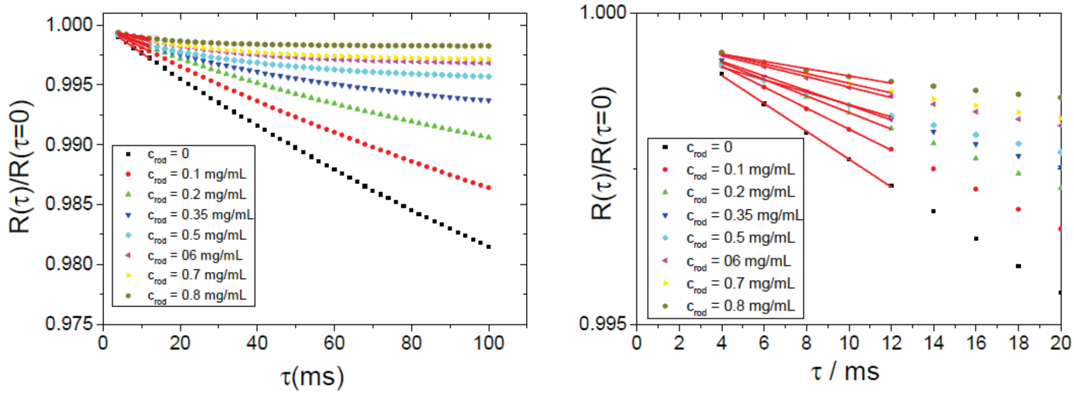

Figure 4-8 Left: Example of normalized time auto-correlation functions of scattered intensities calculated from intensity traces measured with a 3 μm probe sphere at a nominal tweezers laser power of 0.03W and at increasing fd-concentrations as indicated in the legend. Right: Zoom in to the short time regime. The red lines represent the linear fits at $\tau \to 0$ which were used to determine $< D_n^{TIRM} >$.

Figure (4-8) above, shows a representative set of examples of ITACFs, calculated with a time resolution of 2ms. The right box is a zoom in the short time regime where the averaged diffusion coefficients are determined multiplying the resulting slopes of the linear fits to the first five data points, with the squared penetration depth of the evanescent wave. This so defined averaged normal diffusion coefficient has also a theoretical formulation:

$$\langle D_n^{theo} \rangle = D_0 \frac{\int_0^{\infty} dh\, f(h+R) I(h)^2 p(h)}{\int_0^{\infty} dh\, I(h)^2 p(h)}$$

where D_0 is the Stokes-Einstein diffusion coefficient in the bulk, $p(h)$ is the Boltzmann-factor $p(h) \propto exp\{-\Phi(h)/k_BT\}$ corresponding to the interaction potential $\Phi(h)$, $I(h)$ is the scattered intensity which decays exponentially with particle-wall separation distance and $f(h+R)$ is the inverse of the Brenner near-wall friction coefficient for a sphere moving normal to the wall with its centre position located at $z = h + R$, as defined by Eq. (1.71). Thus the averaged theoretical normal diffusion coefficient has to be calculated by numerical integration, bearing in mind that the pair-wise interaction potential is a known quantity determined already case by case from the static treatment of the TIRM data and the solvent viscosity for the calculation of D_0 is fixed to $\eta = 1.5$ mPas. The latter is the viscosity of the depletant-free solution at $20^{\circ}C$, selected as reference viscosity due to the fact that, because of quasi-inevitable shear thinning [90] it is very difficult to reliably measure the viscosity of very dilute fd-suspensions.

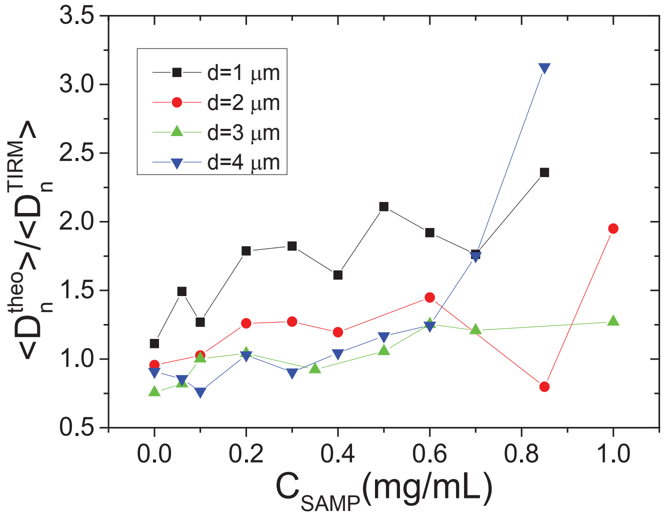

Figure 4-9 Ratio of theoretical and experimental averaged diffusion coefficients vs fd-concentration obtained at 0.03W nominal tweezers laser power for various particle sizes as indicated in the legend.

Figure (4-9) shows the $\frac{<D_n^{theo}>}{<D_n^{TIRM}>}$ ratios for each probe size and in function of fd-concentration. The experimental data were obtained at the lowest nominal tweezer laser power usable, namely 0.03 W. The data obtained from measurements on the 1 μm spheres (Fig. (4-9), black line and symbols) fall completely off the trend set by the other probe spheres due to the enhanced susceptibility of the smallest spheres to the tweezers power (see also Fig. (4-10)(a)). As for the rest of the trends (Fig. (4-9), coloured lines and symbols), up to an fd-content of about $C_{SAMP} = 0.60\ \frac{mg}{mL}$, experimental diffusion coefficients agree with the theoretical prediction within 20%

interval and with a slight increase of the ratio at increasing fd-concentration. Thus, considering the inverse proportionality linking viscosities to diffusion coefficients, the up-turn of the trends could be interpreted as the signature of increasing suspension viscosity with increasing depletant concentration.

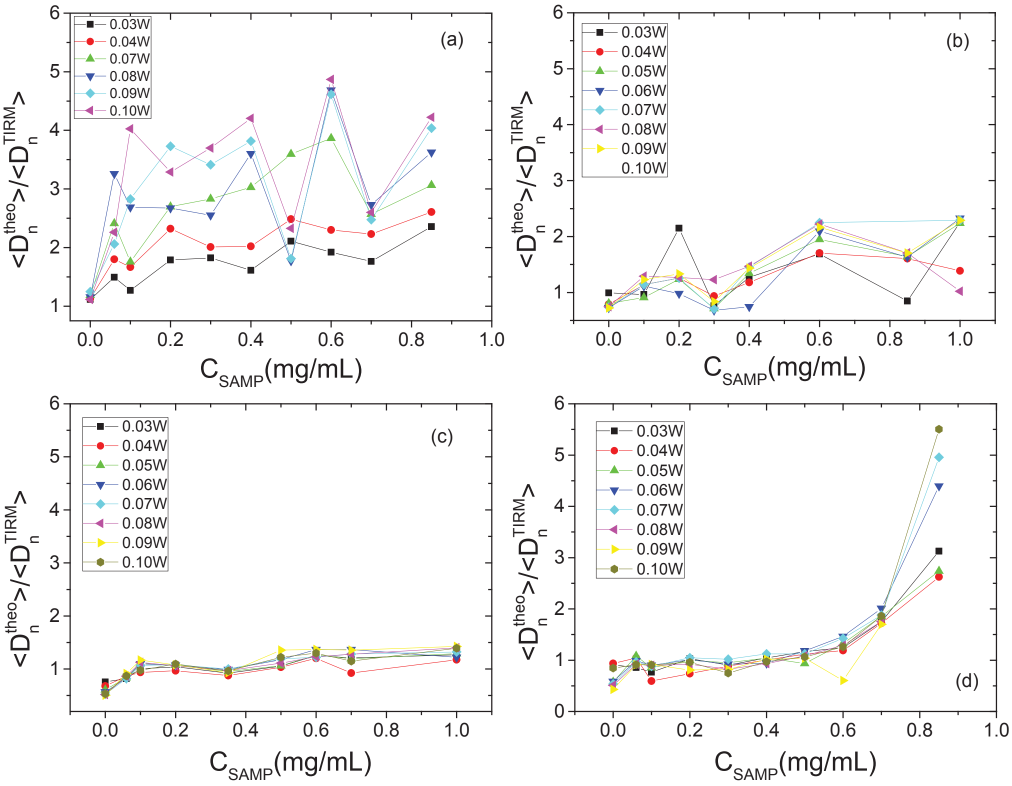

Figure 4-10 Ratio of theoretical and experimental averaged diffusion coefficients vs fd-concentration for different probe sizes: d=1 μm (a), d=2 μm (b), d=3 μm (c), d=4 μm (d) obtained at various nominal tweezers laser power as indicated in the legend.

Especially for the 4 μm in diameter probe spheres, above 0.60 mg/mL, the experimental diffusion coefficients become significantly smaller than the calculated values. This can be interpreted as the dynamic fingerprint of the observation from static data where, under these conditions, the apparent depletion potential is four times deeper than expected from the AO theoretical prediction. For completeness, the full set of data covering all probe sizes and tweezers laser powers is displayed in Figure (4-10) above.

The data confirm the basic features observed with a nominal tweezers power of 0.03W and the conclusions drawn from those. There are however, two drawbacks to this method of data analysing. First, as shown in the right panel of Fig. (4-8), the initial range in which the correlation functions can be approximated by a linear trend is very limited, especially at large fd-concentrations. Second, it is desirable to have spatially resolved dynamic information instead of a single measurement, representing an average over the illumination volume. Therefore we analysed the distributions of displacements height by height as will be discussed in the next section.

4.2.2 Dynamics at fixed separation distances

Calculation of distribution functions and their first moments

For the calculation of the displacements distribution functions, the intensity traces have to be converted to the one-dimensional particle trajectories in dependence of time, using the exponential relation between separation distance and scattered intensity. From these the discrete conditional probability distributions, $p_i(h_i,t|h_0)$ can be easily constructed by identifying all occurrences of a selected h_0-value and counting the frequencies $n_i(h_i(t))$ of a given value $h_i(t)$ after a given time t. These quantities can as well be expressed in terms of the particles centre of mass position z, bearing in mind that $z = h + R$,

$$p_i(z_i, t|z_o) = \frac{n_i(z_i(t))}{\sum_i^N n_i}$$

from which the mean displacement (MD) and the mean squared displacement (MSD) are calculated according to:

$$m(t|z_0) \equiv \langle z - z_o \rangle = \sum_{i=1}^{N} (z_i - z_0) p_i(z_i, t|z_o)$$

and:

$$W(t|z_0) \equiv \langle (z - z_o)^2 \rangle = \sum_{i=1}^{N} (z - z_0)^2 p_i(z_i, t|z_o)$$

Typical examples for separation distributions are shown in Figure (4-10) obtained from measurements on a 4 μm probe sphere in depletant-free suspensions with a nominal tweezers laser power of 0.03W. The distributions were calculated for the separation distances indicated in the labels of the plots y-axes and for various times as indicated in the legends. Independent of the starting separation distance h0, we observe that at very short times the distributions are symmetric and can be quantitatively fitted by a Gaussian, as it is shown in the lower right panel of Figure (4-10). At larger times the distributions turn askew, and their maximum shifts towards the equilibrium separation distance, h_{min}, of about 25 nm, distance at which the position of the maximum probability does not shift with time. At time $t \geq 500$ ms the shape of the distribution does not change any more with time, the system relaxed in its equilibrium state and its distribution function is quantitatively described by the Boltzmann factor of the static interaction potential. This is also demonstrated in the lower right panel of Figure (4-11), where the full magenta coloured trend represents the corresponding Boltzmann term which was calculated without any adjustable parameter and for a very long experimental time.

It takes to point out that there is a discrepancy in the evaluation of the equilibrium separation distance respect to the statics, in fact the equilibrium separation distance of a 4 μm bead in diameter, trapped at the nominal tweezers laser power of 0.03W in a depletant free suspension, in form the statics comes out to be $h_{min} = 45\ nm$. The discrepancy on the evaluation might depend partially on how much the static fit was able of reading the minimum of the interaction potential and partially on the fact that no fit was performed over the dynamic distributions either, given that the model followed by the askew distributions is unknown so no fitting operation is possible over those.

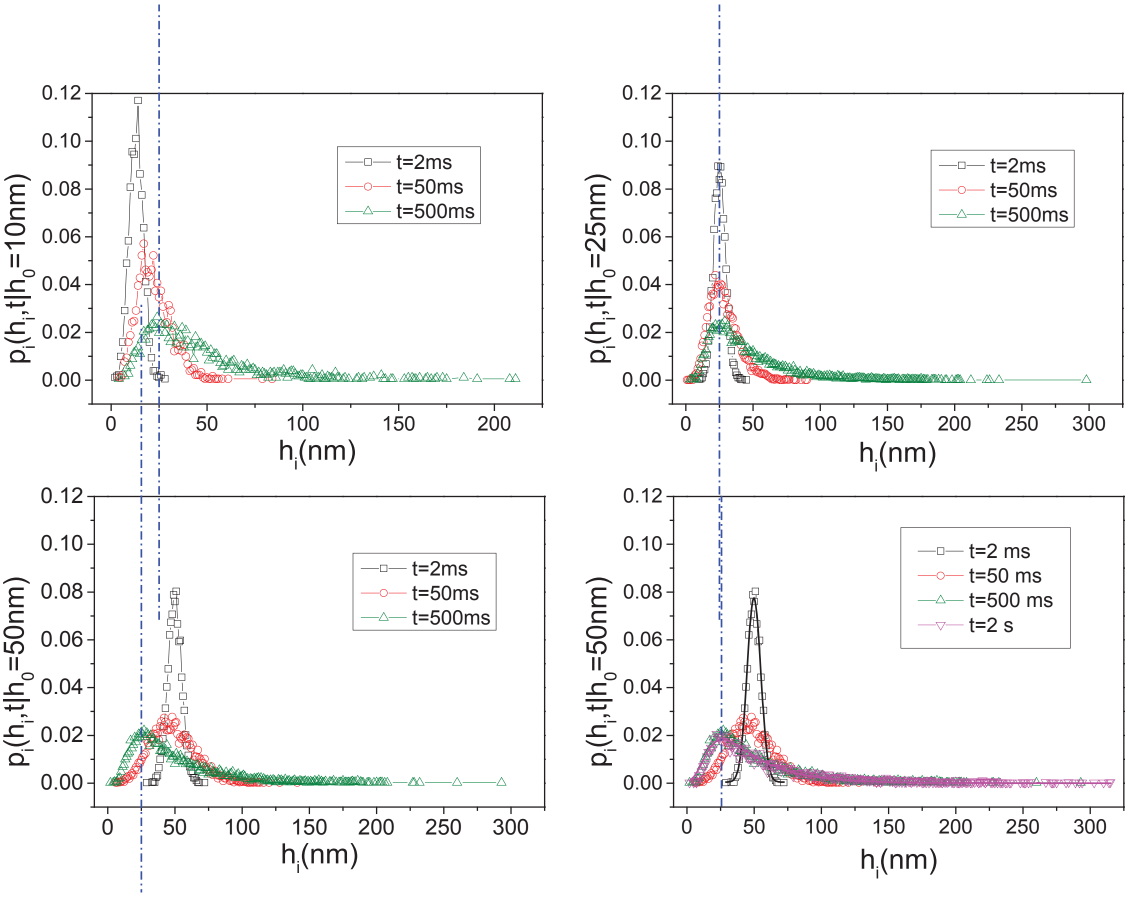

Figure 4-11 Distribution functions of separation distances obtained from a 4 μm particle in a depletant free suspension calculated for h_0=10 nm (top left), h_0=25 nm (top right), h_0=50 nm (bottom left and right) and the times indicated in the legends. Symbols are experimental data, vertical lines mark the equilibrium separation distance, the full black line in the lower right panel is a Gaussian fit and the magenta line represents the Boltzmann factor of the interaction potential obtained from the same raw data.

Some representative examples for the time dependence of MDs and MSDs are shown in Figure (4-12) below. At low starting values (h_0=10 nm, black curve in the left panel), the MDs are always positive and increase continuously with time, due to the repulsive interaction of the particle with the wall. Differently, at h_0=100 nm (purple curve in the left panel) where the effective gravitational contribution dominates the static potential, the mean displacements are always negative and decrease monotonically with time. In both cases the MD curves level off only at times beyond about two seconds. In cases where $h_o \approx h_m$, (light blue curve in the left panel) the absolute values of the mean displacements are very small, because the particle is almost force free at the starting position.

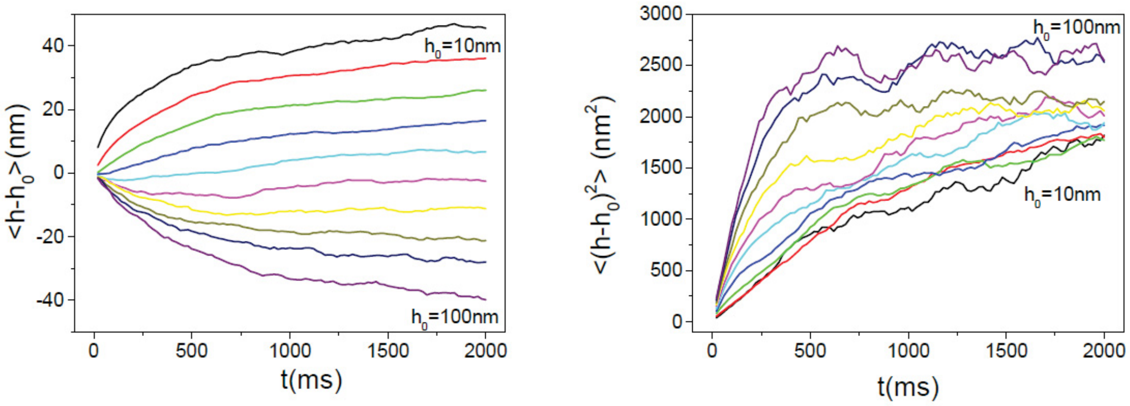

Figure 4-12 Mean displacements (left) and mean squared displacements (right) as a function of time of a 4 µm particle in a depletant free suspension. Curves were calculated for starting values ranging from 10 to 100 nm in steps of 10 nm.

All MSD curves show an almost linear time dependence at small times and level off to a plateau value at large times. The time at which the turnover to the constant value occurs, decreases with increasing h_0. According to Eqs. (1.77) and (1.78) respectively the initial slope of a MD vs time curve is the particles drift velocity at the chosen position, $v(z_0) = v(h_0 + R)$, while the slope of a MSD vs time curve is twice the position dependent diffusion coefficient $D_n(z_0)$. In the following sections these quantities will be treated in detail.

Mean squared displacements and diffusion coefficients

As discussed in section (1.4.2), diffusion coefficients normal to the interface are equal to half the initial slopes of the mean squared displacements vs time curves at a given position $h = z - R$. In Fig. (4-13) diffusion coefficients of particles in depletant free suspensions are displayed in terms of the ratio $\frac{D_n(h)}{D_0} = f_n^{-1}(h)$ versus the normalized separation distance h/R. For the convenience of notation, the subscript $_0$ is dropped here and further on. The error bars assigned to the experimental data represent the error resulting from the linear least squares fit to the initial part of the MSD vs. time curves. The experimental data are only qualitatively described with the expression of Eq. (1.72) by Honig and co-workers [72], if the solvent viscosity of 1.5 mPas (water with 15% ethanol) is used to calculate D_0 from the particle radius.

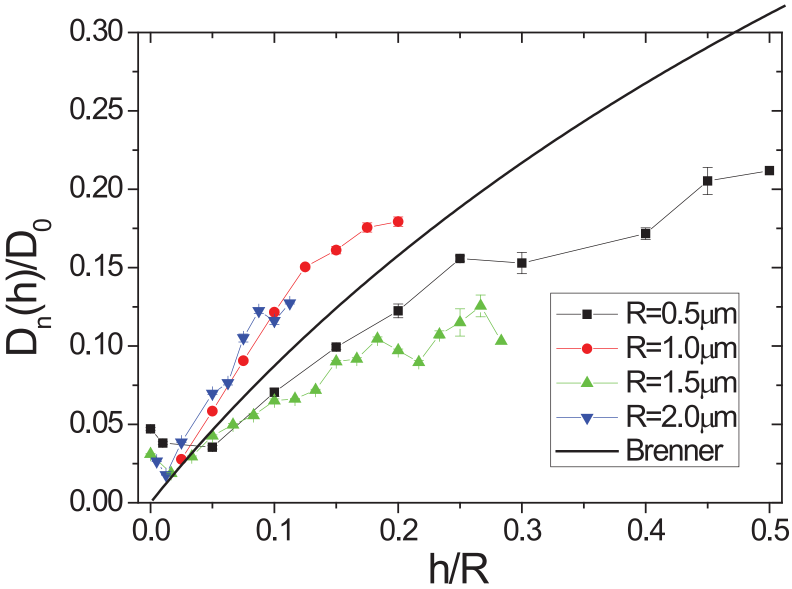

Figure 4-13 Normalized particle diffusion coefficients as a function of normalized separation distance. Symbols are experimental data for different probe particle sizes as indicated in the legend. Particles were suspended in depletant free solution. The full line is the theoretical prediction by Brenner and co-workers.

Figure (4-14) below, shows experimental data for differently sized colloidal spheres and varying fd-concentration, where again the ratio $\frac{D_n(h)}{D_0}$ is plotted versus the normalized separation distance h/R for all probe particle sizes and various depletant concentrations. For the two smallest probe particles all the experimental data follow the theoretical prediction, within the confidence limits set by the data acquired in depletant-free suspension. In the case of the two larger spheres, this holds only for low fd-concentrations up to approximately $c_{SAMP} \approx 0.4 - 0.5$ mg/mL. At larger depletant concentrations we observe a steep upturn of the diffusion coefficient versus separation distance curve, e.g. the data not even qualitatively follow the trend of the theoretical prediction. This observation might again be interpreted as a dynamic fingerprint of the finding from static data where for the large spheres and high fd-concentrations the apparent depletion potential is significantly deeper than expected from the classical theoretical prediction.

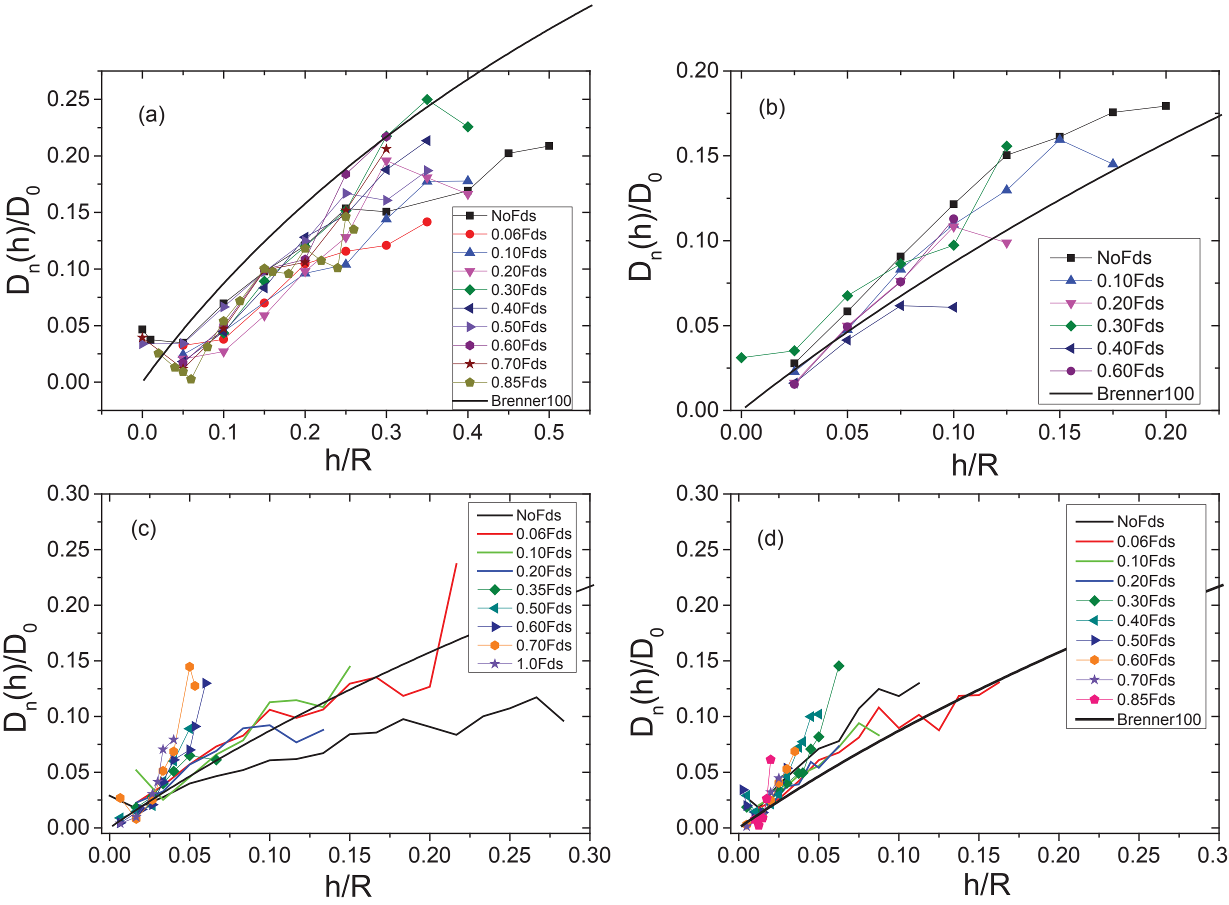

Figure 4-14 Normalized particle diffusion coefficients as a function of normalized separation distance. Symbols are experimental data for different fd-concentrations as indicated in the legend. The data for different probe particle sizes are collected in the four panels: (a) d=1 µm, (b) d=2 µm, (c) d=3 µm, and (d) d=4 µm. In all cases, the full black lines represent the theoretical prediction by Brenner and co-workers while in the last two quadrants the samples at low fd-concentration have been plotted as lines to better appreciate the difference with the trends at higher fd-concentration displayed as lines and symbols.

Mean displacements and drift velocities

As discussed in section (1.4.2), the initial slopes of the mean displacements vs time curves at a given position $h = z - R$ represent the particles' drift velocity at the chosen position. In Figure (4-15), drift velocities of particles in depletant-free suspensions are displayed as a function of separation distance. The symbols are experimental data for all probe sphere sizes, which were determined by linear least squares fitting of the initial part of the MD versus time curves, while the lines represent predictions using Eqs. (1.72) and (1.75). The input parameters for these calculations are the force acting on the particle and the solvent viscosity, which determines the particles' bulk diffusion coefficient. The latter was again set to $\eta = 1.5$ mPas in all cases and the forces were calculated using the parameters determined by the static potential measurements, thus there are no adjustable parameters.

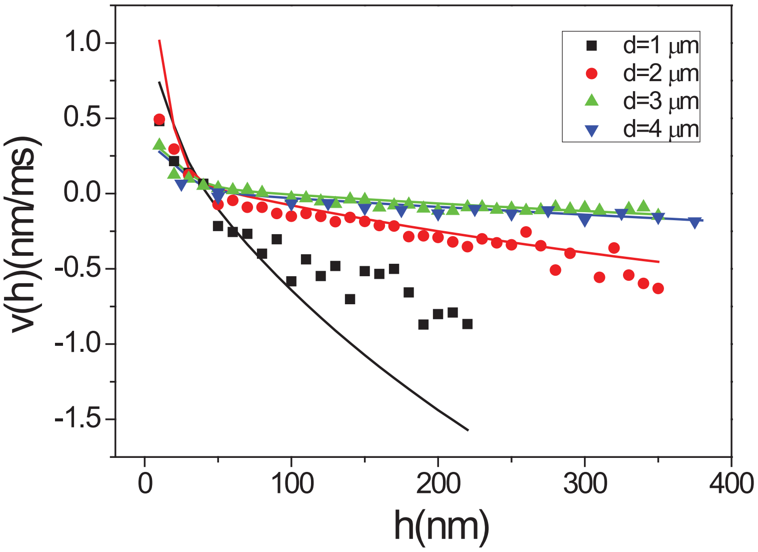

Figure 4-15 Particle drift velocities as a function of separation distance. Symbols are experimental data for different particle sizes as indicated in the legend obtained at 0.03 W tweezers laser power. Particles were suspended in depletant free solution. The full lines are parameter free model calculations using Eqs. (1.72) and Eq.(1.75).

Differently from the diffusion coefficients obtained from the same systems, shown before in Figure (4-13), here we observe a perfect agreement between experimental data and predictions for the drift velocities. The only exceptions are the data from the 1 μm diameter particles at large separation distance, where the force due to the tweezers laser is dominant, which makes the data unreliable, as discussed before.

The quantitative agreement between experimental and predicted drift velocities suggests a way of measuring local viscosities in the sample solution. For this purpose we determined the drift velocities from the MD versus time curves and now used Eqs. (1.72) and (1.75) as model function for a non-linear least squares fit with the viscosity as only parameter. The best fitting parameters are shown in Figure (4-16). Again the data obtained from the 1μm spheres are deviating significantly from the trends set by the other systems, which is again very likely due to the tweezers effect. The viscosities obtained for the other probe spheres fluctuate around the solvent viscosity of 1.5 mPas with some experimental scatter. Actually the average of all fitted viscosity values is 1.41 mPas. This finding may seem counterintuitive at first glance, since a significant increase of the viscosity with fd concentration should be expected. However, looking at the absolute velocity values, those have maximum values of about 0.5 nm/ms. On the other hand the times over which the MD vs time curves are evaluated, are 100 ms at maximum. Consequently we are observing drifts which are generally smaller than 50 nm. This is only ten or less percent of the radius of the hypothetical spherical volume a freely rotating fd-virus particle would occupy. Therefore it appears reasonable that the probe sphere does not feel any significant constraints on its mobility caused by the rods. Thus, it is rather only the friction with the solvent determining the local viscosity values evaluated with the fits.

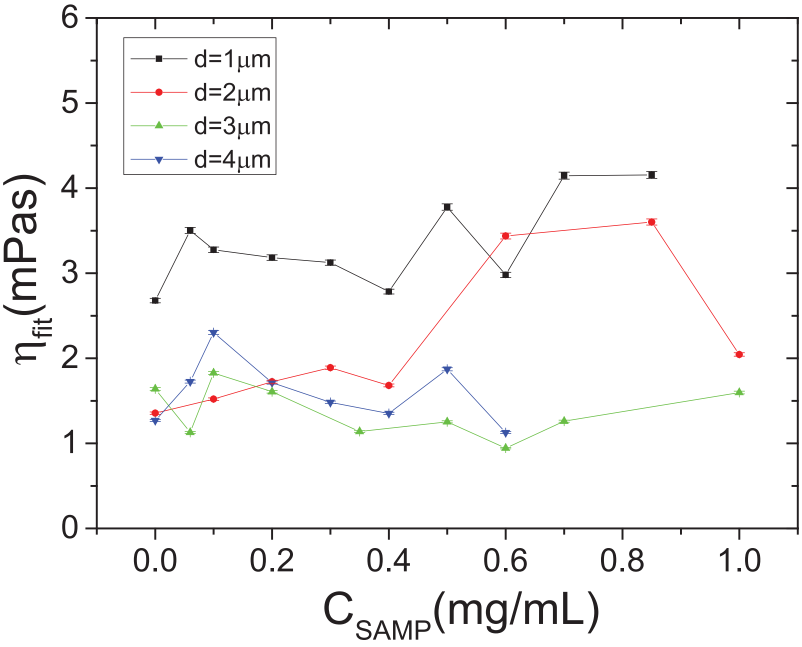

Figure 4-16 Local viscosities as a function of depletant concentration. Symbols are data for different particle sizes as indicated in the legend, obtained at 0.03 W tweezers laser power. The data were determined by non-linear least squares fitting of the drift velocities vs separation distance curves, using Eq. (1.75) as model function.

It is however intriguing, that the experimental data are much better described by the theoretical prediction in the case of the drift velocities than in the case of the diffusion coefficients. This finding will be discussed in the final section of this chapter.

Reliability of $D_n(z)$ and v(z) determination

According to Eqs. (1.77) and (1.78), we rely on an initial linear dependence of the particles' mean displacement and mean squared displacement on time for the determination of $v(z)$ and $D_n(z)$, respectively. Therefore, the ratio of the second coefficient in the short time expansions of these quantities over the first coefficient is a key parameter determining the reliability of the obtained results. For the simplification of notation we define:

$$m(t,z) \cong v(z)t + A(z)t^2 + \cdots$$

$$W(t,z) \cong 2D_n(z)t + B(z)t^2 + \cdots$$

where $A(z)$ and $B(z)$ are defined by Eq.(1.79) and Eq.(1.80), as the coefficients of the time squared terms respectively. With the latter quantities one can further define:

$$A_{drift}(z) \equiv \frac{A(z)}{v(z)}$$

$$B_{diff}(z) \equiv \frac{B(z)}{2D_n(z)}$$

which are coefficients that allow a direct visualization of the predominance of either the coefficient of the linear term or of the quadratic term, in function of z. Thus, the smaller A_{drift} and B_{diff}, the more reliable is the respective linear approximation for the time dependence of the MD and the MSD. It is important to note that the drift velocity will be very small or even zero close to the equilibrium separation distance $h_{\mathrm{m}}=z_{\mathrm{m}}-R$ and consequently , the ratio A_{drift} will diverge at z_{m}. Thus, the ratios A_{drift} and B_{diff} will only be discussed for separation distances $h \geq 0.1R$.

A collection of representative ratios is displayed in Figure (4-17), below. They were calculated for a sphere with radius R=2 μm, interacting with the wall by an electrostatic repulsion with amplitude B=20$k_{\mathrm{B}}T$ and a Debye screening length of 10 nm, an effective weigh force, $\tilde{F}_G = 75$ fN and a depletion potential of with amplitude depending on the fd-concentration, as indicated in the figures' legends. It is immediately evident that in all relevant cases the ratio $|A_{drift}| < 1$, while $|B_{diff}| \gg 1$ in most cases. Note that both parameter $A_{drift}(z)$ and $B_{diff}(z)$ have the dimension of a reciprocal time, which should be identified with the time range over which the linear fit is applied. This time is of the order of several milliseconds to several tens of milliseconds. However no matter which time range is chosen we will always observe that $A_{drift}(z) \ll B_{diff}(z)$ showing that the linear fit will always be less reliable in the case of the MSD data as compared to the MD data.

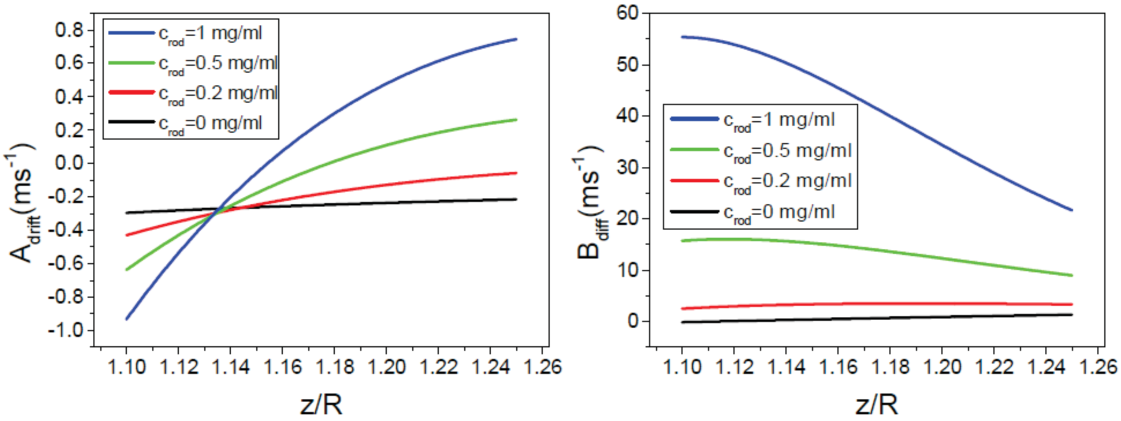

Figure 4-17 ratios between the second and first coefficient of the short time expansions of the time dependence of the mean displacement (left) and the mean squared displacement (right).Curves are calculated for a 4 µm sphere suspended in solutions with varying fd-concentrations as indicated in the legend.

This implies, that it is not appropriate to use a linear approximation for the time dependence of the MSD, no matter how short the selected time range is. A qualitative argument for this finding is that the second coefficient of the MSD time expansion, $B(z)$, contains the drift velocity, which is thus neglected by the linear approximation. However the drift velocity should never be neglected, since it will be effective at any time.

5 Conclusions

The present experimental investigation was about measurement, via TIRM, of static and dynamic properties of two different bio-mimetic systems:

- Colloids and interfaces coated with a 2D protein-layer called S-layer protein, to study protein-protein non-specific interaction;
- Binary mixtures of polystyrene probe spheres and fd-virus, to study depletion interactions beyond the limits of low density and Derjaguin approximation.

TIRM is a scattering technique normally used to measure interaction potentials between colloidal probes and the interface underneath, but the same intensity traces can be used also to infer dynamics. A novelty we proposed is the calculation of dynamic quantities at given heights (see section (1.4.2)), with further determination of absolute values of local viscosities (see section (4.2.2)). In the following, the conclusions drawn from the experiments, are organized in two sections: *Conclusions about Statics* (5.1) and *Conclusion about Dynamics* (5.2).

5.1 Conclusions about Statics

Preliminary TIRM measurements over protein-protein non-specific interactions between a colloidal spherical probe and the interface underneath, were obtained choosing fluorescent-fusion-S-layer proteins as coating agent (Esge-EGFP). Given that the only forces known so far justifying proteins stability at physiological conditions are Hydration forces [34], normally acting at very short distances [36], our measurements were performed at increasing ionic strengths, between $2 \div 60\,mM$ of HCl-Tris buffer, so to get the probe spheres closer and closer to the interface buy dumping repulsion, and at constant $pH = 9$, so far away from their iso-electric point.

Measurements have been performed with bare particles over bare wall (BB), to create a reference, and then with coated particles over bare wall (BC) and finally with coated particles over coated wall (CC), this time to understand weather the protein coating was causing any change in the otherwise expected DLVO potential between the probe and the interface. A comparison between the interaction potentials, from each aforementioned case, measured at equal salt concentration has shown that the interaction potential between ted surfaces (CC) has a much smoother Van der Waals attractive minimum at high salt concentrations, e.g. $c_{salt} = 40\,mM$, than the one of the bare particle over bare wall (BB) (see Fig. (4-2)(c)), and even higher salt concentrations are addressable in the latter case without sedimentation (see Fig. (4-2)(b)). At first glance one may argue that the stabilizing effect comes from hydration forces, but the measurements show an effect that extends from $50-100\ nm$, thus an order of magnitude higher than the usual range for hydration, which is about $2\ nm$. A plausible hypothesis to explain the change in shape for the coated surfaces interaction potentials is to consider that the coating could have determined a higher surface charge for both objects involved, resulting in a higher repulsive interaction. For this reason DLVO interaction potentials at increasing values of electrostatic amplitude, B, have being calculated to match the reduction of Van der Waals attractive minimum found from the data (see Fig. (4-3)). The latter calculations have shown that, for such effect to be due solely to the increased amount of surface charges, one would need an electrostatic amplitude at least thousand times higher than $20\ k_B T$. Unfortunately no proper fitting over the coated surfaces interaction potentials minima was possible, neither using hydration, nor a retarded Van der Waals attraction to correct the typical DLVO model. Nonetheless measurements have shown that a clear effect is present when the protein-coating is on and strong suggestions point towards some possibly new non-DLVO contribution as stabilization cause. Though, given the low experimental reproducibility we have encountered no strong conclusions could be made and further investigations over the matter are recommended.

The TIRM measurements performed to investigate depletion interactions beyond the limits of low density and Derjaguin's approximation, were carried out over a range of concentrations and probe sizes yet never reported in literature so systematically. From those it came out that the classical AO model holds up to concentrations almost $10 \times c^*$, so of about 0.6 mg/mL. Above such concentration the 4 micron beads in diameter display a much stronger depletion interaction that what expected by the AO model and a depletion force about 4 times higher. Similar trend seam to follow also the 3 micron in diameter beds, case in which though the divergence from the model is visible but less striking. All other probes, so the 2 and 1 micron beads in diameter, show no deviation from the model calculations through all the range of concentrations measured, most probably as a fortuitous cancellation of errors, given that for those two cases Derjaguin's approximation is also not fulfilled. Thus, respect to what already known in literature [59], the violation of the Derjaguin's approximation does not bring about as much of an error as numerically calculated; the violation of the low density approximation brings instead to an increase of the interaction strength of about 4 times; the 6% reduction predicted in fact by the high concentrations model by Mao, Cates and Lekkerkerker [58] strongly detaches from what shown by the experiment.

5.2 Conclusions about Dynamics

The analysis of the dynamic information of the TIRM data, reveals a fingerprint of the already observed deepening beyond expectations of the interaction potential minimum, for the largest spheres and at high fd-concentrations. What one can observe from the trends of the <Dnteo>, calculated from the auto-correlation functions of scattered intensity, in function of increasing fd-concentration, is an upturn of the trends at high fd-concentrations, implying higher values for the measured averaged normal diffusion coefficient respect to the theoretically calculated ones (see Fig. (4-9)), independently of the selected tweezers laser power (see Fig. (4-10)). One potential explanation for the experimental observation might be that the fd-suspensions at increasing concentrations are not anymore purely viscous, but an elastic contribution to their rheological properties will arise from the formation of an entangled network of rods [90]. Nonetheless one needs to keep in mind that auto-correlation functions do not allow the determination of absolute normal diffusion coefficients but only of averages respect to all possible particle positions. Thus, the latter cannot be used to explicitly evaluate solvent viscosities.

Thanks to this discomfort we though observed that there is potential to measure local mean displacements (MD) and mean square displacements (MSD) at given heights with TIRM. As explained in the theory section (1.4.2), once the intensity trace was converted into a trajectory over time, a fixed separation distance, namely z_0, was chosen to evaluate MD and MSD at that given height. The experimental value of the aforementioned dynamical quantities was obtained by simply applying the statistical definitions of mean and mean square displacement, while theoretically those were compared to Eqs. (1.77) and (1.78), respectively. From those it is clear that drift velocities and normal diffusion coefficients at given heights can be estimated as the initial slopes of the MD and MSD, respectively. Moreover, both drift velocity and normal diffusion coefficient, have an explicit dependence from D_0. To calculate local viscosities, we decided to compare the normal diffusion coefficients to the Brenner/Honig model (Eq. (1.72)) directly, and to fit all drift velocities in function of the height using Eq. (1.75) as fitting model.

The trends of the normal diffusion coefficients in function of the heights showed a clear divergence, especially for the largest probe spheres, at high fd-concentrations, detaching completely form the Brenner predictions (see Fig. (4-14)). Local viscosities could then be evaluated just for concentrations below 0.03 mg/mL finding an average value of $\eta_0 = 1.41$ mPas, quite close to the nominal viscosity of the depletant-free solution, $\eta_0 = 1.5$ mPas at 20°.

To check over the divergence shown by the trends of the diffusion coefficients at high concentrations, viscosities were evaluated also from the drift velocities at given heights, extracted for each height as the initial slope of the MD over time. In this case no divergence was found between theory and experimentally evaluated drift velocities and a viscosity of exactly 1.5 mPas was found on average from the fitting operations.

Finally, we identified the reason why drift velocities can be determined more reliably than diffusion coefficients from the initial slope of the time dependence of the MD and MSD respectively. In the latter case the ratio of the second coefficient in the short time expansion over the first coefficient is always much larger than unity (see Fig. (4-17) right side panel). This means that the linear approximation will always cause much greater errors in the determination of the diffusion coefficient then for the drift velocity. This is true especially for systems in an external force field, where drift velocities are non-zero at any time [91].

Acknowledgements

At this point I would like to thank all those who supported me in so many ways during these years. To start I am very grateful to Dr. Peter Lang for being so capable in remembering the Roman-Italian so well to make me feel at home (and not forgetting one of my favourite Italian dialects)! Moreover for supporting me with excellent supervision and giving me the opportunity of being part of the most welcoming and productive working environment. For the latter reasons I cannot forget to thank Professor Dhont, chief of the ICS-3 in Juelich, who has not spared the effort whenever asked for help or clarifications no matter how busy he was, so thank you deeply as well! Special thanks go to Marie Goeking, who has taken me by hand (literally!) through all the necessary paper work to make my PhD possible being a great example of efficiency, truly hard work and kindness, I will never forget! Thanks to Prof. Pavlik Lettinga for the generous fd-virus supplies, which have allowed me the study of depletion interactions, as well as for pushing towards a dynamical treatment of the acquired data sets which made another chapter of my PhD thesis. Thanks to Dr. Manolis Stiakakis for his generosity in supplying me with lab material from his own private ‘’colleciton’’ at any time I was in need (which were many indeed…). Thanks to Dr. Johan Buitenhuis for his kindness is sharing his tremendous knowledge of chemistry and his patience (especially!) in training me on the basic safety protocols in the lab, which probably kept me healthy and safe thus far. Thanks to Dr. Hartmuth Kriegs and Dipl.-Ing. Hans Juergen for their help and support with electronics and softwares I would have crushed otherwise! Thanks to Sylvia de Waal for taking such good care of the lab supplies and for helping me any time I needed to place orders…and for her artistic side in handmade jewellery which happened to be very convenient in more than one occasion! Thanks to Dr. Simone Wiegand, Dr. Gerhard Naegele, Dr. Kyongok Kang for all the helpful discussions. Special thanks to Dr. Gerhard Meier for the philosophical debates and wonderful teas aside, especially for being the wonderful person he is! Finally thanks to all my fellow-colleagues: Zilin Wang, Yunfei Jia, Yi Liu, Philip Neumann, Donald Guu, Olivera Korculanin, thank you all for your friendship and care, you have being like family to me, we had great times together and I love you all! Special thanks go to Dr. Christoph July, former PhD student at the ICS-3, who has built the TIRM set-up I worked with together with the acquisition software and trained me in the first months on both, I am very much obliged to his great capabilities as well as kindness.

Thanks to Cristina, and Andrea who shared with me the ‘burden’ of the Deutsche Bahn during winter times (!!!) and generally along the years spent commuting together. Thanks to Stella, Francesca, Gloria, Paola, Anna, Karan, Clara and so many more, from many other institutes in the Forschungszentrum Juelich for sharing the wonderful experience of the ‘’Bio-Soft’’ Helmholtz International Research School and special thanks to Dr. Auth Thorsten for the great endeavour of organizing it.

Thanks are due as well to Prof. Erik Reimhult, Dr. Peter Van Oostrum and Andrea Scheberl from the Institute of Biology-Inspired Materials of the BOKU University of Vienna for their generosity in providing me with the S-layer proteins used in the non-specific protein-protein interactions studies, free of charges.

Thanks to Antonio Giuliani from FORTH institute in Crete and Manos and Maria Amargianitakis from Heraklion for being of great help to me during the suffering of the writing process both psychologically and practically (thank you Manos for the lay out I would have never achieved without you!) and for being such great friends!

Finally, few rows are also due to my family and closest friends: I won’t be here and neither the person I am without you all, so thank you for being my strongest core!

I have the best memories of those years and this is mostly thanks to all the wonderful people I had the fortune of sharing those times with.

THANK YOU ALL!

Bibliography

1. Debye, P., *Light Scattering in Solutions.* Journal of Applied Physics, 1944. **15**(4): p. 338-342.
2. Zimm, B.H., *Molecular Theory of the Scattering of Light in Fluids.* The Journal of Chemical Physics, 1945. **13**(4): p. 141-145.
3. Dorfmüller, T., *B. J. Berne and R. Pecora: Dynamic Light Scattering, John Wiley and Sons Ltd., Baffins Lane 1976, 376 Seiten, Preis: £ 14,—.* Berichte der Bunsengesellschaft für physikalische Chemie, 1977. **81**(1): p. 101-101.
4. Israelachvili, J.N., R.K. Tandon, and L.R. White, *Measurement of forces between two mica surfaces in aqueous poly(ethylene oxide) solutions.* Nature, 1979. **277**(5692): p. 120-121.
5. Ducker, W.A., T.J. Senden, and R.M. Pashley, *Direct measurement of colloidal forces using an atomic force microscope.* Nature, 1991. **353**(6341): p. 239-241.
6. Furst, E.M., *Interactions, Structure, and Microscopic Response: Complex Fluid Rheology Using Laser Tweezers.* Soft Materials, 2003. **1**(2): p. 167-185.
7. Vossen, D.L.J., et al., *Optical tweezers and confocal microscopy for simultaneous three-dimensional manipulation and imaging in concentrated colloidal dispersions.* Review of Scientific Instruments, 2004. **75**(9): p. 2960-2970.
8. Grier, D.G., *Optical tweezers in colloid and interface science.* Current Opinion in Colloid & Interface Science, 1997. **2**(3): p. 264-270.
9. Biggs, S., D.C. Prieve, and R.R. Dagastine, *Direct comparison of atomic force microscopic and total internal reflection microscopic measurements in the presence of nonadsorbing polyelectrolytes.* Langmuir, 2005. **21**(12): p. 5421-5428.
10. Prieve, D.C., *Measurement of colloidal forces with TIRM.* Advances in Colloid and Interface Science, 1999. **82**(1–3): p. 93-125.
11. Walz, J.Y., *Measuring particle interactions with total internal reflection microscopy.* Current Opinion in Colloid & Interface Science, 1997. **2**(6): p. 600-606.
12. Bevan, M.A. and D.C. Prieve, *Direct Measurement of Retarded van der Waals Attraction.* Langmuir, 1999. **15**(23): p. 7925-7936.
13. Hertlein, C., et al., *Direct measurement of critical Casimir forces.* Nature, 2008. **451**(7175): p. 172-175.
14. Soyka, F., et al., *Critical Casimir Forces in Colloidal Suspensions on Chemically Patterned Surfaces.* Physical Review Letters, 2008. **101**(20): p. 208301.
15. Bechinger, C., et al., *Understanding Depletion Forces beyond Entropy.* Physical Review Letters, 1999. **83**(19): p. 3960-3963.
16. Kleshchanok, D., R. Tuinier, and P.R. Lang, *Direct measurements of polymer-induced forces.* Journal of Physics: Condensed Matter, 2008. **20**(7): p. 073101.
17. Xing, X., Z. Li, and T. Ngai, *pH-controllable depletion attraction induced by microgel particles.* Macromolecules, 2009. **42**(19): p. 7271-7274.
18. De Sio, S. and P. Lang, *Depletion Interaction Mediated by fd-Virus: on the Limit of Low Density and Derjaguin Approximation.* Zeitschrift für Physikalische Chemie, 2015. **229**(7-8).
19. Sullivan, C., *''Otto H.Schmitt, Como People of the past''.*

20. Vincent, J.F.V., et al., *Biomimetics: its practice and theory.* Journal of the Royal Society Interface, 2006. **3**(9): p. 471-482.
21. Marvin, D.A. and B. Hohn, *Filamentous bacterial viruses.* Bacteriological Reviews, 1969. **33**(2): p. 172-209.
22. Newman, J., H.L. Swinney, and L.A. Day, *Hydrodynamic properties and structure of fd virus.* Journal of molecular biology, 1977. **116**(3): p. 593-603.
23. Casadevall, A. and L.A. Day, *Thermal difference circular dichroism of Pf1 filamentous virus and effects of mercury (II), silver (I), and copper (II).* Biochemistry, 1988. **27**(10): p. 3599-3602.
24. Bhattacharjee, S., M.J. Glucksman, and L. Makowski, *Structural polymorphism correlated to surface charge in filamentous bacteriophages.* Biophysical Journal, 1992. **61**(3): p. 725-735.
25. Song, L., et al., *Dynamic light scattering from weakly bending rods: estimation of the dynamic bending rigidity of the M13 virus.* Biopolymers, 1991. **31**(5): p. 547-567.
26. Loh, E., E. Ralston, and V.N. Schumaker, *Quasielastic light scattering from solutions of filamentous viruses. I. Experimental.* Biopolymers, 1979. **18**(10): p. 2549-2567.
27. Beveridge, T.J., *Bacterial S-layers.* Current Opinion in Structural Biology, 1994. **4**(2): p. 204-212.
28. Kainz, B., et al., *Fluorescent S-layer protein colloids.* Soft Matter, 2010. **6**(16): p. 3809-3814.
29. Kainz, B., et al., *Absorption, Steady-State Fluorescence, Fluorescence Lifetime, and 2D Self-Assembly Properties of Engineered Fluorescent S-Layer Fusion Proteins of Geobacillus stearothermophilus NRS 2004/3a.* Biomacromolecules, 2010. **11**(1): p. 207-214.
30. Asakura, S. and F. Oosawa, *On interaction between two bodies immersed in a solution of macromolecules.* The Journal of Chemical Physics, 1954. **22**(7): p. 1255-1256.
31. Asakura, S. and F. Oosawa, *Interaction between particles suspended in solutions of macromolecules.* Journal of Polymer Science, 1958. **33**(126): p. 183-192.
32. Oosawa, F. and S. Asakura, *Surface Tension of High-Polymer Solutions.* The Journal of Chemical Physics, 1954. **22**(7): p. 1255-1255.
33. Ebbinghaus, S., et al., *An extended dynamical hydration shell around proteins.* Proceedings of the National Academy of Sciences, 2007. **104**(52): p. 20749-20752.
34. Israelachvili, J.N., *15 - Solvation, Structural, and Hydration Forces*, in *Intermolecular and Surface Forces (Third Edition)*. 2011, Academic Press: San Diego. p. 341-380.
35. Gapinski, J., et al., *Diffusion and microstructural properties of solutions of charged nanosized proteins: Experiment versus theory.* The Journal of Chemical Physics, 2005. **123**(5): p. 054708.
36. Valle-Delgado, J.J., et al., *Interactions between bovine serum albumin layers adsorbed on different substrates measured with an atomic force microscope.* Physical Chemistry Chemical Physics, 2004. **6**(7): p. 1482-1486.
37. Sleytr, U.B., *Regular Arrays of Macromolecules on Bacterial Cell Walls: Structure, Chemistry, Assembly, and Function*, in *International Review of Cytology*, G.H. Bourne and J.F. Danielli, Editors. 1978, Academic Press. p. 1-64.
38. Sleytr, U.B., et al., *Crystalline bacterial cell surface layers (S layers): from supramolecular cell structure to biomimetics and nanotechnology.* Angewandte Chemie International Edition, 1999. **38**(8): p. 1034-1054.
39. Sleytr, U.B., et al., *Crystalline bacterial cell surface layers.* Molecular microbiology, 1993. **10**(5): p. 911-916.

40. Huber, C., et al., *Heterotetramers Formed by an S-Layer–Streptavidin Fusion Protein and Core-Streptavidin as a Nanoarrayed Template for Biochip Development.* Small, 2006. **2**(1): p. 142-150.
41. Ilk, N., et al., *Molecular characterization of the S-layer gene, sbpA, of Bacillus sphaericus CCM 2177 and production of a functional S-layer fusion protein with the ability to recrystallize in a defined orientation while presenting the fused allergen.* Applied and environmental microbiology, 2002. **68**(7): p. 3251-3260.
42. Moll, D., et al., *S-layer-streptavidin fusion proteins as template for nanopatterned molecular arrays.* Proceedings of the National Academy of Sciences, 2002. **99**(23): p. 14646-14651.
43. Völlenkle, C., et al., *Construction of a functional S-layer fusion protein comprising an immunoglobulin G-binding domain for development of specific adsorbents for extracorporeal blood purification.* Applied and environmental microbiology, 2004. **70**(3): p. 1514-1521.
44. Tschiggerl, H., et al., *Exploitation of the S-layer self-assembly system for site directed immobilization of enzymes demonstrated for an extremophilic laminarinase from Pyrococcus furiosus.* Journal of biotechnology, 2008. **133**(3): p. 403-411.
45. Tschiggerl, H., et al., *Display of a peptide mimotope on a crystalline bacterial cell surface layer (S-layer) lattice for diagnosis of Epstein–Barr virus infection.* Bioconjugate chemistry, 2008. **19**(4): p. 860-865.
46. Schäffer, C., et al., *Novel Biocatalysts Based on S-Layer Self-Assembly of Geobacillus Stearothermophilus NRS 2004/3a: A Nanobiotechnological Approach.* Small, 2007. **3**(9): p. 1549-1559.
47. Badelt-Lichtblau, H., et al., *Genetic Engineering of the S-Layer Protein SbpA of Lysinibacillus sphaericus CCM 2177 for the Generation of Functionalized Nanoarrays†.* Bioconjugate chemistry, 2009. **20**(5): p. 895-903.
48. Delcea, M., et al., *Thermal stability, mechanical properties and water content of bacterial protein layers recrystallized on polyelectrolyte multilayers.* Soft Matter, 2008. **4**(7): p. 1414-1421.
49. Dogic, Z. and S. Fraden, *Development of model colloidal liquid crystals and the kinetics of the isotropic–smectic transition.* Philosophical Transactions of the Royal Society of London A: Mathematical, Physical and Engineering Sciences, 2001. **359**(1782): p. 997-1015.
50. Koenderink, G.H., et al., *Depletion-Induced Crystallization in Colloidal Rod−Sphere Mixtures.* Langmuir, 1999. **15**(14): p. 4693-4696.
51. Urakami, N. and M. Imai, *The Effect of Sphere Size on the Phase Behaviors in the Rod and Sphere Mixture System.* Journal of Macromolecular Science, Part B, 2003. **42**(3-4): p. 533-543.
52. Adams, M., et al., *Entropically driven microphase transitions in mixtures of colloidal rods and spheres.* Nature, 1998. **393**(6683): p. 349-352.
53. Helden, L., et al., *Direct Measurement of Entropic Forces Induced by Rigid Rods.* Physical Review Letters, 2003. **90**(4): p. 048301.
54. Rudhardt, D., C. Bechinger, and P. Leiderer, *Direct Measurement of Depletion Potentials in Mixtures of Colloids and Nonionic Polymers.* Physical Review Letters, 1998. **81**(6): p. 1330-1333.
55. Sharma, A. and J.Y. Walz, *Direct measurement of the depletion interaction in a charged colloidal dispersion.* Journal of the Chemical Society, Faraday Transactions, 1996. **92**(24): p. 4997-5004.

56. Yaman, K., C. Jeppesen, and C.M. Marques, *Depletion forces between two spheres in a rod solution.* EPL (Europhysics Letters), 1998. **42**(2): p. 221.
57. Auvray, L., *Solutions de macromolécules rigides : effets de paroi, de confinement et d'orientation par un écoulement.* Journal de physique, 1981. **42**(1): p. 79-95.
58. Mao, Y., M.E. Cates, and H.N.W. Lekkerkerker, *Theory of the depletion force due to rodlike polymers.* The Journal of Chemical Physics, 1997. **106**(9): p. 3721-3729.
59. Lang, P.R., *Depletion interaction mediated by polydisperse rods.* The Journal of Chemical Physics, 2007. **127**(12): p. -.
60. Lin, K.-h., et al., *Colloidal Interactions in Suspensions of Rods.* Physical Review Letters, 2001. **87**(8): p. 088301.
61. Lau, A., K.-H. Lin, and A. Yodh, *Entropic interactions in suspensions of semiflexible rods: Short-range effects of flexibility.* Physical Review E, 2002. **66**(2): p. 020401.
62. July, C. and P.R. Lang, *Depletion Interactions Effected by Different Variants of fd Virus.* Langmuir, 2010. **26**(24): p. 18647-18651.
63. Frej, N.A. and D.C. Prieve, *Hindered diffusion of a single sphere very near a wall in a nonuniform force field.* The Journal of Chemical Physics, 1993. **98**(9): p. 7552-7564.
64. Bevan, M.A. and D.C. Prieve, *Hindered diffusion of colloidal particles very near to a wall: Revisited.* The Journal of Chemical Physics, 2000. **113**(3): p. 1228-1236.
65. Ashkin, A., *Acceleration and Trapping of Particles by Radiation Pressure.* Physical Review Letters, 1970. **24**(4): p. 156-159.
66. Ashkin, A., *Forces of a single-beam gradient laser trap on a dielectric sphere in the ray optics regime.* Biophysical journal, 1992. **61**(2): p. 569.
67. Ashkin, A., et al., *Observation of a single-beam gradient force optical trap for dielectric particles.* Optics letters, 1986. **11**(5): p. 288-290.
68. Neto, P.M. and H. Nussenzveig, *Theory of optical tweezers.* EPL (Europhysics Letters), 2000. **50**(5): p. 702.
69. Mazolli, A., P.M. Neto, and H. Nussenzveig. *Theory of trapping forces in optical tweezers*. in *Proceedings of the Royal Society of London A: Mathematical, Physical and Engineering Sciences*. 2003. The Royal Society.
70. Malagnino, N., et al., *Measurements of trapping efficiency and stiffness in optical tweezers.* Optics Communications, 2002. **214**(1): p. 15-24.
71. Walz, J.Y. and D.C. Prieve, *Prediction and measurement of the optical trapping forces on a microscopic dielectric sphere.* Langmuir, 1992. **8**(12): p. 3073-3082.
72. Honig, E.P., G.J. Roebersen, and P.H. Wiersema, *Effect of hydrodynamic interaction on the coagulation rate of hydrophobic colloids.* Journal of Colloid and Interface Science, 1971. **36**(1): p. 97-109.
73. Brenner, H., *The slow motion of a sphere through a viscous fluid towards a plane surface.* Chemical Engineering Science, 1961. **16**(3): p. 242-251.
74. Goldman, A.J., R.G. Cox, and H. Brenner, *Slow viscous motion of a sphere parallel to a plane wall—I Motion through a quiescent fluid.* Chemical Engineering Science, 1967. **22**(4): p. 637-651.
75. Volpe, G., et al., *Novel perspectives for the application of total internal reflection microscopy.* Optics Express, 2009. **17**(26): p. 23975-23985.
76. Adams, M. and S. Fraden, *Phase Behavior of Mixtures of Rods (Tobacco Mosaic Virus) and Spheres (Polyethylene Oxide, Bovine Serum Albumin).* Biophysical Journal. **74**(1): p. 669-677.
77. Hertlein, C., et al., *Experimental Verification of an Exact Evanescent Light Scattering Model for TIRM.* Langmuir, 2008. **24**(1): p. 1-4.

78. Prendergast, F.G. and K.G. Mann, *Chemical and physical properties of aequorin and the green fluorescent protein isolated from Aequorea forskalea.* Biochemistry, 1978. **17**(17): p. 3448-3453.
79. Tsien, R.Y., *THE GREEN FLUORESCENT PROTEIN.* Annual Review of Biochemistry, 1998. **67**(1): p. 509-544.
80. Valle-Delgado, J.J., et al., *Measurement of interactions between protein layers adsorbed on silica by atomic force microscopy.* Journal of Physics: Condensed Matter, 2004. **16**(26): p. S2383.
81. Berg, J.M., J.L. Tymoczko, and L. Stryer, *Biochemistry, Fifth Edition*. 2002: W. H. Freeman.
82. Biology, A.S.f.C., *Molecular biology of the cell*. 2003: American Society for Cell Biology.
83. Harvey Lodish, A.B., S Lawrence Zipursky, Paul Matsudaira, David Baltimore, and James Darnell, *Book reviews.* Biochemistry and Molecular Biology Education, 2001. **29**(3): p. 126-133.
84. Kamerlin, S.C.L. and A. Warshel, *At the Dawn of the 21(st) Century: Is Dynamics the Missing Link for Understanding Enzyme Catalysis?* Proteins, 2010. **78**(6): p. 1339-1375.
85. Dumetz, A.C., et al., *Patterns of protein–protein interactions in salt solutions and implications for protein crystallization.* Protein Science : A Publication of the Protein Society, 2007. **16**(9): p. 1867-1877.
86. Li, W., et al., *Charge-Induced Patchy Attractions between Proteins.* The Journal of Physical Chemistry B, 2014. **119**(2): p. 503-508.
87. Fusco, D. and P. Charbonneau, *Crystallization of asymmetric patchy models for globular proteins in solution.* Physical Review E, 2013. **88**(1): p. 012721.
88. Wang, W., et al., *Serum Ferritin: Past, Present and Future.* Biochimica et biophysica acta, 2010. **1800**(8): p. 760-769.
89. Helden, L., et al., *Depletion potentials induced by charged colloidal rods.* Langmuir, 2004. **20**(14): p. 5662-5665.
90. Lang, C., et al., *The Connection between Biaxial Orientation and Shear Thinning for Quasi-Ideal Rods.* Polymers, 2016. **8**(8).

91. De Sio, S., J.K.G. Dhont and P.R. Lang, *Near Wal Dynamics of a spherical particle in crowded suspensions of colloidal rods-dynamic information from TIRM revisited*,Soft Matter, in revision.